

Dust continuum, CO and [C_I] 1-0 lines: Self-consistent H₂ mass estimates and the possibility of globally CO-‘dark’ galaxies at $z=0.35$

L. Dunne,^{1,2*} S. J. Maddox,¹ C. Vlahakis,³ H. L. Gomez¹

¹*School of Physics & Astronomy, Cardiff University, Queens Buildings, The Parade, Cardiff, CF24 3AA, UK*

²*SUPA, Institute for Astronomy, University of Edinburgh, Royal Observatory, Blackford Hill, Edinburgh EH9 3HJ, UK*

³*National Radio Astronomy Observatory, 520 Edgemont Road, Charlottesville, VA 22903-2475, USA*

18 November 2021

ABSTRACT

We present ALMA observations of a small but statistically complete sample of twelve 250 μ m selected galaxies at $z = 0.35$ designed to measure their dust submillimeter continuum emission as well as their ¹²CO(1 – 0) and atomic carbon [C_I](³P₁–³P₀) spectral lines. This is the first sample of galaxies with global measures of all three H₂-mass tracers and which show star formation rates (4–26 M_⊙ yr^{–1}) and infra-red luminosities (1 – 6 × 10¹¹ L_⊙) typical of star forming galaxies in their era. We find a surprising diversity of morphology and kinematic structure; one-third of the sample have evidence for interaction with nearby smaller galaxies, several sources have disjoint dust and gas morphology. Moreover two galaxies have very high $L'_{\text{C I}}/L'_{\text{CO}}$ ratios for their *global* molecular gas reservoirs; if confirmed, such extreme intensity ratios in a sample of dust selected, massive star forming galaxies presents a challenge to our understanding of ISM. Finally, we use the emission of the three molecular gas tracers, to determine the carbon abundance, X_{C I}, and CO–H₂ conversion α_{CO} in our sample, using a weak prior that the gas-to-dust ratio is similar to that of the Milky Way for these massive and metal rich galaxies. Using a likelihood method which simultaneously uses all three gas tracer measurements, we find mean values and errors on the mean of $\langle \alpha_{\text{CO}} \rangle = 3.0 \pm 0.5 \text{ M}_{\odot} (\text{K kms}^{-1} \text{ pc}^2)^{-1}$ and $\langle X_{\text{C I}} \rangle = 1.6 \pm 0.1 \times 10^{-5}$ (or $\alpha_{\text{C I}} = 18.8 \text{ M}_{\odot} (\text{K kms}^{-1} \text{ pc}^2)^{-1}$) and $\delta_{\text{GDR}} = 128 \pm 16$ (or $\alpha_{850} = 5.9 \times 10^{12} \text{ W Hz}^{-1} \text{ M}_{\odot}^{-1}$), where our starting assumption is that these metal rich galaxies have an average gas-to-dust ratio similar to that of the Milky Way centered on $\delta_{\text{GDR}} = 135$.

Key words: Galaxies: Local, Infrared, Star-forming, ISM

1 INTRODUCTION

The cold neutral gas (i.e. Cold Neutral Medium (CNM) H_I and H₂ gas) in galaxies is the main fuel for star formation and thus a driver of galaxy evolution across cosmic time, with the CNM being the phase where the H_I → H₂ phase transition takes place (e.g. Papadopoulos et al. 2002 and references therein).

Measuring the cold neutral gas content for large representative galaxy samples is thus a key requirement for understanding how galaxies form from gas clouds in dark matter haloes to the agglomerations of stars we see in the local Universe. There are, however, considerable difficulties involved in observing the cold gas phase. Neutral hydrogen (H_I) produces 21-cm line radiation, but its very low L_{H I}/M_{H I} ratio means that large arrays of radio telescopes such as the JVLA operating at the long cm range are required to observe it at

any redshift beyond the very local Universe ($z > 0.1$). This state of affairs will change dramatically once the so-called Square Kilometer Array (SKA) comes into operation.

Cold H₂ gas, with densities starting from $\sim (200 - 500) \text{ cm}^{-3}$ is the more intimate fuel for star formation in galaxies but unlike the case for H_I, the lowest transition available for H₂ mass tracing is S(0): J_u – J_l = 2 – 0, with $E_{20}/k_{\text{B}} \sim 510 \text{ K}$ which will not be excited appreciably for the typical temperature range of most of the molecular gas in Giant Molecular Clouds ($\sim (15 - 60) \text{ K}$). Indeed S(0) is mostly excited in shocks, containing only a few percent of the total H₂ gas mass.¹

This is the reason why the emission of tracer elements mixed with the H₂ gas are always used to determine its mass.

¹ Even if the S(0) line could somehow be excited for the bulk of the mass of a typical GMC, its rest-frame wavelength of $\sim 28 \mu\text{m}$ precludes routine observations from the ground over most of the cosmic volume as the atmosphere is opaque at such wavelengths.

* E-mail: DunneL6@cardiff.ac.uk

These are low-J rotational lines of CO (the next most abundant molecule in the Universe after H₂ itself), its most abundant isotopologue ¹³CO (though often very faint), and dust continuum emission (which, for star-forming ISM, is mostly mixed with H₂ rather than H_I). Thus, unlike the case of H_I, where an H_I line is used to trace its mass, for molecular gas, the relative abundance (R) of the species used to trace H₂ will always insert a first, common, uncertainty in the computed M(H₂) mass. This uncertainty enters non-linearly in the case of the typically optically thick low-J CO lines J=1–0, 2–1, where a (FUV/CR)-regulated $R_{\text{co}} = [\text{CO}/\text{H}_2]$ abundance enters the mass estimates via the non-linear dependence of the CO-H₂ (cloud volume)-filling factor on R_{co} . The uncertainty is linear only in the cases of optically thin tracers such as low-J ¹³CO lines ($R_{13\text{CO}} = [^{13}\text{CO}/\text{H}_2]$) or dust continuum emission ($R_{\text{dust}} = \text{M}(\text{dust})/\text{M}(\text{H}_2)$).

The low-J CO lines (J=1–0, 2–1), with their low critical densities ($n_{10,21} \sim (410, 2.7 \times 10^3) \text{ cm}^{-3}$, Jansen 1995), and small $E_{10}/k_B \sim 5.5 \text{ K}$, $E_{21}/k_B \sim 11 \text{ K}$, are very easily excited even in the coldest and most diffuse regions of molecular clouds, and thus remain luminous throughout their volumes. Their typically high optical depths ($\tau_{10} \sim 5 - 10$), and the resulting radiative trapping, make them even easier to excite by lowering the corresponding critical densities to: $n_{\text{crit}}^{(\text{eff})} \sim [(1 - e^{-\tau})/\tau] n_{\text{crit}}$, but are also responsible for a much less straightforward link between those luminosities and the underlying H₂ gas mass, than would have been the case should these CO lines be optically thin. This is what gives rise to the vagaries of the so called $\alpha_{\text{CO}} = \text{M}(\text{H}_2)/L_{\text{CO}}$ factor for the CO(1–0) line, (see Bolatto et al. 2013 for a good review).

There are quite a few effects in the use of CO lines as H₂ tracers which become more severe at high redshifts, namely:

(i) The conversion between ¹²CO(1–0) luminosity (L'_{CO}) and molecular gas mass is sensitive to metallicity in a non-linear fashion that is hard to calibrate, especially at the low ($Z \lesssim 0.2$) metallicities expected in the outer regions of local spirals, and even more so at high redshifts where present-epoch metallicity gradients are being built by cosmic chemical evolution.

(ii) ¹²CO(1–0) cannot be observed at high redshifts ($z \gtrsim 0.4$) without having to resort to the JVLA (the only array with adequate sensitivity). Any accessible higher-J CO lines (from J=3–2 and higher) trace only the warmer and denser H₂ gas, which may not necessarily be the bulk of H₂ gas mass even in vigorously star-forming galaxies.

(iii) The underlying assumption of CO line luminosities emanating from macro-turbulent clouds (where gas cells are radiatively decoupled in CO line emission) which are self-gravitating may not hold in some extreme environments where gas motions may be unbound or responding to significant concomitant stellar mass inside the clouds (Solomon et al. 1997; Downes & Solomon 1998).

(iv) At very high redshifts ($z \gtrsim 4$), the CO J=1–0, 2–1 lines lose their contrast against a brightening CMB, significantly reducing the visibility of ¹²CO(1–0) in the high- z Universe (da Cunha et al. 2013), but even more importantly the velocity fields and scale-lengths outlined by these lines are rendered nearly invisible inducing biases in the assessment of e.g. the dynamical mass enclosed (Zhang et al. 2016).

The latter is rather disconcerting given that, despite early claims of dusty distant starbursts containing mostly warm and dense gas (which could be traced using only high-J CO lines Tacconi et al. 2006, 2008), subsequent JVLA CO(1–0) line imaging of such galaxies found this not to be true and, in fact, their H₂ gas was found to be in a cold/diffuse state where only CO(1–0), (and 2–1) lines would be excited (Ivison et al. 2011). At $z \gtrsim 4$ large regions of such low-J CO line emission can be rendered nearly invisible by the CMB effect described by (Zhang et al. 2016).

Furthermore, multi-line studies of large (U)LIRG samples challenged the long-held view of $\alpha_{\text{CO}} \sim 1/5$ the Galactic value in these merger systems (Papadopoulos et al. 2012b). It is worth recalling that this long-held view was based on the study of four local (U)LIRGs (Downes & Solomon 1998), and on the premise that the total mass of dynamically unsettled merger systems can be computed via the virial theorem. Unfortunately the remedy is rather expensive in telescope time, demanding the observations of both low-J CO lines as well as observations of rotational lines of heavy rotor molecules such as HCN which are much fainter.

The emergent complications of using an α_{CO} factor in the distant Universe (or a simple bimodal application of it for disks and mergers) has been recently confounded by the discovery that Cosmic Rays (CRs) can be effective destroyers of the CO molecule, while leaving H₂ intact, especially in starbursts (Bisbas et al. 2017).

The combined effects of CRs, metallicity and UV fields have led to several theoretical and observational studies highlighting the possibility, and detection of, CO-‘dark’ molecular gas (Papadopoulos et al. 2002; Planck Collaboration et al. 2011; Pelupessy & Papadopoulos 2009; Wolfire et al. 2010; Pineda et al. 2013; Bisbas et al. 2015; Remy et al. 2017; Liszt et al. 2018). This gives more prominence to alternative H₂ gas mass tracers such as dust continuum and the two [C_I] lines.

Since the first statistical sub-mm survey of 100 local Far-Infrared (FIR) bright galaxies (SLUGS: Dunne et al. 2000; Dunne & Eales 2001), it has been clear that sub-mm derived dust masses ($\propto L_{850\mu\text{m}}$) and CO based molecular gas masses ($\propto L_{\text{CO}}$) are tightly correlated. The recent availability of large sub-mm selected samples from *Herschel* have seen an increase in the exploitation of dust as a measure of molecular gas content (Magdis et al. 2012; Rowlands et al. 2014; Scoville et al. 2014, 2016) and several large studies have demonstrated the potential for dust emission to be a good alternative tracer of molecular gas through comparisons of 850 μm emission and CO measurements (Scoville et al. 2014, 2016; Hughes et al. 2017; Orellana et al. 2017). So far, however, there is no independent verification that dust or CO are tracing the total molecular component effectively.

The third tracer of molecular hydrogen is the atomic carbon line [C_I](³P₁–³P₀) (hereafter [C_I](1–0)), with the [C_I](1–0) line being optically thin in most extragalactic situations. Its promise as an alternative extragalactic H₂ mass tracer was first comprehensively described by Papadopoulos et al. (2004); Papadopoulos & Greve (2004) (though see the early pioneering work by Keene et al. 1985, 1997). Early models of the chemical evolution of dense molecular clouds predicted that atomic carbon would be found only in a thin layer between the molecular CO form of C and the ionised C_{II} (Langer 1976; Tielens & Hollenbach 1985: the

standard PDR view). Subsequent observations of [C I] and CO in Galactic clouds were at odds with this model, measuring much higher $[C^0/CO]$ abundances than the standard PDR view predicted and also revealing that the [C I] emission was distributed widely throughout the cloud (Keene et al. 1985). A review of the models explored at that time to explain these high Carbon abundances was presented by Keene et al. (1985). One avenue of thought was that balance between the competing dynamical processes of accretion and evaporation of carbon atoms onto dust grain mantles would determine the Carbon abundance (Boland & de Jong 1982; Williams & Hartquist 1984) although there was disagreement about the main processes driving the evaporation (turbulence carrying cells to the cloud surface, or sputtering by shocks within the cloud). Another suggestion (Prasad & Tarafdar 1983) was that UV-photons could be produced deep within clouds by the interaction of cosmic rays with hydrogen molecules. This photon flux would dissociate CO and produce [C I] throughout the cloud. The idea of a cosmic ray regulated chemistry has been explored further in recent numerical work by Bisbas et al. (2017); Clark et al. (2019) and could explain the existence of some clouds in the Galactic Center Region which have unusually high $[C^0/CO]$ abundances (Tanaka et al. 2011) as well as the central regions of starburst galaxies and active nuclei (Israel & Baas 2002; Israel 2020; Izumi et al. 2020). Clouds in the process of forming are also expected to have higher Carbon abundances because of the timescale taken to reach equilibrium in the conversion of $C \rightarrow CO$ (Suzuki et al. 1992).

Atomic carbon has a simple partition function of 3 levels (unlike CO's rotational ladder), while the abundance ($X_{CI} = [C^0/H_2]$) uncertainty is one common to all H_2 tracer species (indeed X_{CI} may actually be the easiest of the three to model in terms of the prevailing ISM conditions, if it is indeed mostly CR-controlled (Bisbas et al. 2015)). Moreover, while much fainter than C II, the [C I] (1–0) line traces *only* molecular hydrogen, unlike C II which also traces the H I or H II gas components (which can be substantial for ‘young’ and forming high- z systems) (Papadopoulos et al. 2004; Liszt 2011; Pérez-Beaupuits et al. 2015; Clark et al. 2019).

The two [C I] transitions are, however, highly absorbed by the atmosphere, making large scale observational work in the local Universe challenging, even from the driest sites on Earth like the Atacama plateau where ALMA is located. As a result there has been little observational work surveying this line in extra-galactic sources, and most have been restricted to a few nearby starbursts, local (U)LIRGs and high- z SMG and QSO (Israel et al. 2006; Weiß et al. 2005; Walter et al. 2011; Zhang et al. 2014; Krips et al. 2016). *Herschel* expanded the observations of the [C I] lines in nearby galaxies with the FTS spectrometer (Kamenetzky et al. 2014; Lu et al. 2017; Jiao et al. 2017, 2019; Wilson et al. 2017; Crocker et al. 2019) but its limited sensitivity meant that the targets were mostly still (U)LIRGs or only the central regions of very nearby galaxies. The recent development of the Atacama Large Millimetre Array (ALMA) and upgrades to NOEMA have allowed an expansion of studies focused on using [C I] as a tracer of molecular gas at high redshifts (Alaghband-Zadeh et al. 2013; Bothwell et al. 2017; Valentino et al. 2018, 2020; Bourne et al. 2019), but what is lacking is a well defined sample of non-extreme star forming galaxies with global observations of all three main gas

tracers: $^{12}CO(1-0)$, [C I] (1–0) and sub-mm observations of cold dust.

This paper describes the observations, data reduction and results for a first dedicated study of the dust, $^{12}CO(1-0)$ and [C I] (1–0) emission in a small but homogeneously selected sample of galaxies in the relatively local Universe at $z = 0.35$. This is possible thanks to the *Herschel*-ATLAS (Eales et al. 2010): the first unbiased survey of the dust content of local galaxies, covering 660 sq. deg and sensitive to the cold dust component which dominates the mass of dust in galaxies. The large areal coverage lends itself to producing samples of (cold ISM)-selected sources at a variety of redshifts with which to revisit the relationships of dust, CO and [C I] emission with the aim to cross-calibrate each tracer of molecular gas mass in massive metal-rich galaxies. A companion paper (Dunne et al. *in prep*) will combine this sample with numerous others from the literature to provide the first joint analysis of the calibration of H_2 gas mass tracers using all three methods in a self-consistent way.

In Section 2 we describe the sample, observations and data reduction. In Section 3 we discuss the results and comparisons of the three gas tracers. In Section 4 we present our method for deriving the gas calibration factors for this sample. We also find the very surprising result that there is an overdensity of a factor 4–6 in the number of high redshift dusty galaxies found in these fields compared to blank field surveys. This is discussed in a companion paper, (Dunne et al. 2020). Throughout we use a cosmology with $\Omega_m = 0.308$ and $H_o = 67.9 \text{ km s}^{-1} \text{ Mpc}^{-1}$ (Planck Collaboration et al. 2016).

2 SAMPLE AND DATA

The sample was selected at $250\mu\text{m}$ from the *Herschel*-ATLAS Science Demonstration Phase (SDP) equatorial field at R.A. 09h. H-ATLAS was the widest area extragalactic survey carried out with the *Herschel* Space Observatory (Pilbratt et al. 2010), imaging 600 deg² in five bands centered on 100, 160, 250, 350 and $500\mu\text{m}$, using the PACS (Poglitsch et al. 2010) and SPIRE instruments (Griffin et al. 2010). One of the primary aims of the *Herschel*-ATLAS was to obtain the first unbiased survey of the local Universe at sub-mm wavelengths, and as a result was designed to overlap with existing large optical and infrared surveys. The *Herschel* observations consist of two scans in parallel mode reaching a 4σ point source sensitivity of 28 mJy beam^{-1} at $250\mu\text{m}$. The angular resolution is approximately $9''$, $13''$, $18''$, $25''$ and $35''$. While the original sample for the proposal was selected from the SDP public release catalogue described in Rigby et al. (2011) to have $S_{250} > 5\sigma$ and a reliable optical identification with spectroscopic redshift from Smith et al. (2011), we update the *Herschel* photometry and optical parameters in this paper to those from the H-ATLAS DR1 release (Valiante et al. 2016; Bourne et al. 2016). We use the SPIRE MADX (Maddox & Dunne 2020) matched filter photometry from the DR1 release, as these are all point sources and this is the most likely estimate of their flux. In the case of PACS, the LAMBDA algorithm of Wright et al. (2016) produces, in our opinion, a more robust measure of the PACS fluxes and errors as instead of using a top hat aperture, it convolves the optical r-band aperture

Table 1. Properties of galaxies in our sample.

H-ATLAS IAU	SDP name	GAMA ID	R.A (hh:mm:ss)	Dec. (dd:mm:ss)	z	S ₂₅₀ (mJy)	r _{pet}	Spectral type	Kinematic class	SMG
J090506.2 + 020700	163	347099	09:05:06.1	02:07:02.2	0.34507	107.6	18.8	Sy2	Simple	N
J090030.0 + 012200	1160	301774	09:00:30.1	01:22:00.2	0.35309	48.4	19.15	LIN	Simple	Y
J085849.3 + 012742	2173	376723	08:58:49.4	01:27:41.0	0.35506	46.2	18.71	SF	Simple	Y
J091435.3 – 000936	3132	575168	09:14:35.3	–00:09:35.6	0.35859	40.6	19.02	SF	Simple	N
J090450.0 – 001200	3366	574555	09:04:50.1	–00:12:03.0	0.35401	40.3	18.93	Sy2	Disturbed	Y
J090707.7 + 000003	4104	210168	09:07:07.9	00:00:02.1	0.35032	46.2	19.38	LIN	Disturbed	Y
J090845.3 + 025322	5323	518630	09:08:45.3	02:53:20.0	0.35282	28.6	18.98	SF-c	Disturbed	N
J090658.6 + 020242	5347	382441	09:06:58.4	02:02:44.7	0.34744	32.7	19.01	–	Disturbed	Y
J090444.9 + 002042	5526	600545	09:04:44.9	00:20:48.2	0.34174	31.2	19.23	SF	Simple	N
J090844.8 – 002119	6216	204249	09:08:44.8	–00:21:18.0	0.35215	36.2	18.75	SF-c	Simple	N
J090402.3 + 010800	6418	372500	09:04:02.2	01:07:58.2	0.34665	31.6	18.96	LIN-c	Disturbed	Y
J090849.4 + 022557	6451	387660	09:08:49.5	02:25:56.9	0.35259	33.7	19.08	SF-c	Simple	N

Notes: Positions and redshifts refer to the optical cross-identifications from [Bourne et al. \(2016\)](#). z is the spectroscopic redshift from GAMA ([Hopkins et al. 2013](#); [Baldry et al. 2018](#)) 250 μ m flux is from the H-ATLAS DR1 release ([Valiante et al. 2016](#)). r_{pet} is the SDSS r-band petrosian magnitude from GAMA. Spectral type uses the Blue diagnostic from [Lamareille \(2010\)](#) since we only have O[II], H β and O[III] lines in the GAMA spectral range. SF-c are in the SF region but composite SF/LIN are also found here. LIN-c are in the LINER region but composite LIN/SF are also found here. Kinematic class describes whether the CO and [CII] have similar kinematics and are aligned with the optical redshift (simple), or are disturbed with multiple kinematic components or large differences in the CO and [CII] properties. SMG indicates whether a background high-redshift SMG is detected at $> 5\sigma$ in the Band 7 field.

with the PACS PSF and so measures flux in a PSF-weighted aperture. Where there was a significant difference between the two catalogues, we returned to the original H-ATLAS PACS maps and remeasured our own photometry. The four sources this applies to are marked with ^M in Table 5. Spectroscopic redshifts and UV-22 μ m photometry are provided by the Galaxy and Mass Assembly (GAMA) survey ([Driver et al. 2011](#); [Liske et al. 2015](#); [Wright et al. 2016](#)).

In order to fulfil the requirements of the ALMA Cycle 1 call where only Band 7 and Band 3 were available, all the sources had to be within 12 deg of each other on the sky and had to be observed with no more than five tunings. This meant that only sources in a very limited redshift range around $z = 0.34 - 0.36$ could be selected in order to be able observe ¹²CO(1 – 0) and [CII](³P₁–³P₀). We selected *all* the H-ATLAS SDP sources within this redshift range, making this sample of twelve representative of sources from a blind 250 μ m selected sample at $z \sim 0.3 - 0.4$. Details of the sample are given in Table 1.

2.1 Properties of the 250 μ m selected galaxies

Earlier studies have shown that the 250 μ m population is evolving rapidly over the $0 < z < 0.5$ interval ([Dye et al. 2010](#); [Dunne et al. 2011](#)) and so we note that this sample probes an era where the galaxies were more IR luminous and gas and dust rich than those at $z = 0$. The sample has a narrow range of $L_{\text{IR}} = 1.2 \times 10^{11} - 6 \times 10^{11} L_{\odot}$ making them far more ‘typical’ of galaxies at this redshift than previous very luminous IR samples (e.g. [Combes et al. 2011](#)). At these IR luminosities the sample should be dominated by galaxies which are forming stars under normal conditions, rather than displaying the properties of extreme star-bursts ([Sargent et al. 2012](#)). The star-formation rates are between 4–26 $M_{\odot} \text{ yr}^{-1}$ and stellar masses are in the range $M_{*} = 4 \times 10^{10} - 3 \times 10^{11} M_{\odot}$. A comparison with optically selected galaxies in the same redshift range from the GAMA survey ([Driver et al. 2016](#); [Baldry et al. 2018](#)) is shown in Figure 1. The magenta solid and dashed lines

show the ‘main sequence’ fit from [Speagle et al. \(2014\)](#) with ± 0.3 dex intrinsic scatter. Most of the sample lies within the 0.3 dex scatter of the galaxy star forming main sequence at $z = 0.35$ (when allowing for the measurement errors), and three sources are above the main sequence by a factor 4–6 (SDP.3132, SDP.6216, SDP.6451). It is also apparent that the 250 μ m selection picks out the leading edge of the optical cloud of galaxies, i.e. only the most massive or highly star forming galaxies at this redshift make it above the *Herschel* flux limit.

Three colour optical/near-IR images of our sample from VST Kilo Degree Survey ([de Jong et al. 2017](#)) and VISTA VIKING, ([Edge et al. 2013](#)) are shown in Figure 4–15 and the optical spectra from GAMA ([Baldry et al. 2018](#)) are shown in Figure C1–C6. The galaxies have a range of morphologies and colours, from compact to disk-like, with many displaying signs of disturbance such as stellar caustics and asymmetric morphology. The optical spectra predominantly show an older stellar population with superimposed emission lines indicating ongoing star formation, similar to that seen in stacked spectra in the much larger H-ATLAS sample analysed by [Eales et al. \(2018\)](#). One source (SDP.6216) has a clear starburst signature in the optical spectrum, and it also has the highest offset from the main sequence in Figure 1.

Metallicity is a property which affects the emission of all three gas tracers, but its most complicated effects are on CO because of a combination of non-linear FUV photon shielding effects (Pak et al. 1998; Bolatto et al. 1999; Wolfire et al. 2010).² The effects on [CII] and dust emission are more straight-forward and the abundances of these tracers are roughly proportional to metallicity. We cannot directly estimate metallicities for our galaxies as their optical spectra do not extend as far into the red as H α at this redshift, i.e. there are no strong line-based methods available to measure metallicity directly (without H α to correct

² The recently explored effect of CRs only compound these difficulties (Bisbas et al. 2015; Bisbas, van Dishoeck et al. 2017).

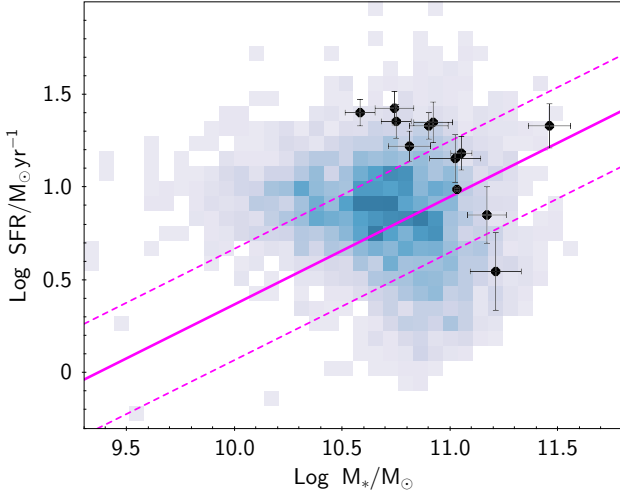


Figure 1. SFR versus stellar mass for the $z = 0.35$ sources with the best fit Main Sequence (solid) and ± 0.3 dex intrinsic scatter (dashed lines) from Speagle et al. (2014). The coloured region represents the density of galaxies in the range $0.33 < z < 0.36$ with $\log \text{sSFR} > -11.0$ and $\sigma_{M_*} < 0.15$, $\sigma_{\text{SFR}} < 0.2$ from GAMA (Driver et al. 2016). This also shows the effect of the $250\mu\text{m}$ selection at this redshift, where we sample the leading edge of the distribution in SFR- M_* for the optical selection $r < 19.8$ from GAMA. Most of the $250\mu\text{m}$ sample is consistent with the expected MS at this redshift, however, three of the lowest mass galaxies lie above the relation (SDP.3132, SDP.6216 and SDP.6451).

for reddening we would not trust methods which use only the ratios of H β , O[III] and O[II] in this dust selected sample). Fortunately, since we have a sample of massive galaxies with $\log M_*/M_\odot > 10.5$, we can use the fact that the mass metallicity relation flattens at this mass in this redshift range, hence we expect these galaxies to have metallicities between $0.8\text{--}1.2 Z_\odot$ using a variety of metrics measured at this redshift (Vale Asari et al. 2009; Lara-López et al. 2010; Bothwell et al. 2016; Torrey et al. 2019). In this metallicity range we do not expect any of the molecular gas tracers to be adversely impacted because of metallicity and thus we do not consider metallicity-dependence within our sample any further.

2.2 ALMA observations and data reduction

Choosing an observing set-up to cover both the $^{12}\text{CO}(1-0)$ and $[\text{C}\text{I}](^3\text{P}_1\text{--}^3\text{P}_0)$ lines with only Band 3 and Band 7 receivers available led to a severe restriction on the redshift of sources which could be observed in Cycle 1. Unfortunately, due to this restricted receiver choice the $[\text{C}\text{I}](1-0)$ spectral window had to be placed in the wings of an atmospheric water line, thus the transmission in the $[\text{C}\text{I}]$ window is lower than that in the other three used for the continuum (Figure 2). The Band 3 base-bands were placed as close to the edge of the band as possible in order to maximise the transparency at the $[\text{C}\text{I}](1-0)$ frequency. With a wider choice of receivers, observations with much improved sensitivity to the $[\text{C}\text{I}](1-0)$ line are now possible.

Observations were made with the ALMA-12 m array in the C32-2 and C32-3 configurations for Band 3 and the

C43-1/2 configuration for Band 7. This produced beam sizes (with natural weighting) of $\theta_3 = 2.4'' \times 1.8''$ and $\theta_7 = 1.03'' \times 0.64''$. The u, v coverage for the two set-ups is shown in Figure 3, where there is clearly more sensitivity on longer base-lines (smaller angular scales) in Band 7 compared to Band 3, while the Band 3 observations have relatively more short baselines (more sensitivity to extended structure). There are fewer missing short-spacings in the u, v coverage³ the $\text{CO}(1-0)$ compared to the $[\text{C}\text{I}](1-0)$ images, which results in better sensitivity to larger angular scales in the $\text{CO}(1-0)$ maps compared to those for $[\text{C}\text{I}]$ and dust. The implications of this are discussed further in Section 3.3.

The Band-3 observations of the $^{12}\text{CO}(1-0)$ line ($\nu_{\text{rest}} = 115.27$ GHz) were made in Dec 2013 during Cycle 1, the spectral setup consisted of four 2-GHz bandwidth spectral windows (spws): one spw with 976 MHz channel width centered at 85.4 GHz covering the $^{12}\text{CO}(1-0)$ line, and three spw with 31.25 MHz channel width, centered at 87.4, 87.5 and 99.3 GHz for the continuum. The total integration time was 96 minutes, giving $\sigma_{\text{line}} = 0.9$ mJy beam $^{-1}$ in a 50 km s^{-1} channel and $\sigma_{\text{cont}} = 40 \mu\text{Jy beam}^{-1}$. The Band-7 observations of $[\text{C}\text{I}](^3\text{P}_1\text{--}^3\text{P}_0)$ and dust continuum were split across Cycles 1 and 2 over a period from December 2013–January 2015. The spectral setup again consisted of four 2-GHz bandwidth spectral windows, one with 976 MHz channel width centered on the $[\text{C}\text{I}](^3\text{P}_1\text{--}^3\text{P}_0)$ line ($\nu_{\text{rest}} = 492.16$ GHz) and the other three with 31.25 MHz channel width at lower frequencies offset by -2, -12, -14 GHz from the high resolution spw. Four different central frequencies for the $[\text{C}\text{I}](^3\text{P}_1\text{--}^3\text{P}_0)$ spw were used, depending on the redshifts of the sources: 366.8, 365.2, 363.5 and 362.3 GHz. The total integration time was 3.9 hours giving $\sigma_{\text{line}} = 0.8\text{--}1.2$ mJy beam $^{-1}$ in a 50 km s^{-1} channel and $\sigma_{\text{cont}} = 65\text{--}90 \mu\text{Jy beam}^{-1}$.

The 3-mm Band 3 data were reduced manually using the Common Astronomy Software Applications (CASA) v4.5 package (McMullin et al. 2007). The starting points were the observatory scripts delivered with the data, but these needed to be adapted due to early issues in Cycle 1, such as too much data being flagged in some cases and extra flagging needed in other regions. Flux calibration was from Mars and the phase/bandpass calibrator J0854+2006 was used. The two measurement sets (MS), which were observed on the same day, were concatenated before imaging having been set to a common flux scale. The $^{12}\text{CO}(1-0)$ spectral line cubes were created using CLEAN in CASA in a range of channel widths in order to determine the best SNR for each source. Any emission detected was cleaned on a channel-by-channel basis. Natural weighting was used in order to maximise signal-to-noise.

The Band 7 observations were set up in four Scheduling Blocks (SBs) where the sources that could share a single tuning were grouped into a given SB. This means that the $[\text{C}\text{I}](^3\text{P}_1\text{--}^3\text{P}_0)$ line is not always placed in the centre of the spectral window. Occasionally both the line and neighbouring continuum spw had to be imaged together to provide a good baseline for line fitting. Due to some of these data being taking during Cycle 2, the newer CASA v4.7 was used for the

³ which are always present for interferometric observations without total power measurements

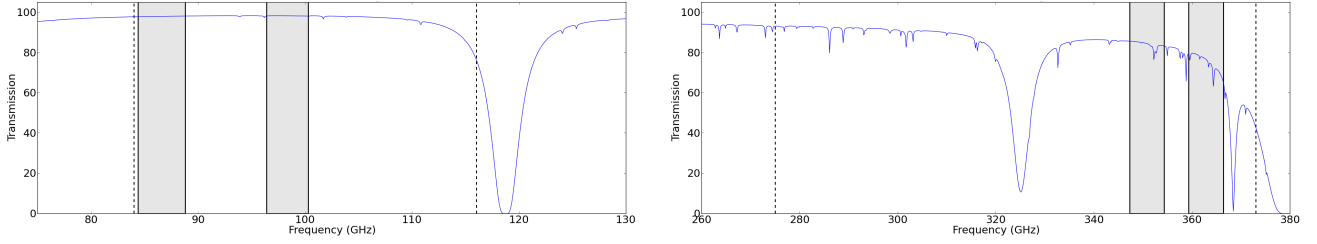


Figure 2. The spectral set-up for the observations. Band 3 (left) for $^{12}\text{CO}(1-0)$ and Band 7 (right) for dust continuum and $[\text{C}\text{I}](^3\text{P}_1-^3\text{P}_0)$. The atmospheric curve is shown for the average pwv over the Band 7 observations (0.84mm). The solid shaded bands are the range of frequencies in which we observed lines and continuum, the vertical dashed lines represent the limits of the ALMA bands. There is only a *very* small range of redshift in which this experiment was possible due to the availability of receiver bands at the Cycle 1 call.

Table 2. Details of the ALMA observing.

SB name	ν_{obs} (GHz)	Date	EB	N_{ant}	t_{int} (min)	p.w.v (mm)	Phase Cal.	Flux Cal.	B.P.	σ_{cont} (μJy)	σ_{line} (mJy)
B3	85.5	3.12.13	Xe20	26	48.4	4.14	J0854 + 20	Mars	J0854 + 20	40	0.9
		3.12.13	X1032	26	48.4	4.14	J0854 + 20	Callisto	J0854 + 20		
LowV (163, 4104, 5347, 6418)	365.2	14.12.13	X1644	26	50.2	0.84	J0854 + 20	Pallas	J1058 + 01	90	0.86 – 1.2
		26.12.14	X2543	40	33.3	0.84	J0909 + 01	Ganymede	J0825 + 03	..	
SDP.5526	366.8	21.2.14	X5fa	27	12.0	0.46	J0909 + 01	Pallas	J0825 + 03	77	1.25
		26.12.14	X23cb	40	8.0	1.15	J0909 + 01	Ganymede	J0825 + 03	..	
SDP.3132	362.3	14.12.13	Xf8d*	30	5.5	1.10	J1007 – 02	Ganymede	J0504 – 44	70	0.87
		2.1.15	X1ba4	39	5.5	0.70	J0909 + 01	J0750 + 12	J0825 + 03	..	
		2.1.15	X1cf1	39	5.5	0.72	J0909 + 01	Callisto	J0909 + 01	..	
HighV	363.5	21.2.14	X3e5	28	35.3	0.64	J0914 + 02	Ganymede	J0825 + 03	65	0.84 – 1.1
(1160, 2173, 3366, 5323, 6216, 6451)		2.1.15	X1e75	39	34.2	0.69	J0909 + 01	Callisto	J0825 + 03	..	
		2.1.15	X2365	39	15.4	0.82	J0909 + 01	Ganymede	J0825 + 03	..	
		2.1.15	X2606	39	34.2	0.91	J0909 + 01	Ganymede	J0909 + 01	..	

σ_{cont} is the average rms in $\mu\text{Jy}/\text{beam}$ for the continuum. * M.S. not used as it did not improve the overall noise level or image quality.

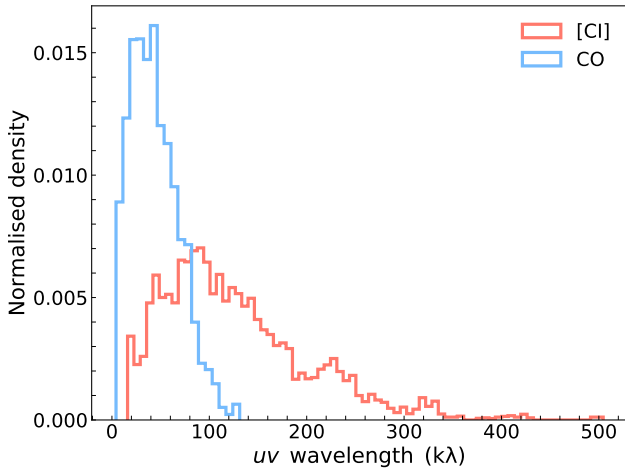


Figure 3. The distribution of (u,v) separations in $k\lambda$ for the array configurations used to observe CO(1-0) (blue) and $[\text{C}\text{I}](1-0)$ and dust (red). The (u,v) coverage is very different. The $[\text{C}\text{I}]$ u-v coverage contains high spatial frequency information (i.e. high resolution information) that CO lacks and, conversely, the CO(1-0) u-v coverage retains spatial sampling in the shortest spacings, meaning more sensitivity to larger spatial scales than $[\text{C}\text{I}]$. The inner gap in the (u,v) coverage for $[\text{C}\text{I}]$ and dust at these small spacings results in a filtering of the larger spatial scales, which would result in a loss of $[\text{C}\text{I}]$ and dust continuum brightness distribution relative to that of CO(1-0) if there is extended gas and dust on scales larger than 25 kpc.

reduction. Some of the MS were calibrated using the ALMA pipeline, while others were reduced manually, depending on how the data were delivered. All MS were checked and reprocessed allowing for tailoring of the calibration to the specific issues in this data-set. For example, there are several atmospheric lines which are evident in the Band 7 data and so the pipeline calibration was modified to avoid flagging the T_{sys} response in some cases, and to output the data-set from the pipeline after the generation of the water vapour radiometer (WVR) and T_{sys} calibration tables. The data were then manually processed from that stage so that the atmospheric lines could be flagged in the bandpass calibrator and the bandpass solutions interpolated in these regions. Additional manual flagging was also applied where required.

Imaging of the $[\text{C}\text{I}](^3\text{P}_1-^3\text{P}_0)$ line and continuum was performed using the CASA task `TCLEAN` with a Hogbom algorithm, using natural weighting. The dust continuum emission at 350 – 360 GHz (rest-frame ~ 480 GHz) was imaged using the line-free portions of the data. Images were made at full resolution ($\theta_7 = 1.03'' \times 0.64''$) and also tapered in the uv -plane to increase the sensitivity to any low level extended emission. The optical diameter of the galaxies is $4-9''$, and so they are expected to be resolved in our observations. Sources above 3σ in the dirty image were masked and lightly cleaned (to 1.5σ).

Spectral line cubes were created using velocity channels chosen on the basis of the lines found (ranging from 30–150 km s^{-1}). Line emission above 3σ detected in the dirty image was masked in each channel individually and cleaned

down to 1.5σ . If the continuum emission was strong, it was subtracted from the cube using the CASA task IMCONTSUB, this was only necessary in the case of SDP.163 as in all other sources the peak continuum emission was much less than the rms in the line channels. We searched near the optical redshift for emission, also taking account of any neighbouring optical sources which may have been at a similar redshift and interacting with the main source (as turned out to be the case for four targets). The cubes were collapsed to make a moment 0 map across the velocity range where line emission was seen using the IMMOMENTS task in CASA.

Images are presented in Figure 4–15 and are not corrected for the variable attenuation of the primary beam over the field, being displayed instead as signal-to-noise contours.⁴

2.3 Flux measurements.

Continuum fluxes were measured on either the full resolution or tapered maps depending on the source size and morphology. For the most accurate fluxes we fitted Gaussians, using the CASA tasks IMFIT and GAUSSFIT where possible, which meant using the tapered maps for the more extended sources and the full resolution maps for any point like sources. Where a source was reported to be unresolved or no size could be measured, we opted to use the peak flux, which is equivalent to that derived when fixing the size parameters to be equal to those of the beam. When a source was resolved and had a peak SNR > 5, we used the integrated flux from the Gaussian fit, while for extended sources where a Gaussian was not a good representation, or when the SNR was less than 5, we used an aperture around the source emission (e.g. Simpson et al. 2015; Oteo et al. 2016).

When fitting fluxes using IMFIT or GAUSSFIT, we used only a small region to actually solve the fit parameters as this makes the fitting less unstable. However, the flux error returned by the algorithm in CASA is usually underestimated due to the presence of correlated noise in the map pixels (Condon 1997). To deal with this, we first measured σ_{true} , the pixel rms noise on the *non* primary-beam-corrected image, over a large enough region to be a true representation. We then derived the correct fractional errors on the flux output by the CASA fitting task using the following equation:⁵

$$\frac{\delta S}{S} = \sqrt{\left(\frac{\delta A}{A}\right)^2 \left(\frac{\sigma_{\text{true}}^2}{\sigma_{\text{alg}}^2} - 1\right) + \left(\frac{\delta I}{I}\right)^2} \quad (1)$$

where $\delta A/A$ and $\delta I/I$ are the fractional error on the amplitude and integrated flux returned by the algorithm.

The amplitude error is underestimated if too small a region is used by the algorithm to determine the map rms, and so we correct this using the ratio of our own measure-

ment of the noise σ_{true} to the rms used by algorithm in its determination of the errors (σ_{alg}).⁶

For the aperture measurements, we estimated the noise using the formulation in Dunne et al. (2000) which accounts for correlated noise:

$$\sigma_{\text{ap}} = \sigma_{\text{pix}} \times \sqrt{N_{\text{ap}}/N_{\text{beam}}}$$

where σ_{ap} is the noise in an aperture which has N_{ap} pixels. σ_{pix} is the pixel to pixel rms measured in large off-source regions of the map and N_{beam} is the number of pixels in the beam. This is equivalent to putting down random apertures on the map and estimating the variance of their sums (assuming the noise is Gaussian other than the beam scale correlations).

We corrected the aperture measurements for the fraction of the beam falling outside the aperture by comparing the fluxes within the same aperture placed on the phase calibrator with that returned by the IMFIT task in CASA, following the method outlined in Simpson et al. (2015).

Integrated line fluxes were calculated in a similar way to the continuum fluxes, either by fitting a Gaussian to the moment 0 image, or using an aperture if that was more appropriate. No thresholding was applied to the moment 0 maps to avoid biasing the fluxes. All fluxes and errors were then corrected for the primary beam attenuation using the primary beam model output by CASA during the CLEAN stage. The integrated line intensities and other observational parameters for CO are listed in Table 3, and those for [C_I] and dust are found in Table 4.

Spectral profiles were extracted either from the peak pixel of a point source, or from the aperture which covered the region of interest. The profiles were baseline subtracted, boxcar or Hanning smoothed in some cases and fitted with a Gaussian line profile. The profiles are shown in Figures 4–15 and the fitted parameters are listed in Tables 3 and 4.

3 RESULTS

We detect a total [C_I] flux above 3σ for all 12 sources, for dust continuum the number is 11 and for CO we detect at this level in 10 sources. There are a wide variety of morphologies and relative luminosities. The optical images with ALMA signal-to-noise contours superimposed are shown in Figures 4–15 along with the CO and [C_I] spectral profiles. We comment in detail on each source in Appendix A.

Half of the fields contained one or more serendipitously detected high redshift dusty star-forming galaxies, identifiable as point sources with SNR > 5 and having either no optical/NIR counterpart, or a very red K-band detection in the VIKING imaging. In total 7 high redshift dusty galaxies are confidently detected at $S_{850} > 5\sigma$ in 6 fields. A full investigation of these sources, which constitute an overdensity relative to the blank field counts of a factor 4–6 is given by Dunne et al. (2020).

⁴ It should be noted that a source nearer to the edge of the map will have a higher flux at the same contour level compared to a source in the centre, due to the fact that the primary beam attenuation increases the noise as a function of radius from the pointing centre.

⁵ This is based on Condon (1997).

⁶ In IMFIT one can simply supply σ_{true} to the task, thus overriding the noise estimate from the smaller region over which the fit is to be performed.

Table 3. Details of the Band 3 CO measurements

Source	R.A. (J2000)	Dec (J2000)	δv_{CO} (km s^{-1})	Δv_{CO} (km s^{-1})	S_{10} (Jy km s^{-1})	FWHM (km s^{-1})
163	09:05:06.19	+02:07:02.2	80	14 ± 53	1.60 ± 0.28^a	728 ± 129
1160	09:00:30.13	+01:22:00.4	100	39 ± 22	0.70 ± 0.13^g	296 ± 53
2173	08:58:49.36	+01:27:41.4	50	-34 ± 8	0.84 ± 0.20^a	147 ± 19
3132	09:14:35.28	-00:09:35.7	15	9 ± 4	0.70 ± 0.12^g	59 ± 10
3366	09:04:50.10	-00:12:03.6	50	54 ± 11	0.38 ± 0.12^g	205 ± 27
4104.a	09:07:07.85	+00:00:02.4	60	-72 ± 14	0.85 ± 0.25^g	222 ± 32
4014.b	09:07:07.82	+00:00:05.1	60	-366 ± 18	0.78 ± 0.15^g	176 ± 43
5323	09:08:45.32	+02:53:21.2	80	-114 ± 31	0.80 ± 0.20^{gt}	462 ± 74
5347	09:06:58.22	+02:02:45.73	80	218 ± 17	2.29 ± 0.56^a	417 ± 40
5347(S)	09:06:58.63	+02:02:35.87	80	206 ± 20	1.90 ± 0.45^a	859 ± 120
5526	09:04:44.88	+00:20:48.2	50	-7 ± 7	1.04 ± 0.20^g	148 ± 16
6216	09:08:44.79	-00:21:17.9	50	20 ± 13	0.70 ± 0.11^{gt}	259 ± 30
6418	09:04:02.15	+01:07:58.9	75	178 ± 53	0.27 ± 0.14^g	124 ± 72
6451	09:08:49.2	+02:25:57.8	50	0	0.27 ± 0.11^{gp}	300
			50	-50	0.40 ± 0.19^a	200

Each component found is listed on an individual line. ^a or ^g next to the flux indicate whether an aperture was used or a Gaussian fit, although where both methods could be used they gave comparable results within the errors. ^t indicates the measurement was made on the tapered map. Bold font indicates measurements with integrated flux at $< 3\sigma$. Details on individual source measurements can be found in Section A.

SDP.5347 has two or three optical components and it is difficult to disentangle the CO emission. The sources appear to be merging and there is CO emission at a similar velocity outside the optical disks which may be tidal remnants. The first row includes emission from the three optical components which have similar velocities. The second row (S) is the clump of emission to the South which can be seen in Figure 11. This southern emission is not used in any further analysis. 6451 has very weak CO emission over a velocity range $-150 \text{ km s}^{-1} \rightarrow -50 \text{ km s}^{-1}$. The first entry in the table above is the peak flux from fitting a Gaussian to the brightest peak coincident with the [C I] peak. The second entry is using an aperture which covers the same area as that used to measure the [C I] flux in Table 4.

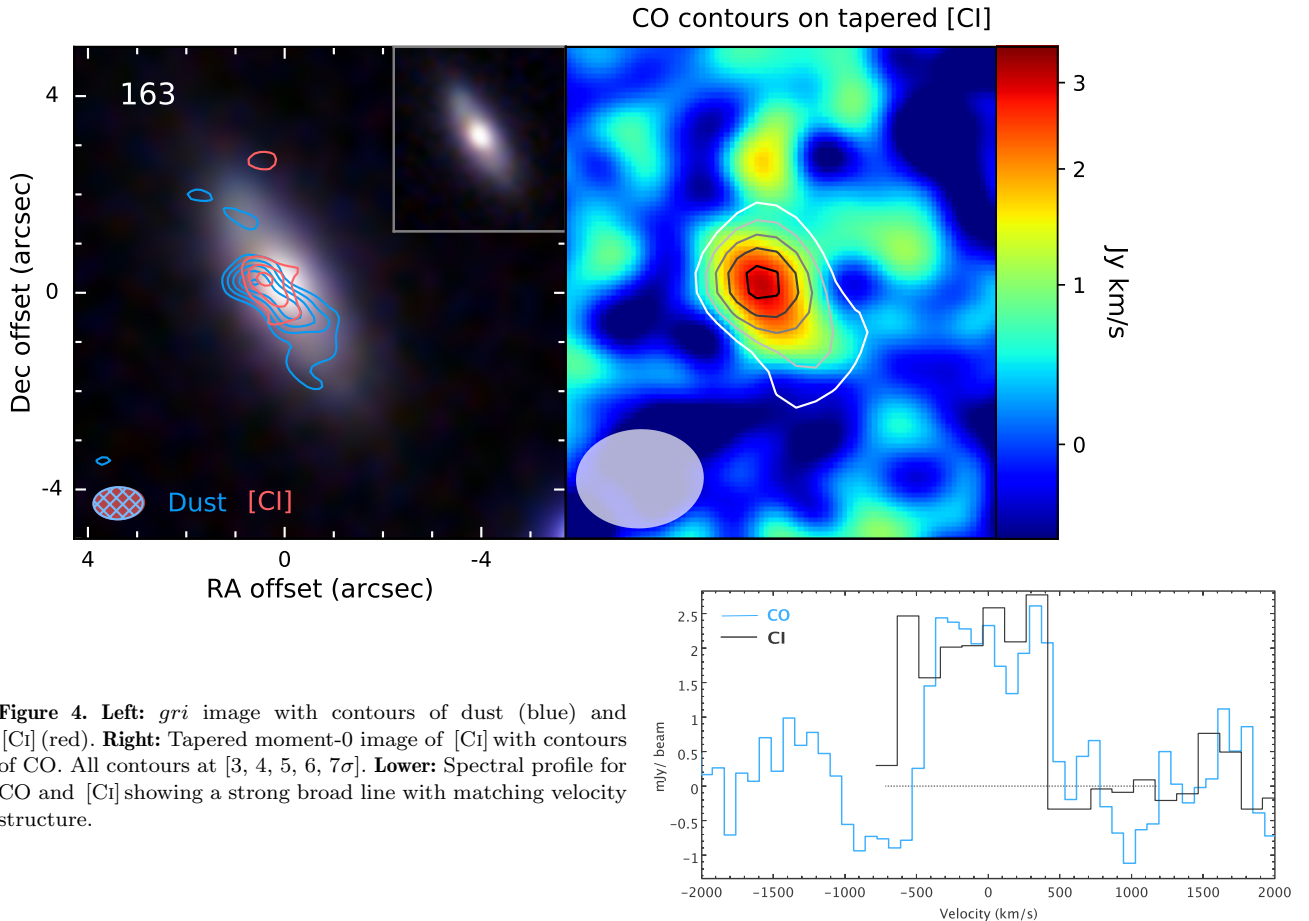


Figure 4. Left: *gri* image with contours of dust (blue) and [C I] (red). Right: Tapered moment-0 image of [C I] with contours of CO. All contours at $[3, 4, 5, 6, 7\sigma]$. Lower: Spectral profile for CO and [C I] showing a strong broad line with matching velocity structure.

Table 4. Details of the Band 7 CI and continuum measurements

Source	R.A. (J2000)	Dec (J2000)	δv_{CI} (km s^{-1})	Δv_{CI} (km s^{-1})	S_{CI} (Jy km s^{-1})	FWHM (km s^{-1})	S_{λ} (mJy)	λ (μm)
163	09:05:06.11	+02:07:01.9	150	-28 ± 74	8.3 ± 1.3^a	829 ± 293	3.05 ± 0.34^a	837.18
1160	09:00:30.15	+01:22:00.2	50	2 ± 18	3.00 ± 0.27^g	383 ± 43	0.54 ± 0.12^{gt}	840.27
2173	08:58:49.31	+01:27:41.3	30	-30 ± 5	3.31 ± 0.48^a	125 ± 12	0.74 ± 0.20^{gt}	840.69
3132 3132 ^{+ACA}	09:14:35.28	-00:09:35.7	20	7 ± 4	2.32 ± 0.38^a 2.57 ± 0.38^a	73 ± 10	0.95 ± 0.29^a 1.51 ± 0.39^a	843.98
3366.a.v1	09:04:50.13	-00:12:03.6	100	2 ± 14	1.77 ± 0.49^{gt}	196 ± 33	0.42 ± 0.19^{gt}	840.29
(3366.a.v2)	09:04:50.09	-00:12:03.0	100	-363 ± 11	1.06 ± 0.28^{gt}	305 ± 27
(3366.b)	09:04:50.21	-00:12:01.0	100	-145 ± 27	0.78 ± 0.20^g	727 ± 63	0.20 ± 0.054^g	840.29
4104.a	09:07:07.85	+00:00:02.4	50	-138 ± 44	1.60 ± 0.53^a 2.41^c	354 ± 102	0.46 ± 0.21^a	835.31
4104.b	09:07:07.82	+00:00:05.1	50	-61 ± 33	1.02 ± 0.30^g 1.13^c	421 ± 82	0.46 ± 0.12^g	835.31
5323.v1	09:08:45.30	+02:53:21.7	80	-273 ± 34	1.35 ± 0.38^{gt}	330 ± 84	0.89 ± 0.24^a	841.43
5323.v2	09:08:45.30	+02:53:21.7	80	107 ± 18	0.54 ± 0.15^g	390 ± 95
(5323.v3)	09:08:45.29	+02:53:20.9	80	1239 ± 13	2.37 ± 0.46^{gt}	325 ± 30
5347.a	09:06:58.45	+02:02:45.2	80	-219 ± 19	3.49 ± 0.91^{at}	480 ± 112	0.39 ± 0.13^{gt}	849.38
5347.bc	09:06:58.22	+02:02:47.6	80	-790 ± 16	0.82 ± 0.19^{gt}	179 ± 36	0.38 ± 0.11^g (b)	849.38
5347.bc	" "	" "	80	110 ± 28	1.11 ± 0.32^{gt}	305 ± 67	1.16 ± 0.29^{gt} (c)	849.38
(5347.S)	09:06:58.56	+02:02:39.3	80	-47 ± 20	1.31 ± 0.33^{gt}	349 ± 47	0.54 ± 0.24^g	849.38
5526	09:04:44.88	+00:20:48.2	50	-76 ± 13	2.07 ± 0.28^{gt}	217 ± 30	1.11 ± 0.27^{gt}	833.32
6216 (min)	09:04:02.15	-00:21:17.9	50	-22 ± 11	2.02 ± 0.36^{gt}	191 ± 25	1.49 ± 0.25^a	841.44
(max)			50				1.02 ± 0.26^a	..
			50				2.18 ± 0.41^a	..
6418.a	09:04:02.14	+01:08:00.4	75	249 ± 19	4.62 ± 0.64^a	290 ± 44	1.06 ± 0.32^a	835.33
(6418.v1)			75	-452 ± 19	1.23 ± 0.29^{gt}	148 ± 43	..	
6418.v2			75	$+249 \pm 17$	2.66 ± 0.51^a	289 ± 41	..	
(6418.v3)			75	$+503 \pm 37$	0.73 ± 0.26^{gt}	282 ± 88	..	
(6418.b)	09:04:02.37	+01:07:58.5	75	-369 ± 14	1.24 ± 0.28^{gt}	314 ± 34	0.24 ± 0.11^{gt}	835.33
6451	09:08:49.49	+02:25:57.6	50	-24 ± 13	4.46 ± 0.97^a	200 ± 30	0.88 ± 0.19^{gt}	841.44

The positions and fluxes of the various components are listed with the following nomenclature: Spatially distinct components which are identified with separate optical sources are given letters to denote them. Kinematically distinct components in the same source are denoted as v_i . The components which are used to derive the physical properties such as luminosity and gas mass in Tables 6 and 7 are shown without brackets, while those inside brackets are not used.

^a or ^g next to the flux indicate whether an aperture was used or a Gaussian fit, although where both methods could be used they gave comparable results within the errors. ^t indicates the measurement was made on the tapered map. Measurements at $< 3\sigma$ are in bold.

For details on the individual entries please see notes in Appendix A.

3132 had ACA data taken in Cycle 7 and the inclusion of this leads to the second row of fluxes denoted ^{+ACA}.

3366 has three components: the main optical galaxy 3366.a has two associated velocity components, v_1 and v_2 while the small blue companion, 3366.b, has a broad line which overlaps the velocity profile of 3366.a.v2.

4104 (interacting pair) has spatially and kinematically resolved components in both CO and [C I].

5323 has three velocity components: north of the nucleus $v_1 = -273 \text{ km s}^{-1}$, south of the nucleus ($v_2 = +100 \text{ km s}^{-1}$), and high velocity emission $v_3 = 1239 \text{ km s}^{-1}$ (Fig. 10). There is no corresponding CO emission for the high velocity component, and we do not consider it further.

5347 ‘a,b,c’ refer to the main optical galaxy, the satellite seen to the west within the optical isophotes of the main galaxy with the strongest CO peak, and the satellite visible to the north-west respectively. 5347.S is a clump of emission to the South which overlaps in velocity with the clump seen in CO.

6216 is an extended source with complex continuum morphology, three continuum fluxes are given. The first includes all the emission except for the Eastern arm-like extension. The second is a robust minimum flux which subtracts the compact clump discussed in Appendix A, and does not include the Eastern extension. The third is a robust maximum which includes all three components.

6418.a is the main optical target, and the next three rows are the three velocity components v_1, v_2, v_3 , the sum of which constitutes the flux for 6418.a. The smaller optical companion, 6418.b, has very low SNR $850 \mu\text{m}$ continuum flux but has [C I] at the same -400 km s^{-1} velocity as the 6418.a(v_1).

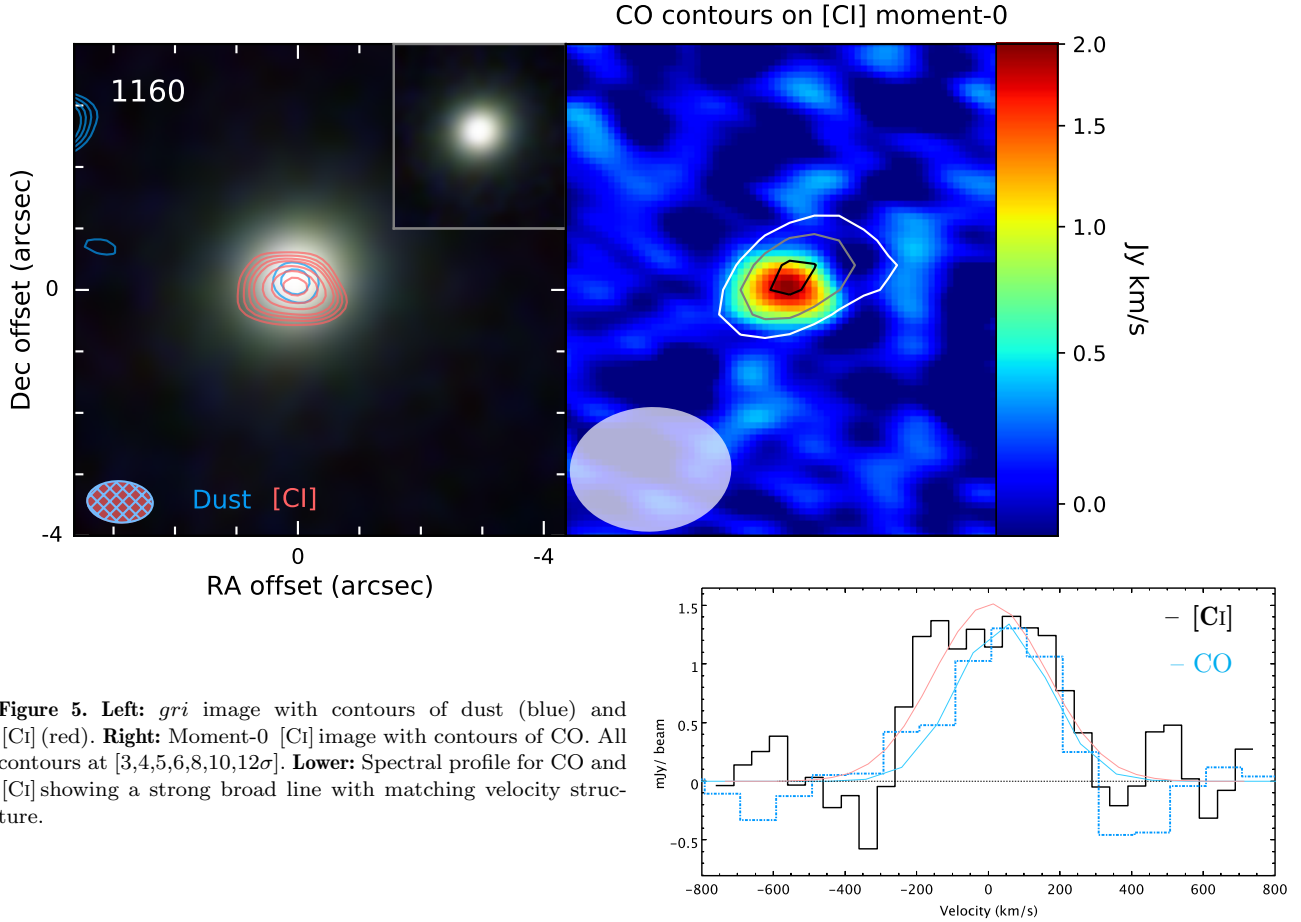


Figure 5. *Left:* *gri* image with contours of dust (blue) and [CI] (red). *Right:* Moment-0 [CI] image with contours of CO. All contours at $[3,4,5,6,8,10,12\sigma]$. *Lower:* Spectral profile for CO and [CI] showing a strong broad line with matching velocity structure.

3.1 Physical parameters from SED fitting

We have estimated physical parameters for the galaxies using the energy balance SED fitting code MAGPHYS, which uses libraries of optical and infrared SEDs with parameters drawn stochastically from physically motivated priors. Details of the fitting method are presented in [da Cunha et al. \(2008\)](#). We use extended infrared libraries which have an ISM cold temperature range of 10–30 K ([Rowlands et al. 2014](#); [da Cunha et al. 2015](#)), as several of the sources favoured warmer ISM temperatures than allowed in the standard MAGPHYS infrared libraries. We fit the FUV–850 μ m photometry (typically 22 or 23 bands), including an additional 7% error in quadrature to incorporate calibration, zero point and model scatter. The FUV–22 μ m photometry is taken from the LAMBDAR catalogue ([Wright et al. 2016](#)), while the *Herschel* photometry is listed in Table 5. We take the *IRAS* SCANPI ([Helou et al. 1988](#)) upper limits at 60 μ m and use them as a constraint on the fitting. In several cases there is contamination of the SPIRE photometry from background sources at higher redshift in the *Herschel* beam. Sometimes the contaminant source is visible in the ALMA continuum images, other times it is evident from the 250 μ m/350 μ m and 350 μ m/500 μ m colours that another higher redshift source must be contributing to the SPIRE fluxes. We describe in Appendix B and in [Dunne et al.](#) how we estimate the range of possible contamination of the *Herschel* fluxes, in order to correct them. Where there is evidence for contamination, we have fitted the photometry

with and without making this correction to check the impact on the SED. We find that, while in all cases making these corrections improves the fit to the SED, the changes to the estimated parameters are very small and within the original 1σ uncertainties in all cases. Therefore the choice of whether to correct, or how to correct has no bearing on our findings in the next section. Our companion paper provides further detail and also investigates the wider implications of this boosting for cases where ALMA data are not present.

We show the best fit SED and parameter PDFs in Figure C1–C6. Alongside the best-fit SED in red we also show 200 of the SEDs which are strongly contributing to the PDFs. The median parameters and their uncertainties are listed in Table 6.

3.2 Kinematics

The kinematics of the sources were more complex than anticipated in many cases. In seven cases, there is a single optical galaxy where CO and [CI] have similar line-widths and velocities and similar morphology.⁷ We call these the Simple Kinematic (SK) sources. The other five sources have disturbed kinematics (DK), four of which (SDP.3366, SDP.4104, SDP.5347, SDP.6418) have a smaller neighbouring optical source which shows either CO, [CI] or both at a

⁷ As far as we can tell with the resolution differences between 85 GHz and 365 GHz.

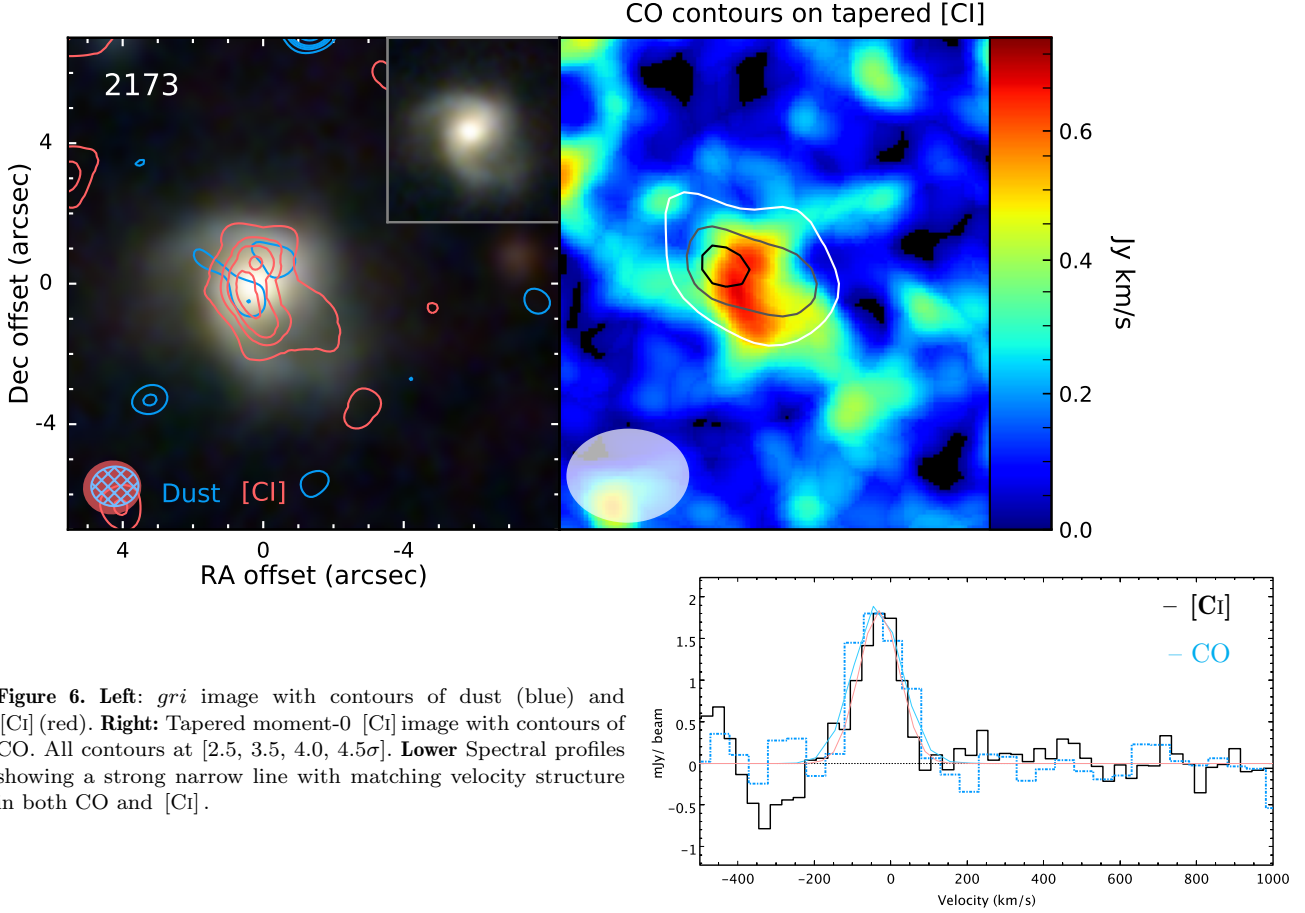


Figure 6. Left: *gri* image with contours of dust (blue) and [C_I] (red). Right: Tapered moment-0 [C_I] image with contours of CO. All contours at [2.5, 3.5, 4.0, 4.5 σ]. Lower Spectral profiles showing a strong narrow line with matching velocity structure in both CO and [C_I].

Table 5. FIR photometry for the galaxies from Herschel-ATLAS DR1 and our ALMA measurements.

Source	S_{100}	σ_{100}	S_{160}	σ_{160}	S_{250}	σ_{250}	S_{350}	σ_{350}	S_{500}	σ_{500}	S_{850}	σ_{850}
163	73.9	20.7	102.1	24.1	107.6	7.3	50.7	8.1	23.9	8.5	3.05	0.34
1160 [†]	49.8	17.5	57.1	19.7	48.4	7.2	32.4	8.1	21.6	8.7	0.54	0.12
2173 [†]	59.0 ^M	34.0	68.0 ^M	38.0	46.2	6.5	21.4	7.5	11.1	7.8	0.74	0.20
3132	64.3 ^M	26.5	65.1 ^M	20.0	40.6	6.4	23.6	7.4	13.1	7.8	0.95	0.29
3366 [†]	19.7	24.5	114	37.6	40.3	7.3	26.3	8.0	16.5	8.8	0.42	0.019
4104 [†]	77.9	17.6	53.3	26.4	46.2	7.2	28.3	8.1	12.1	8.8	0.92	0.24
5323	28.6	7.1	30.0	8.0	9.6	8.4	0.89	0.24
5347 [†]	33.0	41.2	68.0	17.7	32.7	7.5	29.8	8.2	17.2	8.7	1.84	0.35
5526	62.0 ^M	32.6	56.9 ^M	40.7	31.2	7.3	20.0	8.2	-10.7	8.5	1.11	0.27
6216	35.0 ^M	36.6	34.0 ^M	40.7	36.2	7.3	19.9	8.1	3.8	8.8	1.49	0.25
6418 [†]	40.4 ^M	19.8	27.0 ^M	33.3	31.6	7.3	18.5	8.0	16.6	8.4	1.06	0.32
6451 [†]	69.4	41.7	59.5	47.8	33.7	7.3	29.7	8.2	19.5	8.6	0.88	0.19

Notes: Fluxes are all in mJy. [†] indicates that there is evidence for contamination of these *Herschel* fluxes by high-*z* SMG in the beam. Before SED fitting we subtract from these fluxes the estimated contamination from high-*z* SMG listed in Table B1. See Appendix B for details. ^M indicates a PACS flux re-measured from the DR1 maps.

similar velocity, indicating tidal interaction. SDP.5323 has a very complex velocity field in [C_I] with three components, and may be hosting an outflow or be involved in an interaction with a satellite.

3.3 Gas and dust morphology

The ALMA Band 7 data provide 850 μ m (rest-frame 620 μ m) dust and [C_I] line imaging at a common angular resolution ($0.6 \times 1.1''$) and with the same (*u, v*) coverage, so that morphological comparisons between the [C_I] and dust are mean-

ingful. The CO imaging is at a very different frequency, which translates into different sensitivity to spatial scales within the interferometer. The smallest spatial scales probed are set by the longest baselines, and the synthesised beam with natural weighting gives a physical resolution of 10 kpc for CO(1–0), and 4 kpc for [C_I](1–0) and dust. The CO is unresolved or very marginally resolved in all sources, apart from SDP.5347, where there appears to be some large scale tidal debris.

The Maximum Recoverable Scale (MRS) for the CO imaging is of order 20''(100 kpc), while for [C_I] and dust it

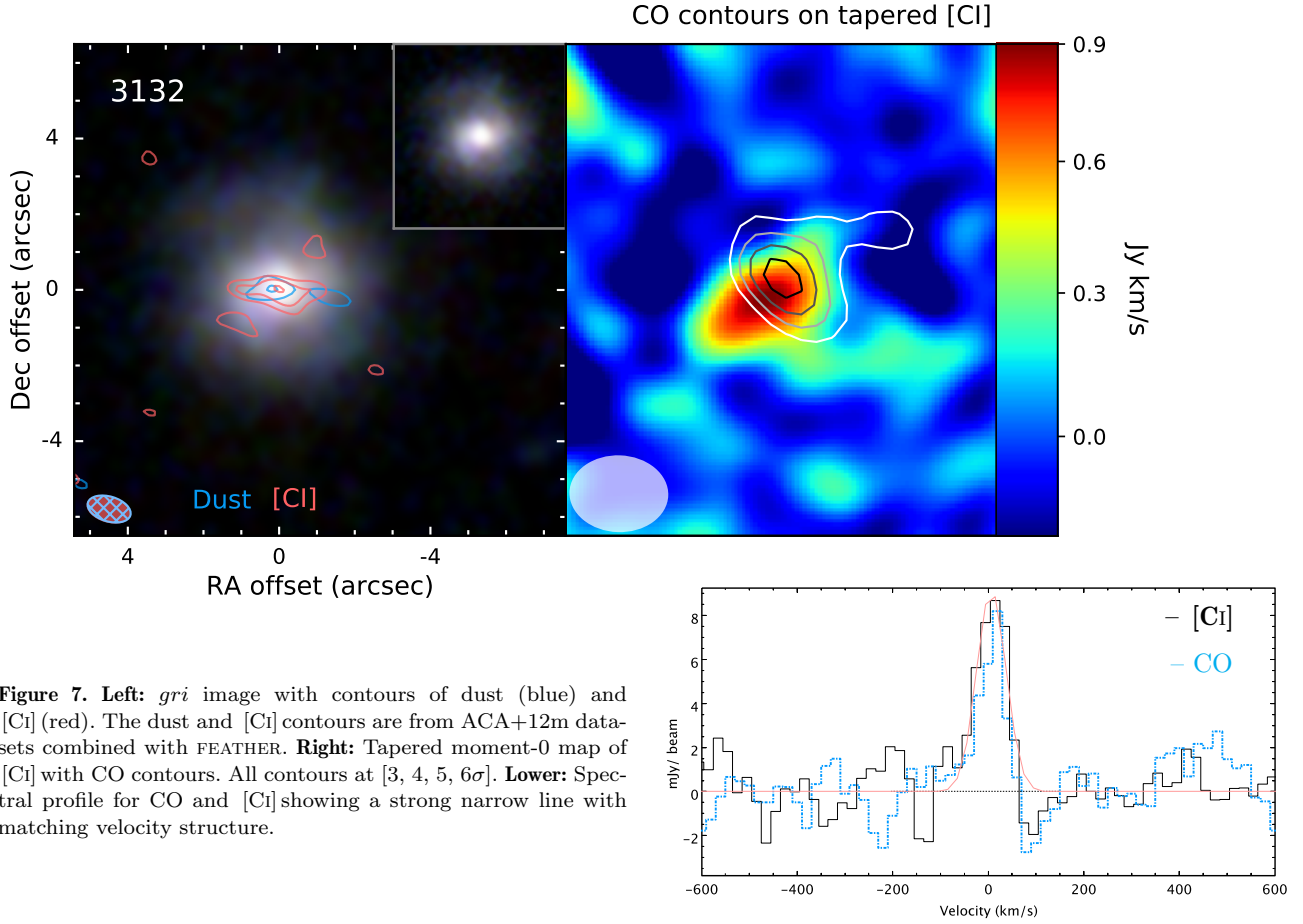


Figure 7. Left: *gri* image with contours of dust (blue) and [CII] (red). The dust and [CII] contours are from ACA+12m datasets combined with FEATHER. Right: Tapered moment-0 map of [CII] with CO contours. All contours at $[3, 4, 5, 6\sigma]$. Lower: Spectral profile for CO and [CII] showing a strong narrow line with matching velocity structure.

Table 6. Luminosities and derived physical properties from MAGPHYS SED fitting.

Source	Log L'_{CI} (K kms $^{-1}$ pc 2)	Log L'_{CO} (K kms $^{-1}$ pc 2)	Log L_{850} (W Hz $^{-1}$)	Log M_* (M_{\odot})	Log L_{IR} (L_{\odot})	Log M_{d} (M_{\odot})	log sSFR (yr $^{-1}$)	T_{C} (K)
163	9.46 ± 0.07	10.01 ± 0.08	23.51 ± 0.05	$11.46^{+0.10}_{-0.10}$	$11.66^{+0.04}_{-0.04}$	$8.60^{+0.05}_{-0.06}$	$-10.12^{+0.1}_{-0.2}$	$22.5^{+0.7}_{-0.8}$
1160 †	9.02 ± 0.04	9.65 ± 0.08	22.75 ± 0.10	$11.04^{+0.11}_{-0.10}$	$11.35^{+0.06}_{-0.10}$	$7.73^{+0.08}_{-0.08}$	$-9.98^{+0.2}_{-0.2}$	$28.3^{+1.1}_{-1.8}$
2173 †	9.06 ± 0.06	9.73 ± 0.10	22.91 ± 0.12	$10.89^{+0.09}_{-0.07}$	$11.30^{+0.10}_{-0.08}$	$7.94^{+0.12}_{-0.12}$	$-9.58^{+0.1}_{-0.1}$	$24.5^{+2.5}_{-2.3}$
3132	8.91 ± 0.07	9.65 ± 0.07	23.03 ± 0.13	$10.74^{+0.09}_{-0.09}$	$11.49^{+0.08}_{-0.07}$	$8.01^{+0.08}_{-0.07}$	$-9.33^{+0.15}_{-0.15}$	$25.9^{+2.0}_{-1.5}$
3366 †	8.79 ± 0.12	9.38 ± 0.14	22.68 ± 0.20	$11.21^{+0.12}_{-0.13}$	$11.13^{+0.10}_{-0.15}$	$7.71^{+0.15}_{-0.14}$	$-10.67^{+0.15}_{-0.3}$	$26.5^{+2.3}_{-2.7}$
4104 †	8.96 ± 0.10	10.02 ± 0.08	22.98 ± 0.11	$10.93^{+0.08}_{-0.09}$	$11.45^{+0.11}_{-0.09}$	$7.87^{+0.11}_{-0.11}$	$-9.68^{+0.2}_{-0.1}$	$27.7^{+1.3}_{-2.3}$
5323	8.91 ± 0.08	9.71 ± 0.11	23.00 ± 0.12	$11.05^{+0.05}_{-0.05}$	$11.17^{+0.12}_{-0.08}$	$8.05^{+0.17}_{-0.17}$	$-9.88^{+0.15}_{-0.1}$	$21.8^{+3.6}_{-2.7}$
5347 †	9.08 ± 0.10	10.05 ± 0.10	23.34 ± 0.08	$11.17^{+0.09}_{-0.10}$	$11.11^{+0.11}_{-0.12}$	$8.38^{+0.14}_{-0.16}$	$-10.32^{+0.2}_{-0.15}$	$19.9^{+2.2}_{-1.9}$
5526	8.86 ± 0.06	9.80 ± 0.08	23.15 ± 0.09	$10.82^{+0.03}_{-0.09}$	$11.33^{+0.07}_{-0.11}$	$7.98^{+0.13}_{-0.11}$	$-9.63^{+0.15}_{-0.1}$	$24.4^{+2.5}_{-2.8}$
6216	8.85 ± 0.08	9.65 ± 0.07	23.22 ± 0.07	$10.58^{+0.07}_{-0.06}$	$11.32^{+0.08}_{-0.10}$	$8.25^{+0.18}_{-0.18}$	$-9.18^{+0.1}_{-0.2}$	$20.0^{+3.5}_{-2.4}$
6418 †	8.97 ± 0.08	9.23 ± 0.23	23.07 ± 0.13	$10.79^{+0.12}_{-0.08}$	$11.28^{+0.10}_{-0.15}$	$8.00^{+0.19}_{-0.18}$	$-9.58^{+0.15}_{-0.1}$	$23.4^{+3.5}_{-2.9}$
6451 †	9.19 ± 0.09	9.18 ± 0.26	22.98 ± 0.09	$10.75^{+0.08}_{-0.07}$	$11.36^{+0.11}_{-0.12}$	$7.96^{+0.15}_{-0.13}$	$-9.48^{+0.15}_{-0.15}$	$25.0^{+3.0}_{-2.9}$

Notes on Luminosities 3366: [CII] is from 3366.a.v1 only. 4104: the sum of both members of the pair as measured with the missing channels. 5323: [CII] is the sum of the two velocity components v_1 and v_2 from Table 4. 5347: sum of the massive galaxy and the two satellites which have dust and/or [CII] and CO emission (5347a–c in Table 4). 6216: flux at $850\mu\text{m}$ is that from the main disk including the compact clump discussed in Appendix. A. 6418: [CII] flux is only that of the v_2 component in the main galaxy. **Notes on MAGPHYS parameters:** † Fits use sub-mm fluxes from Table 5 which are then corrected for high- z contamination where required (see Appendix B). The differences in the fitted parameters using fluxes which are corrected for estimated contamination by dusty high redshift galaxies detected by ALMA within the SPIRE beam is well within the 1σ error and so the consideration of contamination has a negligible effect on the properties derived here. The dust mass estimates using the ALMA data in addition to the *Herschel* fluxes are considerably lower than when using the *Herschel* data alone.

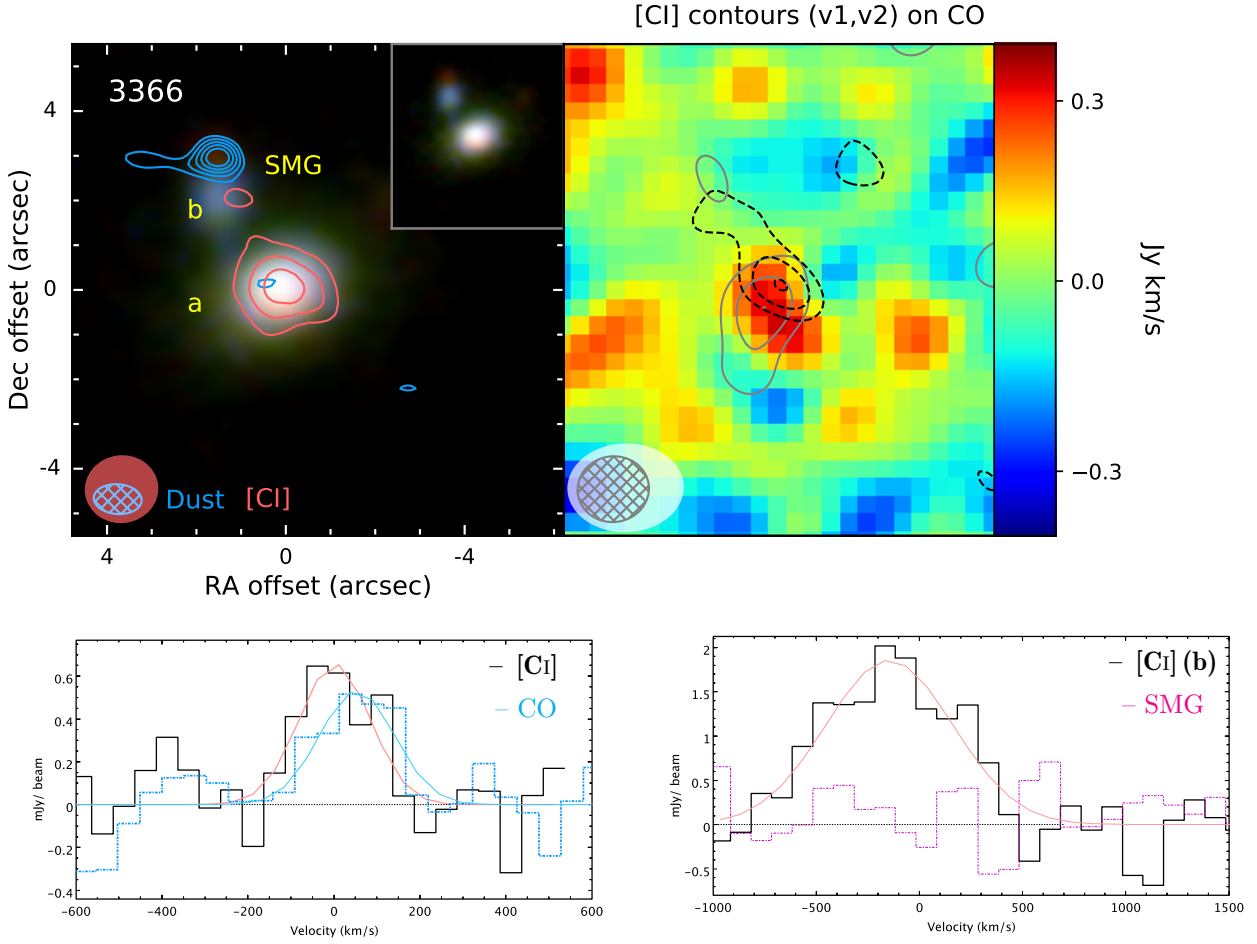


Figure 8. **Left:** *Hrg* image with contours of dust (blue) and [C I] (red) at $[3, 4, 5, 6, 7\sigma]$. The bright continuum source to the NE of the target is an SMG coincident with an optically red source, clearly visible in the upper inset image. The target 3366.a and its satellite, 3366.b, have weak continuum emission ($2-3\sigma$ – not all shown with these contours). The [C I] contours on 3366.a are the full velocity range over which [C I] was detected (v_1 and v_2) tapered with a $1.5''$ Gaussian, as shown by the beam in the lower left. The [C I] contour for 3366.b is at full resolution (i.e. the same as the beam for the continuum). **Right:** Moment-0 map of CO, which has a very weak detection (3σ) for 3366.a with a velocity profile matching that of the component v_1 in [C I]. There is no sign of any CO emission at the blue-shifted velocities associated with the companion. The contours are those of the two velocity components of [C I], tapered with a $1.5''$ Gaussian. Grey solid: the systemic component v_1 , black dashed: the blue-shifted component v_2 , which overlaps with the broad profile seen at the position of the companion galaxy 3366.b. Contours are at $[2, 3, 4\sigma]$. **Lower left:** Spectral profile for CO and [C I] in SDP.3366.a showing emission close to the systemic velocity (3366.a(v_1)). **Lower right:** [C I] profile for the companion source (3366.b) showing the much wider line which extends to the blue-shifted velocities from 3366.a(v_2). Also shown is the spectrum extracted at the SMG position, the lack of signal further indicating its nature as a background source at a different redshift. Only the v_1 component is considered in the analysis of gas calibration, though adding in the v_2 component would not change any of our conclusions.

is only $\sim 5''$ (25 kpc), where we are quoting the quantity $0.5 \times \lambda / \sqrt{u_m^2 + v_m^2}$.⁸ The optical diameter of the galaxies ranges from $4-7''$ (20–35 kpc at this redshift), and we did not expect the molecular gas to be distributed smoothly on scales this large. However this may not be so for the CI-bright H_2 distribution as CO-poor gas will be preferentially be at larger galactocentric distances because of metallicity gradients and/or lower gas densities allowing FUV radiation and/or cosmic rays to shift the $[C^0/CO]$ relative

abundance towards higher values in outer regions. Moreover cold dust is typically found well-beyond optical disks and even well-concomitant with HI (Alton et al. 1998; Thomas et al. 2002a; Smith et al. 2016; Casasola et al. 2017). A subsequent ACA proposal to image those sources with the most extended emission was approved in the Cycle 7 supplementary call, however, only one source had data taken before ALMA ceased operations in March 2020. This source (SDP.3132) shows a small (10 percent) increase in [C I] flux once the ACA data are included, but a much larger (60 percent) increase in the dust flux, from $S_{12m} = 0.95 \pm 0.29$

⁸ At the time of the Cycle 1 call, the proposal guide gave an MRS of $25''$ and $7.1''$ respectively for the two bands. This, plus the severe restriction on observing time for Cycle 1 meant that we did not request ACA data in the first instance.

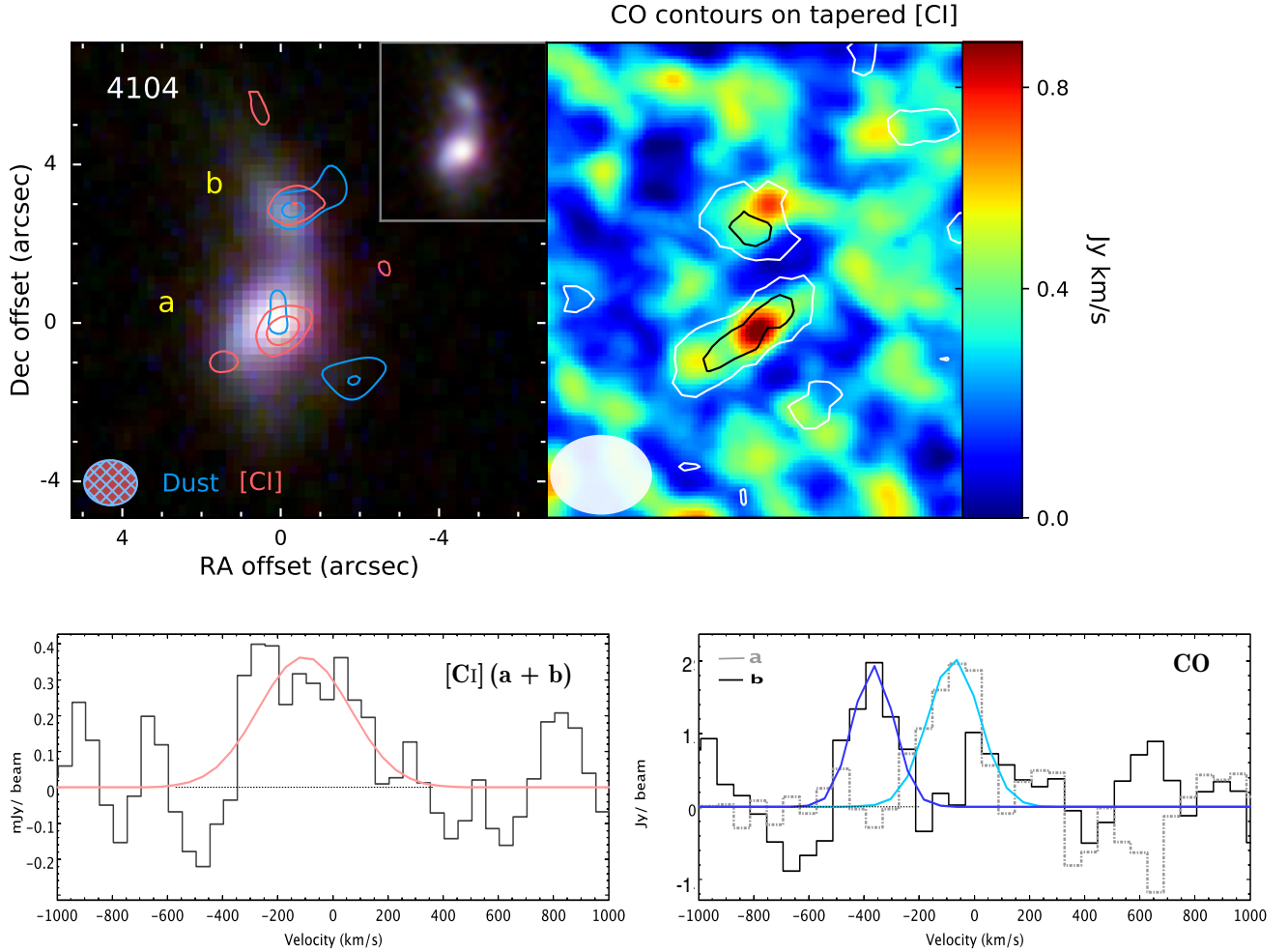


Figure 9. **Left:** *Zrge* image with contours of dust (blue) and [C I] (red), tapered with a 1'' Gaussian. **Right:** Moment-0 image of tapered [C I] with CO contours. All contours at $[2, 3\sigma]$. **Lower left:** [C I] line profile for both galaxies summed together. **Lower right:** CO line profile for each source individually. See notes in Appendix A for details on the difficulties with measurement of [C I] in this source.

to $S_{12m+ACA} = 1.51 \pm 0.39$.⁹ This is not unexpected as the fainter dust continuum is affected more by the filtering effect of the missing short spacings, because there is no frequency dependence in the emission morphology. Other sources which appear to have diffuse dust emission (predominantly the disks which are face-on, SDP.2173, SDP.6216, SDP.6418) may also have substantial fractions of the dust flux resolved out, although there is no indication of anything larger than the effect on SDP.3132 given that none of these sources are outliers in the [C I]–dust or CO–dust relations.

Ultimately, only higher sensitivity (u,v)-matched imaging of CO(1-0), dust continuum and [C I] line emission can resolve these issues, an observing setup that is not trivial, especially between CO(1-0) and [C I] (1-0) lines, given their very different frequencies. Still, should significant tracer brightness be resolved out by our current imaging setup, this will certainly impact any extended [C I] line and dust continuum distribution much more than that of CO(1-0) because of

the differential (u,v) coverage between the low and high frequency observations filtering-out extended emission from the high-frequency tracers (see Figure 3).

Within the limitations of the data (both in terms of resolution, (u, v) coverage, and signal-to-noise), we can say that three of the sources show evidence for some difference between the dust and [C I] distributions. SDP.5323 has a very compact dust morphology centered on the nucleus while the [C I] is found in two lobes outside of the dust core. The CO appears to be more similar to the dust than to the [C I] but the poorer angular resolution and SNR of the CO imaging means we cannot be confident. SDP.6216 has centrally concentrated [C I] emission while the continuum morphology is diffuse and complex. SDP.6418 has dust emission at low level near to the optical centre while the [C I] is located in several clumps at different velocities. The [C I] is distributed over a much wider area than the dust, although the SNR is very low for the dust and so differences here could just be due to there being a diffuse distribution and low SNR.

In summary, there are some very interesting morphological differences between the [C I] and dust, however, the SNR is not high enough for us to be confident that these are real

⁹ While the fractional increase is large, the uncertainties mean that the actual difference is not statistically very significant.

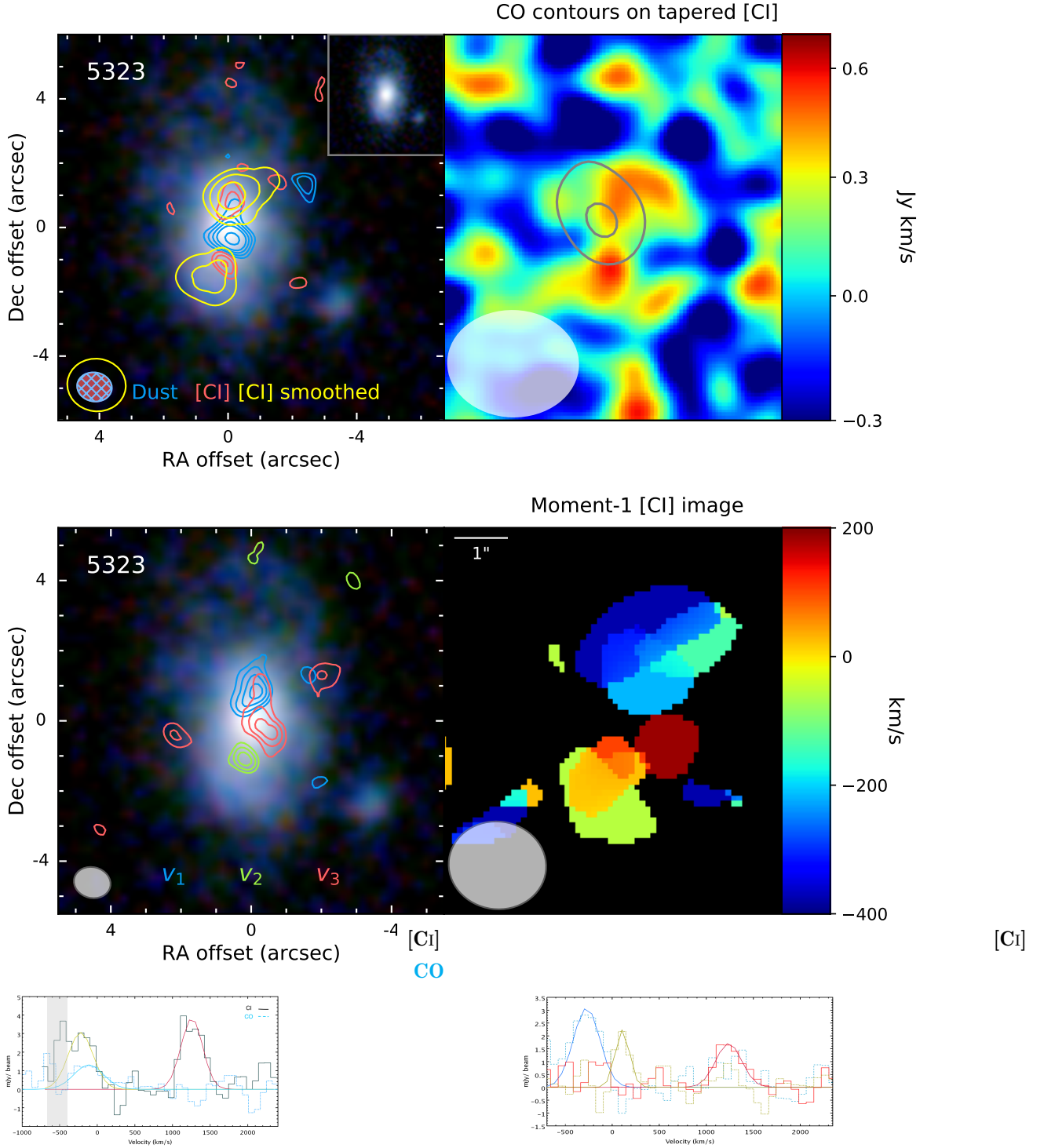


Figure 10. *Top left:* *irg* image with contours of dust (blue) and [C_I] (red: same resolution, yellow: smoothed by 1.5"). *Top right:* CO contours on tapered [C_I] moment-0 map. Only the v_1 and v_2 [C_I] components are shown in this top row. Contours are [2.5, 3.0, 3.5, 4.0] σ for [C_I] and dust and [2, 3] σ for CO. *Middle left:* Velocity components of [C_I], v_1 : $-415 \rightarrow +15$ km s⁻¹, v_2 : $-15 \rightarrow +225$ km s⁻¹ and v_3 : $+945 \rightarrow +1645$ km s⁻¹ (v_3 is the high velocity component which has no CO counterpart and we cannot be sure of its origin). Contours are the same as the top row. *Middle right:* velocity weighted moment map masked at 2σ for the components v_1 and v_2 which we are certain are associated with SDP.5323. *Lower left:* [C_I] and CO line profiles measured from a heavily tapered cube showing all three velocity features. *Lower right:* [C_I] line profiles at the peak of each velocity feature. In the analysis of gas calibration only the v_1 and v_2 [C_I] components are used.

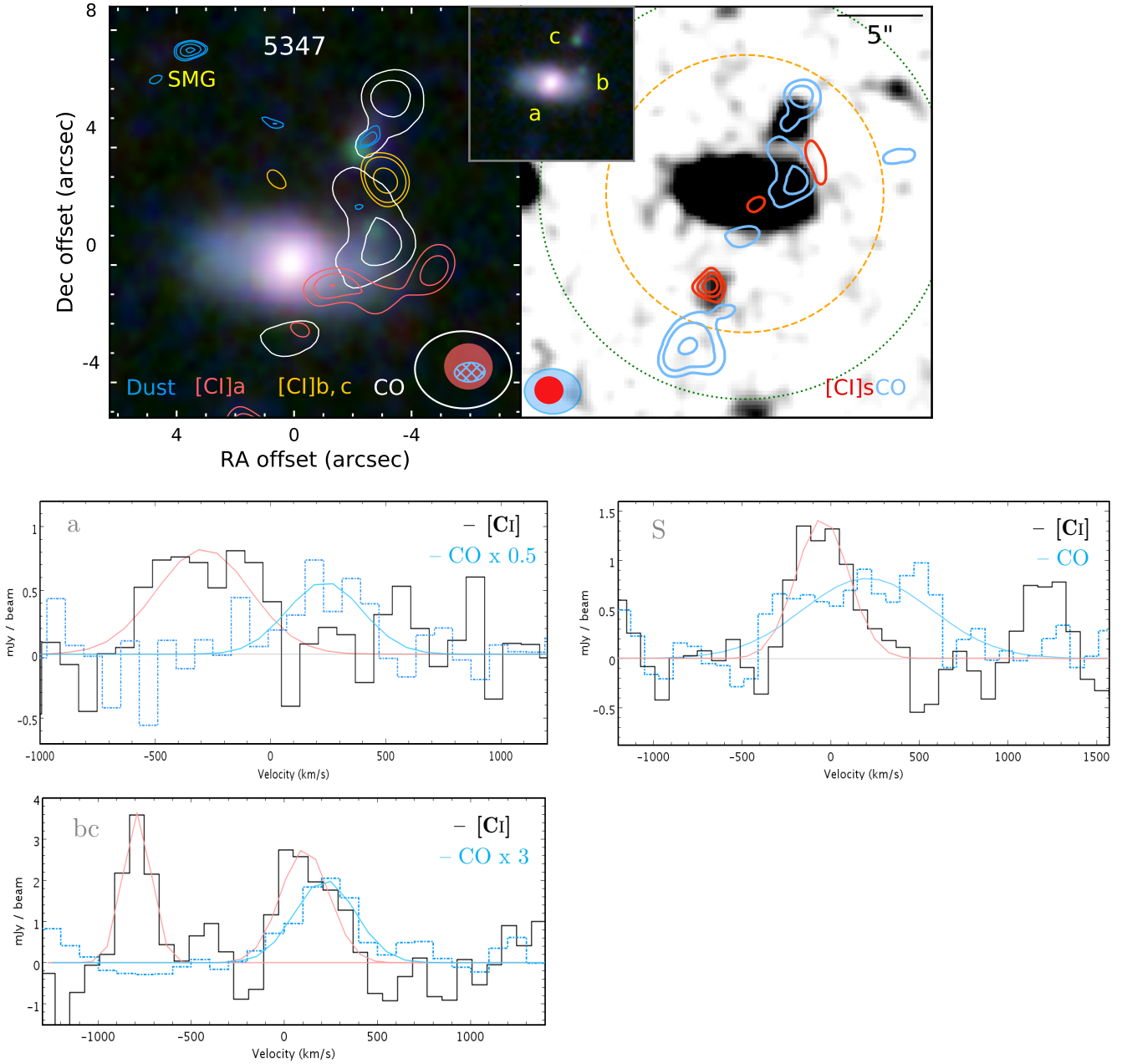


Figure 11. **Top left:** *Krg* image with contours of dust (blue), [C I] (red is the *a* component and orange is *bc*) and CO (white). This is a very complex source (see Appendix. A). [C I] is tapered by $1.5''$, CO by $2''$. CO, dust and [C I] *bc* (orange) contours at $[3.0, 3.5, 4.5\sigma]$, [C I] *a* (red) contours at $[2.0, 2.5, 3.0\sigma]$. **Right:** A highly smoothed KIDs *g*-band image over a wider area showing CO and [C I] emission to the South. The [C I] peak coincides with a low surface brightness patch of blue optical emission. The orange dashed circle denotes the radius at which the primary beam attenuation is a factor of 2, while the green dashed line shows the radius imaged in [C I]. **Center left:** [C I] and CO profiles for the *a* component. Apertures are used in each case to extract the spectra, as the emission is extended and diffuse. There is a significant detection in [C I] but the CO is much weaker and also significantly shifted in velocity. **Lower left:** Spectral profile of the [C I] *bc* component, extracted at the peak of the [C I] emission. The CO emission does not peak at the same location, and we show the CO profile from the full region spanning sources *b* and *c* (scaled by a factor 3 for presentation). The velocity component at $100\text{--}200\text{ km s}^{-1}$ is consistent in both CO and [C I] but there is an additional velocity component at negative velocities which is only seen in [C I]. We list the fluxes for each velocity component separately in Table 4. **Centre right:** Spectral profiles for the Southern emission, shown in the top right panel. The CO and [C I] peaks are not in exactly the same location, however, the [C I] field of view is not large enough to have detected comparable emission at the location of the CO peak, which lies out beyond the HPBW of the primary beam. We show the spectra together to illustrate that there is overlap in their spectral profiles, but the CO profile is much wider than that of the [C I]. We use the [C I] and CO emission from the *a, b, c* components in the analysis on gas calibration.

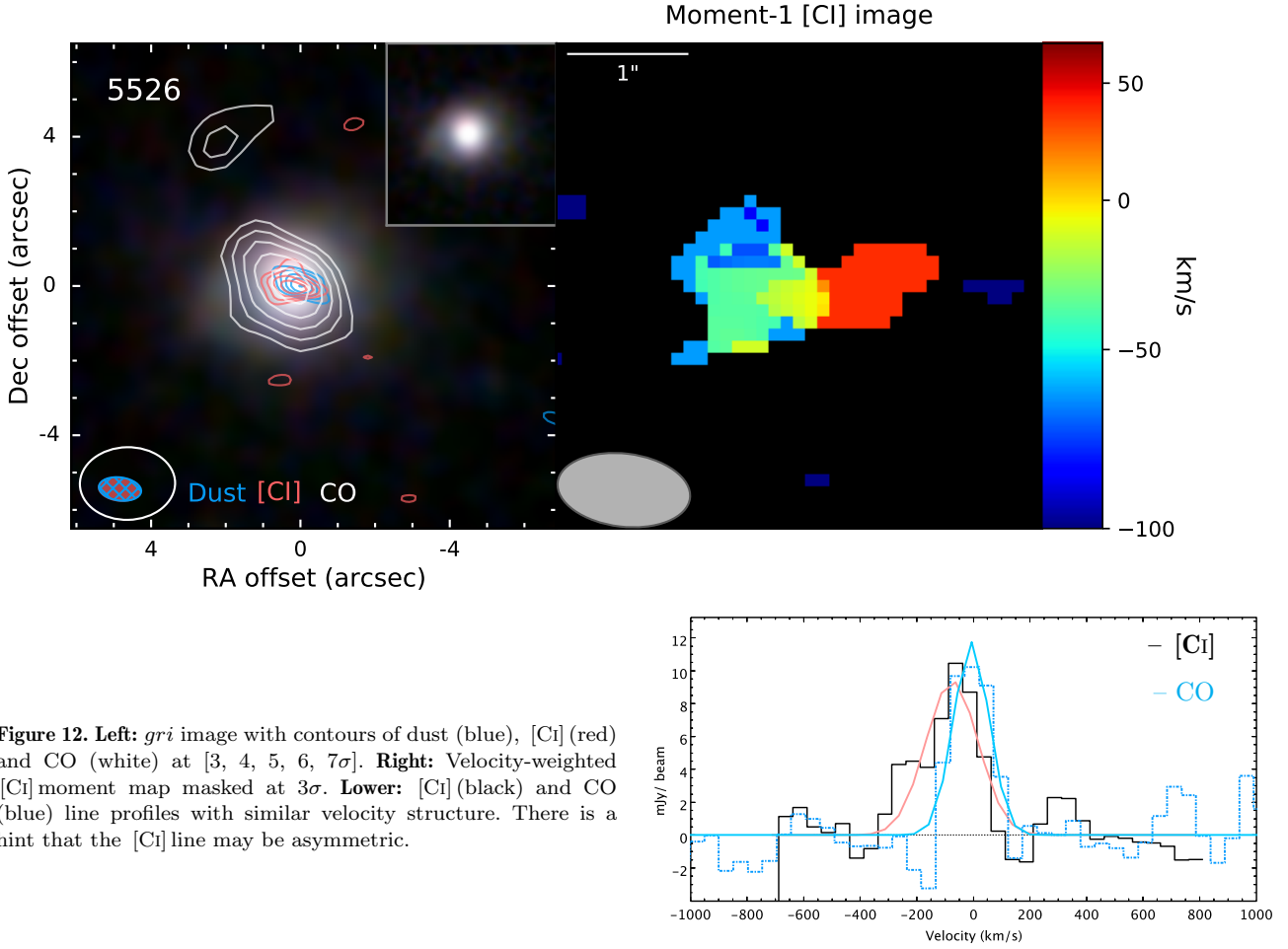


Figure 12. Left: *grz* image with contours of dust (blue), [C_I] (red) and CO (white) at [3, 4, 5, 6, 7σ]. Right: Velocity-weighted [C_I] moment map masked at 3σ. Lower: [C_I] (black) and CO (blue) line profiles with similar velocity structure. There is a hint that the [C_I] line may be asymmetric.

in all cases. The CO(1-0) observations are at a very different angular resolution and do not provide much information on the morphology. To undertake a meaningful morphological comparison of the three tracers requires further observations to (a) improve the sensitivity in all three tracers and (b) crucially match the resolution and the (u, v) coverage between the Band 3 and Band 7 observations.

3.4 Relationships between the tracers

The fluxes which are not in parentheses in Tables 3 and 4 are used to estimate the line luminosities (Solomon & Vanden Bout 2005) and rest-frame 850 μm monochromatic luminosity as follows:

$$L' = \frac{3.25 \times 10^7}{\nu_{\text{rest}}^2} \left(\frac{D_L^2}{1+z} \right) S \Delta v \quad [\text{K km s}^{-1} \text{ pc}^2] \quad (2)$$

Where $S \Delta v$ is the velocity-integrated flux density in Jy km s^{-1} , D_L is the luminosity distance in Mpc and ν_{rest} is the rest frequency of the transition in GHz.

$$L_{850} = 4\pi S_{\nu(\text{obs})} \times K \left(\frac{D_L^2}{1+z} \right) \quad [\text{W Hz}^{-1}] \quad (3)$$

where D_L is the luminosity distance, $S_{\nu(\text{obs})}$ is the observed flux at 353 GHz, and K is the K-correction to rest-frame

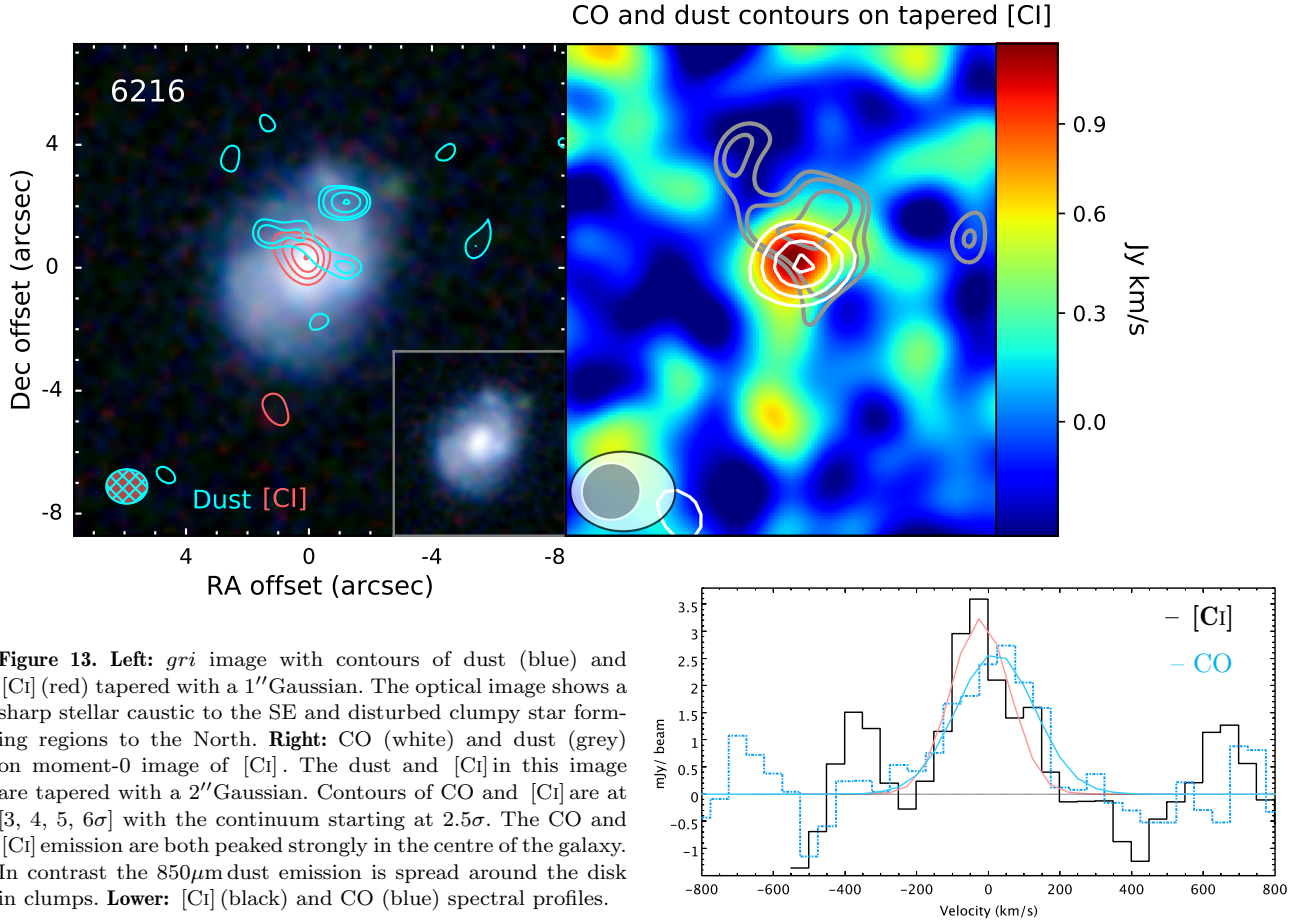
850 μm , defined as

$$K = \left(\frac{353 \text{ GHz}}{\nu_{\text{rest}}} \right)^{3+\beta} \frac{e^{h\nu_{\text{rest}}/kT_d} - 1}{e^{16.956/T_d} - 1} \quad (4)$$

Here $\nu_{\text{rest}} = \nu_{\text{obs}}(1+z)$, T_d is the luminosity weighted dust temperature (from an isothermal fit to the SED) with $\beta = 1.8$. K-corrections for this sample ranged from 2.6–3.0, therefore making this extrapolation to rest frame 850 μm in order to be consistent with the literature (Scoville et al. 2016) does not add significant uncertainty to what we are doing. These luminosities are reported in Table 6.

The correlations between the three observables, $L'_{\text{C I}}$, L'_{CO} and L_{850} are shown in Figure 16, along with the best linear 1:1 fit in order to visually compare the consistency of the various tracers. The two sources which have alternative [C_I] estimates (SDP.4104 and SDP.6418) are shown as cyan and pink circles with the two values joined by a dashed line. The choice of which [C_I] flux to use has no material impact on the conclusions or results. This sample is too small and has too limited a dynamic range in luminosity to make meaningful fits to these relationships, and we defer this process to a much more comprehensive analysis which combines this sample with others from the literature (Dunne et al. *in prep*). Suffice to say that the trend noted here, for [C_I]–dust to have the lowest scatter, is borne out by the analysis on a much larger sample of 70+ sources.

We also show the ratios of the tracers as a function of



sSFR in the right column of Figure 16. The top row shows the L'_{CO}/L_{850} ratio which shows no apparent trend. The middle row shows $R_{\text{CI}} = L'_{\text{CI}}/L'_{\text{CO}}$, with the average values for the Milky Way (Frerking et al. 1989) and high-z QSO (Walter et al. 2011) shown as the grey dot-dashed (lower) and dotted (upper) horizontal lines respectively. With two exceptions (SDP.6418 and SDP.6451), the galaxies fall in a reasonably tight band with a spread of ~ 0.5 dex, and a trend to lower values of R_{CI} with increasing sSFR. The two exceptions have much higher R_{CI} for their sSFR, although the significance of the offset would need to be confirmed with more sensitive CO observations. The bottom row shows L'_{CI}/L_{850} , which has the smallest dispersion. The very highest sSFR galaxies have the lowest L'_{CI}/L_{850} ratios, but given the sample size and error bars there is no significant trend.

The means and medians (in brackets) and 1σ ranges for the ratios are: $\log(L_{850}/L'_{\text{CI}}) = 14.04(14.07) \pm 0.19$, $\log(L_{850}/L'_{\text{CO}}) = 13.39(13.32) \pm 0.25$ and $\log(L'_{\text{CI}}/L'_{\text{CO}}) = -0.66(-0.68) \pm 0.25$. The relationship with the least variance is $L_{850} - L'_{\text{CI}}$ which implies that these two tracers are better correlated with each other than either of them are with CO. We will return to the implications of these relationships for calibrating the H_2 tracers in Section 4.

3.4.1 Potential CO-‘dark’ galaxies

The two sources (SDP.6418 and SDP.6451) which are outliers in the [CI]–CO relationship (Figure 16), have very weak CO emission *despite being detected both in dust and [CI]*. The sources are unremarkable in the [CI]–dust relationship indicating that this seems to be a deficiency in CO relative to the other tracers rather than an enhancement in [CI]. There is nothing particularly special about these sources, their stellar masses are $\log M_* \sim 10.8 M_\odot$, and neither show evidence for an AGN in the optical spectra, using the criteria of Lamareille (2010); they have O[II] flux greater than O[III], and O[III] is generally weak. As pointed out in Section 3.3, any filtering of flux on extended scales is going to affect [CI] more than CO and so this cannot be an explanation for the high [CI]/CO ratio. More data would be needed to confirm this unusual $L'_{\text{CI}}/L'_{\text{CO}}$ ratio, both to increase the sensitivity in the line observations and to match the resolution between the tracers. The ratio of line luminosity $L'_{\text{CI}}/L'_{\text{CO}} (= R_{\text{CI}})$ in these galaxies ranges from $0.54 < R_{\text{CI}} < 0.94$, using the measured CO fluxes which are only 2σ significance. Using a 3σ upper limit on the CO flux gives a lower limit of $R_{\text{CI}} > 0.35$ (0.42) for SDP.6418 and SDP.6451 respectively. The average value in Milky Way clouds is $R_{\text{CI}} \sim 0.15$ (Frerking et al. 1989), while the average value seen in QSO is $R_{\text{CI}} \sim 0.29$ (Walter et al. 2011).

Understanding how reasonably normal star forming galaxies like these can be so deficient in CO is very impor-

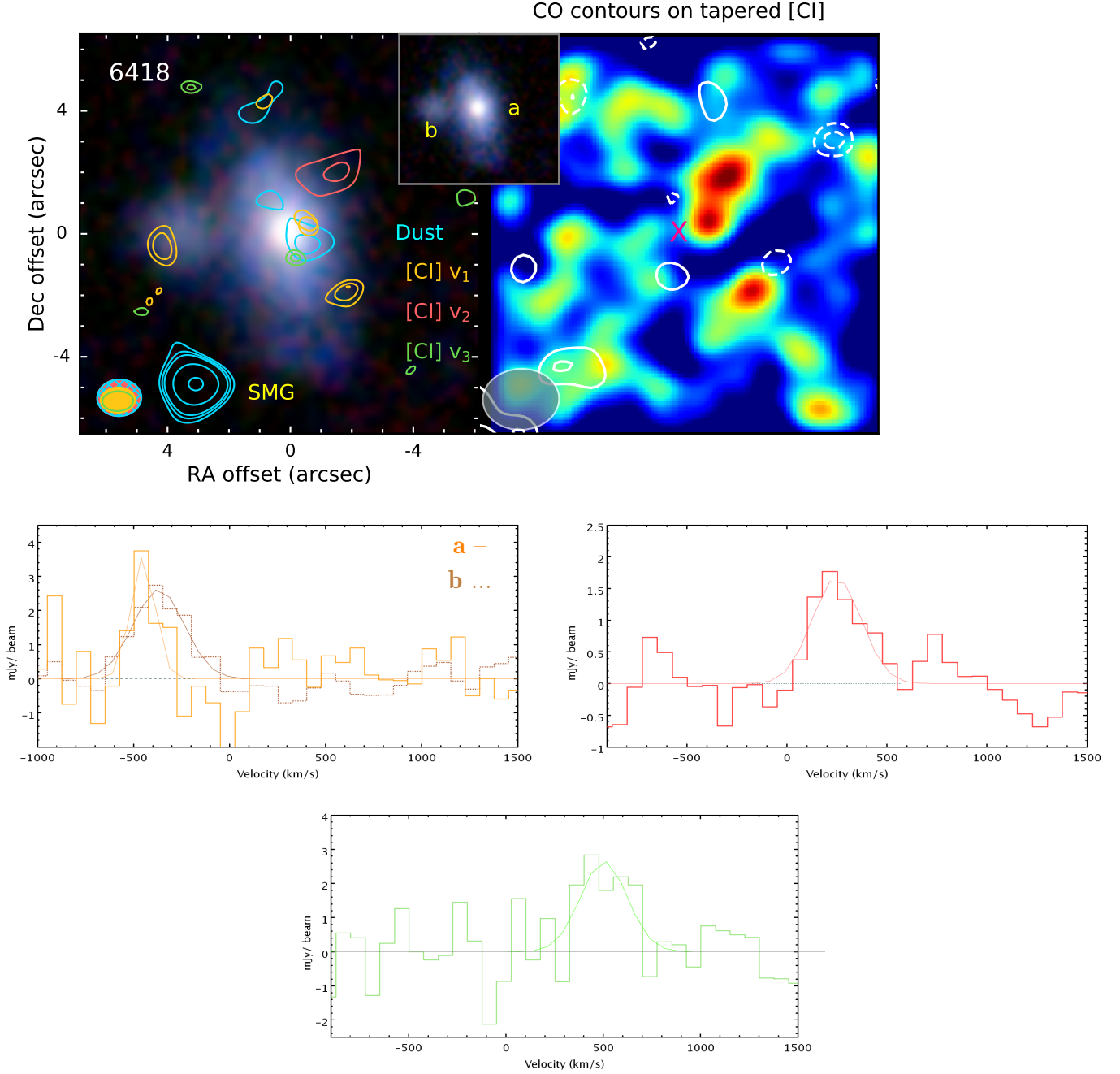


Figure 14. Left: *irg* image with contours of dust smoothed by $2''$ (blue) and [C_I] tapered to $1''$. The colours of the [C_I] contours denote the velocity components. Orange: $v_1 = -450 \text{ km s}^{-1}$, red: $v_2 = +250 \text{ km s}^{-1}$, green: $v_3 = +500 \text{ km s}^{-1}$. Dust and [C_I] contours are at $[3, 4, 5\sigma]$. There is no line emission at the systemic velocity of the optical galaxy. Right: CO contours at $[-2.5, -2.0, 2.0, 2.5\sigma]$ on tapered moment-0 [C_I] image. The pink 'X' marks the centre of the main optical galaxy 'a'. Due to the difficulty of showing the three components together in a moment-0 map, we have created this image by combining the velocity ranges of v_1 and v_2 but including only the positive pixels in the moment-0 image. Thus this image is illustrative of where the [C_I] peaks are in these velocity components but flux cannot be measured from this image. Lower panels: Spectral profiles for the three [C_I] velocity components, colour coded to match the contours. The $v_1 = -450 \text{ km s}^{-1}$ component is also present in the companion optical galaxy 'b', shown as the dotted brown line in the first spectral profile. We use two values for the [C_I] luminosity in the gas calibration analysis, a conservative value just using the v_2 component in the main 6418.a galaxy, and a total value which uses all three components.

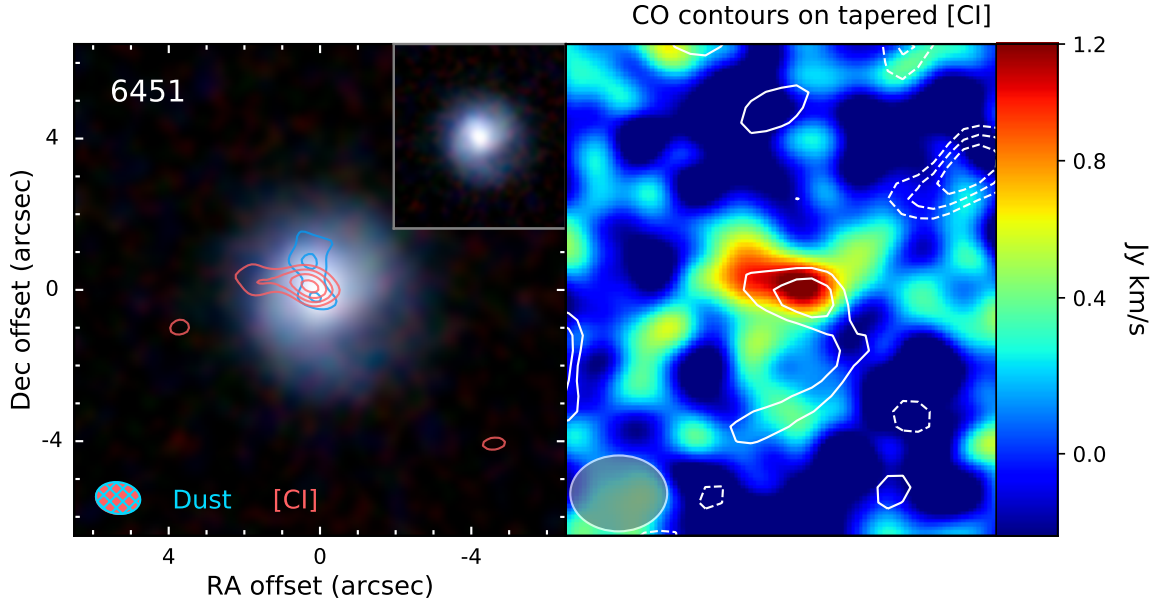
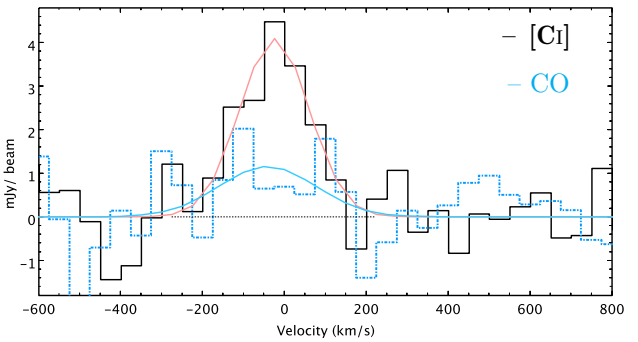


Figure 15. **Left:** *irg* image with contours of dust (blue) and [C I] (red) at [3, 4, 5, 6 σ]. **Right:** Moment-0 map of [C I] smoothed with a 1'' Gaussian and scaled so that the lower level emission is evident ($2\sigma = 0.4 \text{ Jy/km s}^{-1}$). CO contours are shown at intervals of $[-2.5, -2, -1.5, 1.5, 2\sigma]$. While the CO is very low significance, it does match the [C I] reasonably well in position and morphology, even to the extent that both gas tracers appear to delineate a spiral arm to the South. **Lower:** [C I] (black) and CO (blue) line profiles.

tant for understanding the C/CO dependencies in the ISM. One mechanism for reducing CO emission relative to [C I] is cosmic ray destruction of CO molecules volumetrically in the clouds, something discussed at length in Bisbas et al. (2015); Glover & Clark (2016); Bisbas et al. (2017); Papadopoulos et al. (2018). The more recent works show that conditions do not have to be extreme in terms of $\zeta_{\text{CR}} (\propto \rho_{\text{SFR}})$ in order to produce a high $[\text{C}^0/\text{CO}]$ abundance ratio, providing that the average gas density is moderate to low. We note that it is not unheard of to find global H_2 reservoirs dominated by low-density gas, even in vigorous SF environments, and can be the result of coherent SF feedback on the H_2 gas reservoir. This may indeed be so for Arp 193, the most extreme ULIRG in the local Universe after Arp 220, where only small ($\sim 5\%$) gas mass fractions at $n \gtrsim 10^4 \text{ cm}^{-3}$ are inferred from multi-J CO, ^{13}CO , HCN and CS observations (Papadopoulos et al. 2014). We will discuss the line luminosity R_{CI} ratio and how observations compare to theory in more detail with a much larger sample in (Dunne et al. *in prep.*)¹⁰

Finally we note that since: a) C-rich gas may extend fur-



ther out in galactocentric distance than CO-rich gas, and b) differential (u, v) -sampling will filter out extended [C I] line emission more than the much-lower frequency CO(1-0) line, we expect that (u, v) -matched CO, [C I] line imaging of this sample will not only preserve our results about CO-‘dark’ galaxies, but it may even ‘push’ some other galaxies towards a global CO-deficient/[C I]-rich state by revealing more [C I] line emission over larger areas. In that regard, ACA imaging observations, that include total power, of the CO(1-0), [C I] (1-0) and dust continuum, can provide a definitive test.

4 CALIBRATION OF GAS MASS.

We estimate the molecular gas mass of the galaxies in our sample using each of the tracers in turn following the method described in detail in Dunne et al. *in prep.* We differentiate between M_{H_2} - the mass of molecular hydrogen, and M_{mol} - the mass of molecular gas including a factor 1.36 contribution from He. Briefly, to determine M_{H_2} we need a value for the calibration parameter for each tracer: for [C I] we need to know the abundance $X_{\text{CI}} = [\text{C}^0/\text{H}_2]$, for CO we need the α_{CO} factor and for dust we need to know the gas-to-dust ra-

¹⁰ An example of a very low $L'_{\text{CI}}/L'_{\text{CO}}$ ratio in a local LIRG has been recently reported by Michiyama et al. (2020), which further indicates the need to better study a diverse range of galaxies with ALMA in order to understand the effects of the $[\text{C}^0/\text{CO}]$ ratio on global H_2 tracers.

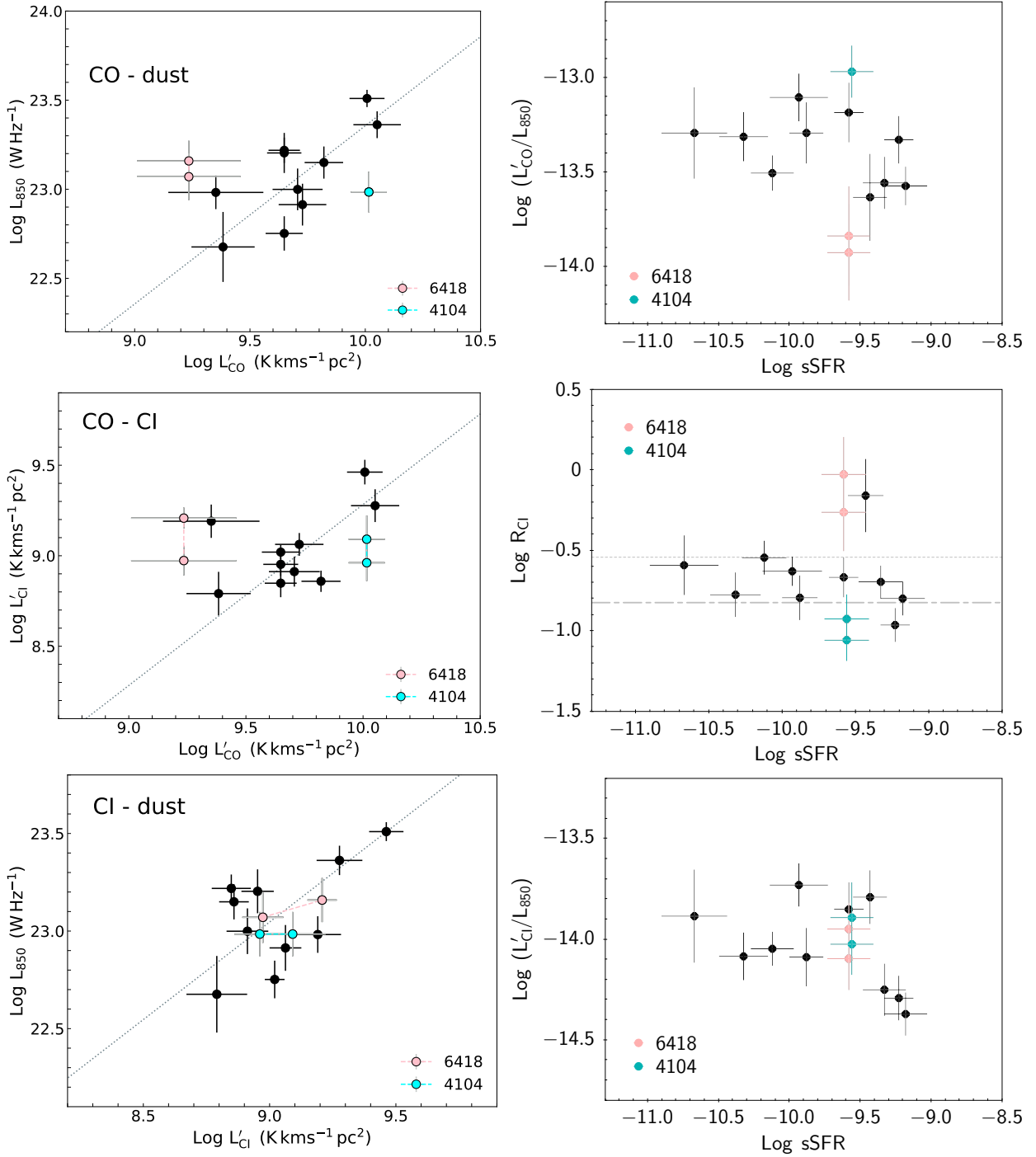


Figure 16. **Left column:** Relationships between the three gas tracers for our sample. The dotted line shows the best linear fit (slope fixed to 1) and. The two sources with alternative [C I] measurements are shown as pink and cyan circles connected by dashed lines. **Right column:** The three tracer ratios as a function of sSFR. The pale dotted and dot-dashed lines in the middle row show the average R_{CI} ratio measured for high redshift QSO (Walter et al. 2011) and the average for Milky Way clouds (Frerking et al. 1989) respectively. Quantities for each source are derived using their measured flux and error, regardless of whether they are ‘detected’ at $> 3\sigma$.

tio δ_{GDR} . The molecular hydrogen gas mass (in M_{\odot} units) then depends on these calibration factors as follows:¹¹

$$M_{H_2}([C I]) = \frac{9.51 \times 10^{-5}}{X_{CI} Q_{10}} L'_{CI}$$

$$M_{H_2}(CO) = \alpha_{CO} L'_{CO}$$

$$M_{H_2}(\text{dust}) = \delta_{GDR} M_d$$

¹¹ Other literature works define quantities such as α_{CI} and α_{850} which are simply related to our calibration factors, and will be presented at the end of this section.

The conversion of L'_{CI} to M_{H_2} also requires an estimate of Q_{10} , which is an excitation function. This is not a strong function of kinetic temperature (see Papadopoulos et al. 2004, Dunne et al. *in prep*) and so we will simply take a single value as is common in the literature. We choose to use the value $Q_{10} = 0.43$ based on the more detailed analysis of a larger sample in Dunne et al. *in prep*. The dust mass is calculated from L_{850} using the mass weighted dust temperature from the MAGPHYS fits and assuming a value for the dust mass opacity at $850\mu\text{m}$ of $\kappa_{850} = 0.065 \text{ m}^2 \text{ kg}^{-1}$ which is consistent with the results from Planck Collaboration XIX (2011) (see Dunne et al. *in prep* for more detailed descriptions of the dust opacity factors).

For each source, we have four unknowns, M_{H_2} , α_{CO} , δ_{GDR} , X_{CI} , and three observables M_{d} , L'_{CO} , L'_{CI} . If we had an independent measure of the true M_{H_2} , then the observed values of L'_{CO} , L'_{CI} and M_{d} would provide direct estimates of the three calibration parameters, α_{CO} , X_{CI} and δ_{GDR} . But, of course, we do not know the value of M_{H_2} , so we need to use a probabilistic argument based on the fact the observations do provide constraints on the relative values of α_{CO} , X_{CI} , and δ_{GDR} for each source.

For each source there is a set of self-consistent calibration factors which link the observed M_{d} , L'_{CO} , L'_{CI} to the true M_{H_2} , with a common, but unknown constant factor. We can write down the products and ratios of these calibration factors in terms of the observed luminosity ratios:

$$\begin{aligned} X_{\text{CI}} \delta_{\text{GDR}} &= 2.212 \times 10^{-4} \frac{L'_{\text{CI}}}{M_{\text{d}}} \\ X_{\text{CI}} \alpha_{\text{CO}} &= 2.212 \times 10^{-4} \frac{L'_{\text{CI}}}{L'_{\text{CO}}} \\ \frac{\alpha_{\text{CO}}}{\delta_{\text{GDR}}} &= \frac{M_{\text{d}}}{L'_{\text{CO}}} \end{aligned} \quad (6)$$

From our parallel study of a larger sample of 72 sources all with CO, [CI] and dust measurements (Dunne et al. *in prep*), we have measured the intrinsic variance for each pair of factors in Eqn. 6. We assume that the covariance between the calibration factors is zero, and use the three pair variances to estimate the intrinsic variance of each individual calibration factor, the population standard deviations of these are denoted σ_X , σ_α and σ_δ for X_{CI} , α_{CO} and δ_{GDR} respectively.

With the constraints given by Eqn 6 we are in a position to determine self-consistent values for each of the calibration factors, α_{CO} , X_{CI} and δ_{GDR} , except for one thing: we do not have any independent measure of the gas mass on which to tie the normalisations of the our calibration (4 unknowns but only 3 measurements). We therefore have to assume a *sample average* for one of the unknown calibration factors, but having done so the relative values of all three will be optimised, and it is trivial to re-scale the solutions to a different normalisation if desired. We choose to normalise to a sample mean $\delta_{\text{GDR}} = 135$ which is the Milky Way value for Hydrogen (no He) from the THEMIS dust framework (Jones 2018).¹²

¹² More precisely the combination of $\delta_{\text{GDR}} / \kappa_{\text{d}}$ we use is 2077,

Dunne et al. *in prep* use their sample of 72 sources which have observations for all three gas tracers¹³ to estimate the mean values of X_{CI} and α_{CO} . This gives us the 3 calibration factors normalised to the Milky Way value of δ_{GDR} . Using these mean values together with the population standard deviations, σ_X , σ_α , σ_δ , we can estimate the probability of finding a particular set of calibration factors for any given source. Using x_i , $i = 1, 2, 3$ to denote the logarithms of the three calibration factors, we can write the means and effective standard deviations as \bar{x}_i , and σ_i respectively, where the effective standard deviation is the intrinsic scatter on each parameter added in quadrature to the measurement error for that gas tracer. Assuming these follow Gaussian distributions, the probability of finding calibration factors x_i for any source is given by

$$\begin{aligned} P &\propto \prod_{i=1}^3 \exp\left(-\frac{(x_i - \bar{x}_i)^2}{2\sigma_i^2}\right) \\ &= \exp\left(-\sum_{i=1}^3 \frac{(x_i - \bar{x}_i)^2}{2\sigma_i^2}\right) \end{aligned} \quad (7)$$

For any given source, we use the observed luminosity ratios in Eqn. 6, to fix the ratios of calibration factors, and choose the common scaling factor that maximises the probability in equation 7. The resulting optimised parameters are listed in Table 7, and shown in Figure 17, while the average values for the sample are listed in Table 8. By design, each tracer for a given source will produce the same gas mass when used in Eqn. 5. The errors are quoted as the values which give $\Delta\chi^2 = 1$. We list these gas masses in Table 7 along with the gas fraction, f_{g} , which is defined as $M_{\text{mol}} / (M_{\text{*}} + M_{\text{mol}})$.¹⁴

5 DISCUSSION

5.1 Calibration factors

We now place the values of our gas calibration factors into context with other recent work and other nomenclature for describing them.

We find that the mean and standard deviation for $X_{\text{CI}} = (1.6 \pm 0.3) \times 10^{-5}$, which is similar to the values found in clouds in the Milky Way (Frerking et al. 1989) and to the recent determination of X_{CI} using GRB/QSO absorber systems using a totally independent method (Heintz & Watson 2020). Several authors have adopted the use of an empirical quantity α_{CI} , with similar units of $\text{M}_{\odot} (\text{K km s}^{-1})^{-1}$

which is the quantity that calibrates dust emission to gas mass. This is equivalent to $\sigma_{850}/m_{\text{H}}$ in S.I. units, where σ_{850} is the dust opacity at $850\mu\text{m}$ per H atom.

¹³ That sample includes the 12 galaxies from this analysis.

¹⁴ If we use the median calibration factors from the sample, listed in Table 8, to derive gas masses from each tracer independently (as one would do if only one measurement were available) there can be some dispersion in the three gas mass estimates depending on how far away a particular source lies in the distribution from the median. For most sources, the mass difference between any pair of tracers is within ± 0.2 dex, except for the two sources with high α_{CO} (SDP.6418 and SDP.6451).

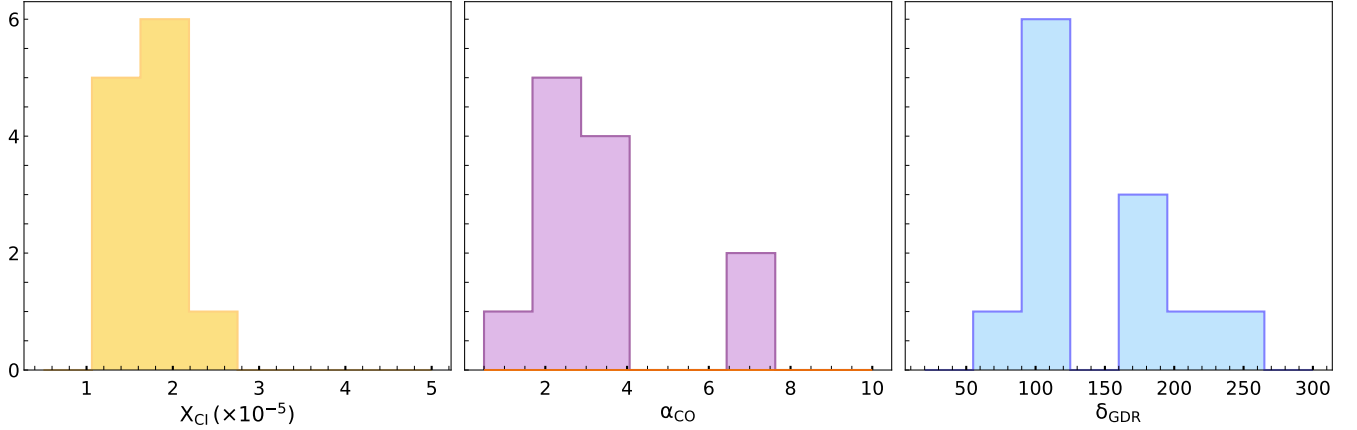


Figure 17. Distribution of the calibration parameter values which are listed in Table 7.

Table 7. Calibration and gas mass parameters. M_{H_2} , X_{CI} , α_{CO} and δ_{GDR} do not include a contribution from He. α_{CI} and α_{850} along with f_g do include a factor 1.36 for He.

Source	Log M_{H_2} [M_\odot]	X_{CI} [$\times 10^{-5}$]	α_{CI} [M_\odot (K kms $^{-1}$ pc 2) $^{-1}$]	α_{CO} [M_\odot (K kms $^{-1}$ pc 2) $^{-1}$]	δ_{GDR}	α_{850} [W Hz $^{-1}$ M_\odot $^{-1}$]	f_g	τ_{dep} [Gyr]
163	10.58 ± 0.11	1.7 ± 0.4	17.9	3.8 ± 0.9	111 ± 28	6.2×10^{12}	0.15	2.4
1160	10.06 ± 0.10	2.0 ± 0.5	14.9	2.6 ± 0.6	261 ± 61	3.6×10^{12}	0.13	1.1
2173	10.14 ± 0.11	1.8 ± 0.5	16.4	2.6 ± 0.6	181 ± 47	4.3×10^{12}	0.19	0.9
3132	10.11 ± 0.11	1.5 ± 0.4	19.9	2.9 ± 0.8	94 ± 24	9.0×10^{12}	0.24	0.7
3366	9.85 ± 0.15	1.9 ± 0.7	15.7	3.0 ± 1.0	177 ± 62	4.9×10^{12}	0.06	2.8
4104	10.16 ± 0.13	1.4 ± 0.4	21.4	1.4 ± 0.4	186 ± 55	4.9×10^{12}	0.19	0.9
4104 ^c	10.22 ± 0.14	1.6 ± 0.5	18.4	1.6 ± 0.5	217 ± 69	4.2×10^{12}	0.21	1.0
5323	10.09 ± 0.12	1.5 ± 0.4	20.4	2.4 ± 0.7	110 ± 31	6.0×10^{12}	0.13	1.1
5347	10.48 ± 0.12	1.3 ± 0.4	21.5	2.7 ± 0.7	103 ± 29	5.7×10^{12}	0.22	5.7
5526	10.09 ± 0.11	1.3 ± 0.3	23.3	1.9 ± 0.5	92 ± 23	8.4×10^{12}	0.14	1.7
6216	10.13 ± 0.11	1.2 ± 0.3	26.0	3.0 ± 0.8	64 ± 17	9.0×10^{12}	0.32	0.7
6418	10.07 ± 0.13	1.8 ± 0.5	17.1	6.9 ± 2.1	100 ± 30	7.3×10^{12}	0.20	1.0
6418 ^t	10.26 ± 0.12	2.0 ± 0.5	15.3	10.6 ± 2.9	125 ± 34	5.8×10^{12}	0.28	1.5
6451	10.17 ± 0.13	2.3 ± 0.7	13.0	6.6 ± 2.0	168 ± 50	4.8×10^{12}	0.26	0.9

Gas mass in M_\odot using the optimised calibration method described in Section 4. The optimised calibration parameter for each gas tracer, X_{CI} , α_{CO} and δ_{GDR} . Gas fraction f_g defined as $M_{mol}/(M_* + M_{mol})$, using the value of M_* from the MAGPHYS fitting in Table 6. Gas depletion timescale, M_{mol}/SFR , in Gyr. SDP.4104^c uses the [C I] fluxes corrected for flagged channels within the line profile as described in Appendix A. SDP.6418^t uses all three of the [C I] velocity components, as opposed to just the v_2 component.

to that of α_{CO} , which is used as standard in extragalactic studies. α_{CI} is related to carbon abundance, X_{CI} as follows, where we now include a factor of 1.36 for He:

$$\alpha_{CI} = 1.293 \times 10^{-4} (X_{CI} Q_{10})^{-1}$$

Thus for our average $X_{CI} = 1.6 \times 10^{-5}$ and $Q_{10} = 0.43$, we find that $\alpha_{CI} = 18.8 M_\odot$ (K kms $^{-1}$ pc 2) $^{-1}$.

The only other source which has an estimate of α_{CI} independent of a blind assumption on the value of α_{CO} is the AGN influenced CND region of NGC 7469, for which Izumi et al. (2020) find a value of $\alpha_{CI} = 4.4 M_\odot$ (K kms $^{-1}$ pc 2) $^{-1}$, which is equivalent to $X_{CI} = 7 \times 10^{-5}$. They attribute their much higher value of X_{CI} to the effects of an X-ray dominated region (XDR) on the ISM, which increases the $[C^0]/H_2$ ratio. High values for X_{CI} have also been inferred for other extreme sources in the high redshift universe such as QSO (Walter et al. 2011), however in these cases an assumption is made that $\alpha_{CO} \sim 0.8$ in such sources, which then produces a higher X_{CI} compared to what would be inferred using a standard $\alpha_{CO} \sim 4$. The

Izumi et al. work is novel because the calibration factors are estimated using a dynamical mass estimate for H_2 from very well sampled ALMA data. A comprehensive comparison of calibration factors with those in the literature is undertaken in Dunne et al. *in prep*.

We find an average $\alpha_{CO} = 3.0^{+1.4}_{-0.7} M_\odot$ (K kms $^{-1}$ pc 2) $^{-1}$, not including He,¹⁵ which is typical of star forming galaxies with an ISM dominated by self-gravitating clouds (Papadopoulos et al. 2012a; Bolatto et al. 2013; Sandstrom et al. 2013).

While we began with a prior that the gas-to-dust ratio δ_{GDR} would be similar to that in the Milky Way (given these are massive, metal rich star-forming galaxies), our method allows the δ_{GDR} to vary slightly in order to maximise the likelihood when considered along with the other two gas tracers. With this we find an average $\delta_{GDR} = 129 \pm 57$ with a range of δ_{GDR} for individual sources ranging from 60–260,

¹⁵ To compare to other work which does include He and heavier elements, our α_{CO} values should be multiplied by 1.36.

Table 8. Average calibration factors derived from this sample. Note that these calibration factors do not include the correction for He.

Parameter	mean	σ_m	median
$X_{\text{CI}} (\times 10^{-5})$	$1.6^{+0.3}_{-0.2}$	0.1	1.6
	$1.7^{+0.3}_{-0.3}$	0.1	1.7
α_{CO}	$3.0^{+1.4}_{-0.7}$	0.5	2.8
	$3.1^{+1.3}_{-0.8}$	0.7	2.8
δ_{GDR}	128^{+54}_{-35}	16	111
	132^{+57}_{-39}	16	118

The sample averages for the calibration parameters, using the optimisation procedure described in Section 4. The first line represents the values using the conservative [CI] estimates for 6418 and 4104. The second row includes all the velocity components for 6418 and corrects the [CI] flux for 4104 for the missing channels as described in the text. The errors quoted on the mean are the 16th and 84th percentiles representing the $\pm 1\sigma$ scatter. σ_m is the formal error on the mean (i.e. $1/\sqrt{12}$ times the scatter).

as expected for such a sample. Once again this δ_{GDR} does not include the contribution from He. It is now common to refer to the calibration between dust luminosity and gas mass as α_{850} , following the work of [Scoville et al. \(2014, 2016\)](#). This is defined as $\alpha_{850} = L_{850} / M_{\text{mol}}$ with units of $\text{W Hz}^{-1} M_{\odot}^{-1}$, where now He is included in the definition of M_{mol} . We describe this parameter and its measurements in the literature in great detail in [Dunne et al. in prep.](#), but here just note that it is related to δ_{GDR} (assuming our $\kappa_d = 0.065$ and including a factor 1.36 for He) as:

$$\alpha_{850} = 7.78 \times 10^{14} (24.5 / T_{\text{mw}})^{-1.4} \delta_{\text{GDR}}^{-1}$$

where T_{mw} is the mass-weighted dust temperature, commonly assumed by [Scoville et al. \(2016\)](#) and others to be ~ 25 K in the sources they studied (typically high redshift star forming galaxies). Our empirically derived α_{850} , using the optimal gas mass calculated using the above method, is $\alpha_{850} = (5.9 \pm 1.8) \times 10^{12} \text{ W Hz}^{-1} M_{\odot}^{-1}$. For our average $\delta_{\text{GDR}} = 129$ and a $T_{\text{mw}} = 25\text{K}$ (which agrees well with the results of our MAGPHYS SED fits), we find a comparable value of $\alpha_{850} = 6.0 \times 10^{12} \text{ W Hz}^{-1} M_{\odot}^{-1}$. This compares with the value initially suggested by ([Scoville et al. 2016](#)) of 10.1×10^{12} and more recent literature studies which indicate $\alpha_{850} = 3.8 - 8.8 \times 10^{12}$ ([Orellana et al. 2017](#); [Hughes et al. 2017](#); [Kaasinen et al. 2019](#)).

Overall, this sample of $250\mu\text{m}$ selected galaxies at $z = 0.35$ have M_{H_2} calibration factors for CO(1–0), [CI](1–0) and dust which are comparable to normal spiral star forming galaxies in the local Universe, and conditions in the Milky Way.

5.2 Gas fractions and evolutionary status.

The mean gas fraction for the sample is 0.19 ± 0.07 where the error is the 1σ standard deviation. This narrow range is rather surprising as $250\mu\text{m}$ selection from H-ATLAS at $z = 0$ produces samples with a huge range of gas fraction (0.1–0.9), and a mean value of $f_g \sim 0.5$ ([Clark et al. 2015](#)). This $z = 0$ selection was volume limited and dust mass selected, and was therefore dominated by lower mass, blue and H I rich

galaxies. In contrast, Figure 1 suggests that by $z = 0.35$ H-ATLAS is only sensitive to the most massive dust sources, which presumably restricts the range of gas fractions, assuming that the anti-correlation between gas fraction and stellar mass holds also at $z = 0.35$ ([De Vis et al. 2017](#); [Saintonge et al. 2017](#)). At a given stellar mass, the gas fractions we find at $z = 0.35$ are significantly higher than those found in the local Universe by the xCOLD GASS survey ([Saintonge et al. 2017](#)), who find $f_g = 0.02 - 0.04$ for galaxies in our stellar mass range. However, in terms of specific star formation rate, the scaling found by xCOLD GASS seems to hold at $z = 0.35$, where for $\text{sSFR} = -10.5$ the expectation is $f_g = 0.039$, while at $\log \text{sSFR}/\text{yr}^{-1} = -9.5$ this increases to $f_g = 0.15$. Thus the increased sSFR 3.9 Gyr in the past is completely consistent with the extra gas available without any changes to the efficiency of how it is converted into stars. This is noteworthy since the observables providing the measures of gas fraction (CO, [CI] and dust) and sSFR (UV–optical SED) are completely independent in this study.

It is common in the literature for authors to define a gas depletion timescale (also the inverse of the star formation efficiency) as $\tau_{\text{dep}} = M_{\text{mol}} / \text{SFR}$, which is a crude way of measuring the relative speed at which the current molecular reservoir is being converted into stars. We list this value for our sources in Table 7. There are limitations to this idea, principally that neither M_{mol} nor SFR are fixed quantities, M_{mol} being only a snapshot of the molecular mass at the observed epoch, and SFR being only the current SFR (averaged over ~ 100 Myr). The SFR will decline as the gas is consumed (thus τ_{dep} is a lower limit to any physical depletion timescale), while in addition more gas may be accreted at later times, from either the cosmic web, mergers or simply the infall of atomic gas from the outer regions of the disk. The median of this quantity $\tau_{\text{dep}} = 1.1^{+1.3}_{-0.2}$ Gyr where the error is the 16–84th percentile range. This is consistent with the range of τ_{dep} in the most massive gas-rich galaxies today, which is 1–1.6 Gyr over the same mass range as our sample ([Saintonge et al. 2017](#)). The time elapsed from $z = 0.35$ to $z = 0$ is 3.9 Gyr, which means that all of these galaxies would be passive today if they continued to form stars at the same rate without fresh gas supply. Certainly there must be some transformation from dust and gas rich galaxies at $z=0.35$ to passive galaxies today ([Dunne et al. 2011](#); [Beeston et al. 2018](#)), but it is not plausible that all of them will become passive further high-lighting the limitations of the simple τ_{dep} parameter.

6 CONCLUSIONS

We present ALMA observations of sub-mm dust continuum at $850\mu\text{m}$, $^{12}\text{CO}(1-0)$ and [CI]($^3\text{P}_1-^3\text{P}_0$) for a complete and volume limited sample of 12 sources selected at $250\mu\text{m}$ from the H-ATLAS survey. We detected dust and either CO or [CI] in all of the targets, finding:

- While the galaxies in the sample are reasonably ‘normal’ in terms of their L_{IR} and sSFR at these redshifts, a very high proportion (40 percent) of the sample are found to be interacting or kinematically disturbed systems. The interactions are mostly minor mergers, and hence maybe it is

not surprising that they do not induce major star formation events.

- There is a large variety of morphology in the gas and dust, and in some cases the [C I] and dust do not appear to have the same spatial structure. The CO resolution is too poor to allow a spatial comparison but kinematically there are also differences between [C I] and CO in the most disturbed systems.

- The range of $L'_{\text{CI}}/L'_{\text{CO}}$ in these sources is very large, covering the full range observed in local clouds in the Milky Way up to those seen in high- z QSO. We find two potential CO-‘dark’ candidates, detected in [C I] and dust but not in CO.

- We estimate the gas calibration parameters, X_{CI} , α_{CO} and δ_{GDR} for each source using a likelihood approach. The sample averages are: Carbon abundance (required to calibrate [C I] as a gas tracer) $X_{\text{CI}} = 1.6^{+1.3}_{-0.2} \times 10^{-5}$, while $\alpha_{\text{CO}} = 3.0^{+1.4}_{-0.7} \text{ M}_{\odot} (\text{K km s}^{-1} \text{ pc}^2)^{-1}$ and $\delta_{\text{GDR}} = 128^{+54}_{-35}$, where we quote the sample log means and 16-84th percentile ranges. These factors do not include a correction for He. The starting assumption is that the average δ_{GDR} is similar to that for the Milky Way in these metal-rich massive galaxies. In other commonly used calibration units, which do account for He, these translate to $\alpha_{\text{CI}} = 18.8 \text{ M}_{\odot} (\text{K km s}^{-1} \text{ pc}^2)^{-1}$ and $\alpha_{850} = 5.9 \times 10^{12} \text{ W Hz}^{-1} \text{ M}_{\odot}^{-1}$.

- The gas fractions in these galaxies range from 0.06–0.32, with an average of $f_{\text{g}} = 0.19$ and a scatter of 0.07. This is a very small range of gas fraction, which is surprising given the very diverse galaxies in a volume limited $250\mu\text{m}$ selected sample at $z = 0$.

We conclude this work by noting the supreme importance of (u,v)-matched imaging in all three prime H_2 gas mass tracers explored here, in order to fully and accurately reveal the similarities and differences of their distributions in galaxies. ALMA+ACA+(total power) imaging could provide the key for such comparisons in the future, by allowing the most unbiased imaging for the high-frequency [C I] lines and sub-mm dust continuum.

DATA AVAILABILITY

The data underlying this article are publicly available from the ALMA archive <http://almascience.eso.org/aq/> using the project code 2012.1.00973.S.

ACKNOWLEDGEMENTS

The authors thank the anonymous referee for their time in helping to improve the manuscript. LD thanks P. Papadopoulos for superb cooking, enlightening conversations and a careful proof-read and improvement of the draft manuscript. LD and SJM acknowledge support from the European Research Council Advanced Investigator grant, COSMICISM and Consolidator grant, COSMIC DUST. HLG acknowledges support from the European Research Council Consolidator grant, COSMIC DUST. This paper makes use of the following ALMA data: ADS/JAO.ALMA#2012.1.00973.S. ALMA is a partnership of ESO (representing its member states), NSF (USA) and NINS (Japan), together with NRC (Canada), MOST and

ASIAA (Taiwan), and KASI (Republic of Korea), in co-operation with the Republic of Chile. The Joint ALMA Observatory is operated by ESO, AUI/NRAO and NAOJ. The National Radio Astronomy Observatory is a facility of the National Science Foundation operated under co-operative agreement by Associated Universities, Inc. The Herschel-ATLAS is a project with Herschel, which is an ESA space observatory with science instruments provided by European-led Principal Investigator consortia and with important participation from NASA. The H-ATLAS website is <http://www.h-atlas.org>. GAMA is a joint European-Australasian project based around a spectroscopic campaign using the Anglo-Australian Telescope. The GAMA input catalogue is based on data taken from the Sloan Digital Sky Survey and the UKIRT Infrared Deep Sky Survey. Complementary imaging of the GAMA regions is being obtained by a number of independent survey programs including GALEX MIS, VST KIDS, VISTA VIKING, WISE, *Herschel*-ATLAS, GMRT and ASKAP providing UV to radio coverage. GAMA is funded by the STFC (UK), the ARC (Australia), the AAO, and the participating institutions. The GAMA website is: <http://www.gama-survey.org/>. This publication has made use of data from the VIKING survey from VISTA at the ESO Paranal Observatory, programme ID 179.A-2004. Data processing has been contributed by the VISTA Data Flow System at CASU, Cambridge and WFAU, Edinburgh.

REFERENCES

- Alaghband-Zadeh S., et al., 2013, *MNRAS*, **435**, 1493
 Alton P. B., et al., 1998, *A&A*, **335**, 807
 Baldry I. K., et al., 2018, *MNRAS*, **474**, 3875
 Beeston R. A., et al., 2018, *MNRAS*, **479**, 1077
 Bisbas T. G., Papadopoulos P. P., Viti S., 2015, *ApJ*, **803**, 37
 Bisbas T. G., van Dishoeck E. F., Papadopoulos P. P., Szűcs L., Bialy S., Zhang Z.-Y., 2017, *ApJ*, **839**, 90
 Boland W., de Jong T., 1982, *ApJ*, **261**, 110
 Bolatto A. D., Wolfire M., Leroy A. K., 2013, *ARA&A*, **51**, 207
 Bothwell M. S., Maiolino R., Peng Y., Ciccone C., Griffith H., Wagg J., 2016, *MNRAS*, **455**, 1156
 Bothwell M. S., et al., 2017, *MNRAS*, **466**, 2825
 Bourne N., et al., 2016, *MNRAS*, **462**, 1714
 Bourne N., Dunlop J. S., Simpson J. M., Rowlands K. E., Geach J. E., McLeod D. J., 2019, *MNRAS*, **482**, 3135
 Casasola V., et al., 2017, *A&A*, **605**, A18
 Casuoli S., et al., 2015, *MNRAS*, **452**, 3100
 Chapman S. C., Blain A. W., Smail I., Ivison R. J., 2005, *ApJ*, **622**, 772
 Clark C. J. R., et al., 2015, *MNRAS*, **452**, 397
 Clark C. J. R., et al., 2019, *MNRAS*, **489**, 5256
 Combes F., García-Burillo S., Braine J., Schinnerer E., Walter F., Colina L., 2011, *A&A*, **528**, A124
 Condon J. J., 1997, *PASP*, **109**, 166
 Crocker A. F., et al., 2019, *ApJ*, **887**, 105
 De Vis P., et al., 2017, *MNRAS*, **464**, 4680
 Downes D., Solomon P. M., 1998, *ApJ*, **507**, 615
 Driver S. P., et al., 2011, *MNRAS*, **413**, 971
 Driver S. P., et al., 2016, *MNRAS*, **455**, 3911
 Dunne L., Eales S. A., 2001, *MNRAS*, **327**, 697
 Dunne L., Eales S., Edmunds M., Ivison R., Alexander P., Clements D. L., 2000, *MNRAS*, **315**, 115
 Dunne L., et al., 2011, *MNRAS*, **417**, 1510
 Dunne L., Bonavera L., Gonzalez-Nuevo J., Maddox S. J., Vlahakis C., 2020, *MNRAS*, **498**, 4635

- Dye S., et al., 2010, *A&A*, **518**, L10
- Eales S., et al., 2010, *PASP*, **122**, 499
- Eales S., et al., 2018, *MNRAS*, **473**, 3507
- Edge A., Sutherland W., Kuijken K., Driver S., McMahon R., Eales S., Emerson J. P., 2013, *The Messenger*, **154**, 32
- Frerking M. A., Keene J., Blake G. A., Phillips T. G., 1989, *ApJ*, **344**, 311
- Glover S. C. O., Clark P. C., 2016, *MNRAS*, **456**, 3596
- Griffin M. J., et al., 2010, *A&A*, **518**, L3
- Heintz K. E., Watson D., 2020, *ApJ*, **889**, L7
- Helou G., Khan I. R., Malek L., Boehmer L., 1988, *ApJS*, **68**, 151
- Hopkins A. M., et al., 2013, *MNRAS*, **430**, 2047
- Hughes T. M., et al., 2017, *MNRAS*, **468**, L103
- Israel F. P., 2020, *A&A*, **635**, A131
- Israel F. P., Baas F., 2002, *A&A*, **383**, 82
- Israel F. P., Tilanus R. P. J., Baas F., 2006, *A&A*, **445**, 907
- Ivison R. J., Papadopoulos P. P., Smail I., Greve T. R., Thomson A. P., Xilouris E. M., Chapman S. C., 2011, *MNRAS*, **412**, 1913
- Izumi T., et al., 2020, arXiv e-prints, [p. arXiv:2006.09406](https://arxiv.org/abs/2006.09406)
- Janssen D. J., 1995, PhD thesis, Leiden Observatory, Leiden University, P.O. Box 9513, 2300 RA Leiden, The Netherlands
- Jiao Q., Zhao Y., Zhu M., Lu N., Gao Y., Zhang Z.-Y., 2017, *ApJ*, **840**, L18
- Jiao Q., et al., 2019, *ApJ*, **880**, 133
- Jones A. P., 2018, arXiv e-prints,
- Kaasinen M., et al., 2019, *ApJ*, **880**, 15
- Kamenetzky J., Rangwala N., Glenn J., Maloney P. R., Conley A., 2014, *ApJ*, **795**, 174
- Keene J., Blake G. A., Phillips T. G., Huggins P. J., Beichman C. A., 1985, *ApJ*, **299**, 967
- Keene J., Lis D. C., Phillips T. G., Schilke P., 1997, in van Dishoeck E. F., ed., *IAU Symposium Vol. 178*, IAU Symposium, pp 129–139
- Kelvin L. S., et al., 2012, *MNRAS*, **421**, 1007
- Krips M., et al., 2016, *A&A*, **592**, L3
- Lamareille F., 2010, *A&A*, **509**, A53
- Langer W., 1976, *ApJ*, **206**, 699
- Lara-López M. A., Bongiovanni A., Cepa J., Pérez García A. M., Sánchez-Portal M., Castañeda H. O., Fernández Lorenzo M., Pović M., 2010, *Astronomy and Astrophysics*, **519**, A31
- Liske J., et al., 2015, *MNRAS*, **452**, 2087
- Liszt H. S., 2011, *A&A*, **527**, A45
- Liszt H., Gerin M., Grenier I., 2018, *A&A*, **617**, A54
- Lu N., et al., 2017, *ApJS*, **230**, 1
- Maddox S. J., Dunne L., 2020, *MNRAS*,
- Magdis G. E., et al., 2012, *ApJ*, **760**, 6
- McMullin J. P., Waters B., Schiebel D., Young W., Golap K., 2007, in Shaw R. A., Hill F., Bell D. J., eds, *Astronomical Society of the Pacific Conference Series Vol. 376*, *Astronomical Data Analysis Software and Systems XVI*. p. 127
- Michiyama T., et al., 2020, *ApJ*, **897**, L19
- Orellana G., et al., 2017, *A&A*, **602**, A68
- Oteo I., Zwaan M. A., Ivison R. J., Smail I., Biggs A. D., 2016, *ApJ*, **822**, 36
- Papadopoulos P. P., Greve T. R., 2004, *ApJ*, **615**, L29
- Papadopoulos P. P., Thi W.-F., Viti S., 2002, *ApJ*, **579**, 270
- Papadopoulos P. P., Thi W.-F., Viti S., 2004, *MNRAS*, **351**, 147
- Papadopoulos P. P., van der Werf P. P., Xilouris E. M., Isaak K. G., Gao Y., Mühle S., 2012a, *MNRAS*, **426**, 2601
- Papadopoulos P. P., van der Werf P., Xilouris E., Isaak K. G., Gao Y., 2012b, *ApJ*, **751**, 10
- Papadopoulos P. P., et al., 2014, *ApJ*, **788**, 153
- Papadopoulos P. P., Bisbas T. G., Zhang Z.-Y., 2018, *MNRAS*, **478**, 1716
- Pelupessy F. I., Papadopoulos P. P., 2009, *The Astrophysical Journal*, **707**, 954
- Pérez-Beaupuits J. P., Stutzki J., Ossenkopf V., Spaans M., Güsten R., Wiesemeyer H., 2015, *A&A*, **575**, A9
- Pilbratt G. L., et al., 2010, *A&A*, **518**, L1
- Pineda J. L., Langer W. D., Velusamy T., Goldsmith P. F., 2013, *A&A*, **554**, A103
- Planck Collaboration XIX 2011, *A&A*, **536**, A19
- Planck Collaboration et al., 2011, *Astronomy and Astrophysics*, **536**, A19
- Planck Collaboration et al., 2016, *A&A*, **594**, A13
- Poglitsch A., et al., 2010, *A&A*, **518**, L2
- Prasad S. S., Tarafdar S. P., 1983, *ApJ*, **267**, 603
- Remy Q., Grenier I. A., Marshall D. J., Casandjian J. M., 2017, *A&A*, **601**, A78
- Rigby E. E., et al., 2011, *MNRAS*, **415**, 2336
- Robotham A. S. G., Driver S. P., 2011, *MNRAS*, **413**, 2570
- Rowlands K., et al., 2014, *MNRAS*, **441**, 1017
- Saintonge A., et al., 2017, *ApJS*, **233**, 22
- Sandstrom K. M., et al., 2013, *ApJ*, **777**, 5
- Sargent M. T., Béthermin M., Daddi E., Elbaz D., 2012, *ApJ*, **747**, L31
- Scoville N., et al., 2014, *ApJ*, **783**, 84
- Scoville N., et al., 2016, *ApJ*, **820**, 83
- Simpson J. M., et al., 2015, *ApJ*, **807**, 128
- Smith D. J. B., et al., 2011, *MNRAS*, **416**, 857
- Smith M. W. L., et al., 2016, *MNRAS*, **462**, 331
- Solomon P. M., Vanden Bout P. A., 2005, *ARA&A*, **43**, 677
- Solomon P. M., Downes D., Radford S. J. E., Barrett J. W., 1997, *ApJ*, **478**, 144
- Speagle J. S., Steinhardt C. L., Capak P. L., Silverman J. D., 2014, *The Astrophysical Journal Supplement Series*, **214**, 15
- Stach S. M., et al., 2019, *MNRAS*, **487**, 4648
- Suzuki H., Yamamoto S., Ohishi M., Kaifu N., Ishikawa S.-I., Hirahara Y., Takano S., 1992, *ApJ*, **392**, 551
- Tacconi L. J., et al., 2006, *ApJ*, **640**, 228
- Tacconi L. J., et al., 2008, *ApJ*, **680**, 246
- Tanaka K., Oka T., Matsumura S., Nagai M., Kamegai K., 2011, *ApJ*, **743**, L39
- Thomas H. C., Dunne L., Clemens M. S., Alexander P., Eales S., Green D. A., 2002a, *MNRAS*, **329**, 747
- Thomas H. C., Dunne L., Clemens M. S., Alexander P., Eales S., Green D. A., James A., 2002b, *Monthly Notices of the Royal Astronomical Society*, **331**, 853
- Tielens A. G. G. M., Hollenbach D., 1985, *ApJ*, **291**, 722
- Torrey P., et al., 2019, *Monthly Notices of the Royal Astronomical Society*, **484**, 5587
- Vale Asari N., Stasińska G., Cid Fernandes R., Gomes J. M., Schlickmann M., Mateus A., Schoenell W., 2009, *Monthly Notices of the Royal Astronomical Society*, **396**, L71
- Valentino F., et al., 2018, *ApJ*, **869**, 27
- Valentino F., et al., 2020, *ApJ*, **890**, 24
- Valiante E., et al., 2016, *MNRAS*, **462**, 3146
- Walter F., Weiß A., Downes D., Decarli R., Henkel C., 2011, *ApJ*, **730**, 18
- Weiß A., Downes D., Henkel C., Walter F., 2005, *A&A*, **429**, L25
- Williams D. A., Hartquist T. W., 1984, *MNRAS*, **210**, 141
- Wilson D., et al., 2017, *ApJ*, **848**, 30
- Wolfire M. G., Hollenbach D., McKee C. F., 2010, *ApJ*, **716**, 1191
- Wright A. H., et al., 2016, *MNRAS*, **460**, 765
- Wright A. H., et al., 2018, arXiv e-prints, [p. arXiv:1812.06077](https://arxiv.org/abs/1812.06077)
- Zhang Z.-Y., et al., 2014, *A&A*, **568**, A122
- Zhang Z.-Y., Papadopoulos P. P., Ivison R. J., Galametz M., Smith M. W. L., Xilouris E. M., 2016, *Royal Society Open Science*, **3**, 160025
- Zhu M., Gao Y., Seaquist E. R., Dunne L., 2007, *AJ*, **134**, 118
- da Cunha E., Charlot S., Elbaz D., 2008, *MNRAS*, **388**, 1595
- da Cunha E., et al., 2013, *ApJ*, **766**, 13
- da Cunha E., et al., 2015, *ApJ*, **806**, 110
- de Jong J. T. A., et al., 2017, *A&A*, **604**, A134

This paper has been typeset from a \LaTeX file prepared by the author.

APPENDIX A: NOTES ON INDIVIDUAL SOURCES

SDP.163 (SK)

This is the most massive galaxy with $M_* = 2.3 \times 10^{11} M_\odot$, and $f_g = 0.13$, residing in a GAMA group (ID104290) with estimated dynamical mass of $4.3 \times 10^{13} M_\odot$ (Robotham & Driver 2011). The GAMA spectrum (Fig. C1) has good SNR, and strong O[II] and O[III]. It is classed as a Sy 2 using the Lamareille (2010) blue classification. The source, which is strongly detected in CO, [C_I] and dust continuum, is a highly inclined massive disk galaxy with FWHM = $700 - 800 \text{ km s}^{-1}$ in both CO and [C_I]. Continuum subtraction was performed in the u, v -plane for the B7 cube. There is an extra kinematic component in the [C_I] cube at the northern end of the galaxy which is not present in the CO map, but which is significant in the [C_I] cube with $S_{\text{CI}} = 1.7 \pm 0.5 \text{ Jy km s}^{-1}$. The flux reported in Table 4 includes this component. This suggests that the CO/C_I ratio is not constant across the galaxy. Matched resolution imaging is needed to further study the spatial variation in the [C_I]/CO ratio.

SDP.1160 (SK)

This galaxy has $M_* = 1 \times 10^{11} M_\odot$ and $f_g = 0.07$. It is the brightest member of a GAMA group (ID103864) with a second galaxy at the same velocity a distance of 0.076 Mpc/h away. The GAMA spectrum (Fig. C1) shows O[II] in emission on a reddened continuum. This source has bright and compact [C_I] and dust emission (Fig. 5).

SDP.2173 (SK)

This is a face-on spiral galaxy with $M_* = 7.9 \times 10^{10} M_\odot$ and $f_g = 0.14$. The optical spectrum (Fig. C2) shows broad lines of O[III] lines and narrow O[II] and H β emission, the continuum is quite blue and there is weak dust attenuation. This is the brightest galaxy in the r -band, with an absolute magnitude of $R = -21.7$, and while not a member of a GAMA group, it has three dwarf companions with compatible photo- z ($z_{\text{ph}} = 0.37 - 0.38$) at projected distances of 40–90 kpc. The dust, [C_I] and CO emission are spatially extended, with a narrow profile consistent with the face-on orientation (Fig. 6).

SDP.3132 (SK)

This is a face-on spiral galaxy with $M_* = 5.4 \times 10^{10} M_\odot$ and $f_g = 0.21$. The GAMA spectrum (Fig. C2) is noisy with emission lines of O[II] and H β . The dust, [C_I] and CO emission are extended. The inclusion of ACA data taken in Cycle 7 shows that as much as 60 percent of the continuum flux of this source was resolved out in the original 12-m configuration. The [C_I] emission was not so affected, with a 10 percent increase once the ACA data were included. The CO and [C_I] lines are very narrow with consistent profiles.

SDP.3366 (DK)

This galaxy is massive with $M_* = 1.3 \times 10^{11} M_\odot$ and $f_g = 0.04$. The GAMA spectrum (Fig. C3) shows strong and broad lines of O[III] and strong O[II]. H δ and H β are strong in absorption, Ca H is stronger than Ca K and there is no strong 4000Å break, indicating a recent significant star formation event. The line ratios put it

in the Sy 2 region of the Lamareille (2010) blue diagram, however, with such strong absorption underlying the H β line this will be a very uncertain classification. The Sersic fits from GAMA (Kelvin et al. 2012) are steeper in the K-band ($n_K = 4.6 \pm 0.2$) compared to the Z-band ($n_Z = 2.6 \pm 0.1$), suggesting that the bluer emission is coming from a rejuvenated disk while the older stellar population is consistent with a spheroid. There is a small, blue neighbouring source in the optical imaging which has photometric redshift $z_{\text{ph}} = 0.26 - 0.38$ from the KIDS survey (Cavuoti et al. 2015; Wright et al. 2018). This is denoted as 3366.b in Table 4 and Fig. 8.

The dust and gas morphology and kinematics are complex. Firstly, Fig. 8 shows strong 850 μm continuum emission from a SMG coincident with a very red source ($K_{\text{AB}} = 19.0$) located 3.4'' to the north-east of the $z = 0.35$ galaxy. There is no line emission associated with this continuum (see spectral profile in Fig 8).

Both the bluer satellite galaxy and the massive central target galaxy show weak dust emission. The 850 μm flux for the satellite was fitted at the same time as fitting a point source to the position of the SMG using the 2-D Gaussian fit task IMFIT. There is also broad [C_I] emission spatially coincident with the blue satellite galaxy (3366.b), shown as the black spectral profile in the lower right panel of Fig 8. There is no CO counterpart to the satellite visible in the depth of our 3-mm data.

The massive central galaxy has [C_I] emission in two velocity components: 3366.a(v1) at the optical redshift and a blue-shifted component, 3366.a(v2), which overlaps in velocity with the broad [C_I] emission from the small blue satellite galaxy (3366.b). These two components are shown in the upper right panel of Fig 8. This suggests an interaction between the two sources, probably responsible for the recent star formation activity in an otherwise older stellar population, as indicated by the optical spectrum and Sersic fits. The spectral profiles for the velocity component centered on the optical redshift, 3366.a(v1), are shown in the lower left panel of Fig 8 with CO in blue and [C_I] in black, showing reasonable agreement between the CO and [C_I] kinematics for this component. CO is only detected at the v1 velocity, the blue-shifted [C_I] emission associated with the main target, 3366.a(v2), and that of the satellite galaxy (3366.b) have no corresponding CO emission.

To compute the [C_I], CO and dust luminosities used in the comparison of the tracers and gas masses (Section 4) we use the values for the 3366.a(v1) component only.

SDP.4104 (DK)

The H-ATLAS target is the southern source (4104.a) of a galaxy pair, with $M_* = 7.8 \times 10^{10} M_\odot$ and $f_g = 0.13$. The GAMA optical spectrum (Fig. C3) has a noisy continuum with detection of O[II], and very weak O[III]. The neighbouring optical source to the north (4104.b) has $z_{\text{ph}} = 0.37$ from KIDS (Cavuoti et al. 2015) but was below the r -band limit for inclusion in the GAMA spectroscopic sample. There is a relatively narrow CO line feature close to the optical velocity of the target ($\Delta V_{\text{CO}} = -72 \text{ km s}^{-1}$) which appears to be elongated along the major axis of the galaxy (see lower right inset panel in Fig. 9). A second, blue-shifted CO component is detected at the position of the northern companion, with a velocity offset of -360 km s^{-1} , confirming that the two galaxies are interacting. The dust continuum image also shows emission at the location of both sources, albeit at very low SNR in the main target (which is extended). The [C_I] data for this target are affected by an atmospheric absorption line in the middle of the expected velocity profile, which was flagged before making the spectral cubes. This resulted in two 50 km s^{-1} channels being unusable due to the large noise from mostly flagged data. The moment 0 maps were made excluding these affected channels

($-50 \rightarrow +50 \text{ km s}^{-1}$) resulting in a lower limit to the integrated line flux (listed in the first row of Table 4). Notwithstanding this, both galaxies are detected in [CII] with positions and velocities consistent with the CO data. The elongation seen in the CO emission along the major axis of the southern galaxy is also seen in [CII].

In an attempt to correct for the missing flux, we have added a second measurement in Table 4 denoted ^c which includes a contribution from the two missing channels assuming that their flux is the average of the neighbouring good channels on either side. For the northern source (4104.b) with a velocity offset of $\Delta V_{CO} = -360 \text{ km s}^{-1}$, this is a negligible addition but for the main optical target (4104.a), the extra flux estimated this way is 50% of the measurement with the missing channels. We use both sets of fluxes (corrected and uncorrected) in the comparison of gas mass tracers in Section 4 summing together 4104.a and 4104.b (since both will be contributing equally to the H-ATLAS photometry). There is only a modest change in the parameters when the correction is made, and so the decision to correct or not is not critical to the conclusions in the paper.

SDP.5323 (DK)

This galaxy has $M_* = 1.1 \times 10^{11} M_\odot$ and $f_g = 0.11$. The GAMA spectrum (Fig. C4) has strong O[II] emission and weak but broad O[III]. The Balmer series is visible in absorption with CaH being stronger than CaK and there is some residual H β emission in the absorption trough, indicating a recent episode of star formation (A-star signatures). The low level optical emission is suggestive of a disturbed disk in the young stellar population and there is a small satellite of similar optical colour to the south west which has a 9-band photo-z of $z_{ph} = 0.27$ (Wright et al. 2018). Figure 10 (top left) shows a very complex morphology. Continuum dust emission is detected along the major axis of the galaxy with a peak located just south of the nucleus, while the [CII] appears in two peaks either side of the dust. The line emission is clearly resolved and so tapering was employed to improve the visibility of low level extended flux (yellow contours in Fig. 10 (top left) are [CII] smoothed by $1.5''$). The top right panel shows CO contours on a tapered [CII] moment-0 map, and it can be seen that the CO appears to be more similar to the dust in its position and morphology but matched resolution observations are required to investigate further the correspondence between the CO and [CII] and dust.

This source also has a complex velocity field, with a velocity offset between the northern and southern [CII] peaks as shown in Fig. 10 (centre right). The green and blue contours denote the two velocity components: $v1 = -273 \text{ km s}^{-1}$ (blue) and $v2 = +107 \text{ km s}^{-1}$ (green). The centre right panel shows the velocity weighted moment map masked at 2σ for these main two components which we are certain are associated with SDP.5323. The two velocity peaks are quite clearly distinguished although the SNR is not high enough to say if this is consistent with rotation. A third [CII] component at much higher velocity ($v3 = +1239 \text{ km s}^{-1}$) is shown as red contours in Fig. 10 (centre left) with an extended and complex morphology. This gas may be associated with tidal disruption experienced by the galaxy. The total flux for the main galaxy components ($v1$ and $v2$) was measured by making two moment 0 maps in the velocity ranges shown by the blue and green contours in Fig. 10, measuring the fluxes on each and then summing them. These are the measurements which are used in the analysis of the gas mass and calibration. The CO shows no complex morphology or kinematics and has a velocity profile similar to the combined $v1$ and $v2$ components in [CII], as shown in Fig. 10 (lower left). The MAGPHYS SED fit (Fig. C4) is not well constrained for dust properties because there was no PACS coverage for this source.

SDP.5347 (DK)

This galaxy has $M_* = 1.3 \times 10^{11} M_\odot$ and $f_g = 0.17$. The GAMA spectrum (Fig. C4) shows a strong 4000Å break and Balmer, CaH and K and Mg absorption features, but no emission lines are seen.¹⁶ The Krg image (Fig. 11 top left) shows the massive central galaxy ‘5347.a’ and two small sources to the west and north (‘b’ and ‘c’) which have bluer optical colours. The small source to the west is not de-blended by KIDs and the one to the north has $z_{ph} = 0.62$ (Cavuoti et al. 2015; Wright et al. 2018), however there is a colour gradient across this source, which may make the fluxes used for the photo-z inaccurate.

The CO moment-0 map is integrated over the velocity range ($-200 \rightarrow +500 \text{ km s}^{-1}$) and shows an extended structure stretching N-S between the two small optical galaxies and the disk of the target.

There is dust emission at the position of the northern optical companion (5347.c), and also a background SMG (see Dunne et al. submitted) to the North-East of the system. The dust emission elsewhere is very weak.

Tapering the continuum subtracted [CII] cube reveals a structure between the two small satellites to the west at similar velocity to the CO emission in the same region (Fig. 11 top left orange contours: component ‘b,c’, and lower left). There is an additional component at large blue-shifted velocity (-750 km s^{-1}) which has no counterpart in CO. This blue-shifted emission peaks at exactly the same location as the main velocity component between the optical satellites b and c, and also has a second clump just north of the main optical galaxy. There is a second [CII] component associated with the main galaxy reaching out in the direction of b, this is shown as red contours in Fig. 11 (top left) with the spectral profile shown in the centre left panel. There is no CO component at the same velocity.

Based on the CO and [CII] morphology and kinematics, we assume this is an interacting system, though there is no optical verification for this. There is very little gas or dust associated with the centre of SDP.5347.a, which is not so surprising given the rather passive nature of the optical spectrum.

There is also a clump of CO emission further South which is shown in Fig. 11 (top right), which may also be related to tidal disruption (e.g. Thomas et al. 2002b; Zhu et al. 2007). It has a very broad velocity range (Fig. 11: centre right). The band 7 field of view is much smaller and so this CO clump falls beyond the half-power radius for the primary beam (shown as an orange dashed circle in the top right panel) which means we would not have the sensitivity to detect any counterpart in [CII]. A [CII] clump is however detected significantly slightly north of the CO clump but at overlapping velocity ranges. The [CII] clump is coincident with a faint blue patch of emission in the g-band image (smoothed in Fig. 11 top right). The southern clumps are listed as SDP.5347(S) in Tables 3 and 4 but are not used further in any analysis.

h

SDP.5526

This isolated galaxy has $M_* = 6.6 \times 10^{10} M_\odot$ and $f_g = 0.2$. The optical GAMA spectrum (Fig. C5) shows strong O[II] and also H β in emission. At the very red end of the spectrum the N[II] and H α lines can be seen, though the spectrum is very noisy in this region. This source is well detected in CO, CII and dust continuum, with a narrow line-width and the signature of rotation in the velocity weighted moment map (Fig. 12). The dust and gas are centrally concentrated, however there is lower level continuum

¹⁶ H α does appear right at the edge of the spectrum but there is often a problem with the throughput calibration in this region so we do not have confidence in this as the only line.

emission which contributes significantly to the integrated flux in the tapered image. The WISE 22 μ m flux for this source seems very high relative to the permissible SEDs from MAGPHYS in Figure C5.

SDP.6216

An isolated, blue and vigorously star forming galaxy with $M_* = 3.8 \times 10^{10} M_\odot$ and $f_g = 0.33$. The optical GAMA spectrum (Fig. C5) shows strong lines of O[II] and H β and weaker O[III]. In conjunction with the strong Balmer absorption lines, this indicates a recent burst of star-formation, which is now declining. The MAGPHYS SED fit is shown in Fig. C5 and is in agreement with the optical spectrum, favouring a high sSFR with low dust extinction. The optical *gri* image (Fig. 13) shows a sharp stellar caustic to the south-east and disturbed clumpy star forming regions to the North. This asymmetry suggests a possible recent interaction either with another galaxy (now subsumed), accretion from the cosmic web or simply disk instability. There are good detections of [C_I] and CO, with a relatively narrow line profile (FWHM $\sim 250 \text{ km s}^{-1}$), as expected for this low inclination galaxy. The morphology of the dust and [C_I] emission is different in this source. The [C_I] is centrally concentrated while the continuum morphology is complex: low level emission is visible across the northern half of the optical disk in the tapered image (grey contours in the right panel of Fig. 13). There is a bright and compact (but not point-like) dust source in the northern spiral arm, where the three colour optical image shows clumpy regions of star formation (upper inset). The dust clump could be interpreted either as an obscured SF region in the disk or a background SMG. The flux of the dust clump is 0.43 mJy. Finally, there is extended clumpy dust emission to the East of the galaxy; it does not coincide with any optical features but may be tracing cold gas associated with the outer disk. Three values for the 850 μ m continuum flux are given in Table 4. The first includes the compact clump and the emission in the disk, the second is a robust minimum flux which subtracts the compact clump and does not include the Eastern extension. The third is a robust maximum which includes all three components. Careful inspection of the optical/NIR images and the morphology of the compact clump leads us to prefer the explanation that it is part of the galaxy disk and so we regard the first flux as the most plausible estimate, and this is the one we use in our analysis of the gas mass in Section 4.

SDP.6418

This appears to be an interacting system with the main galaxy, SDP.6418.a, having $M_* = 6.2 \times 10^{10} M_\odot$ and $f_g = 0.18$. The GAMA spectrum (Fig. C6) shows a blue continuum with very strong O[II] emission, and also significant O[III] and H β with H δ in absorption. There is H α just visible at the red end of the spectrum. The smaller diffuse neighbour of similar colour to the east, has $z_{ph} = 0.42$ (Cavuoti et al. 2015). A reasonably strong 850 μ m continuum source in the primary beam allowed us to self-calibrate this image. The dust continuum in both low redshift galaxies is detected, but is weak and extended. This source is a challenge to interpret as we do not find CO or [C_I] line emission at the systemic velocity of the optical galaxy, but there is [C_I] emission offset both red-ward and blue-ward. The [C_I] spectra did have problematic spectral baselines in the region around $-200 \rightarrow 0 \text{ km s}^{-1}$. We can be sure that there is no strong signal in that region, but cannot say anything else. Continuum subtraction was performed with IMCONTSUB in order to try to flatten the baselines but an order 3 polynomial was required which leads to extra uncertainty in the line fluxes. Careful inspection before and after subtraction shows that the subtraction has not produced any spectral features which were not there already in the original cube. There are three [C_I] components which

are outside the systemic velocity range: $v1 \sim -400 \text{ km s}^{-1}$ and $v2 \sim +250 \text{ km s}^{-1}$ are shown by the orange and red contours in Fig. 14 (top left) and $v3 \sim +450 \text{ km s}^{-1}$ is shown in green, though $v3$ is less convincing in the spectrum. The spectral profiles are shown individually for each velocity component in Fig. 14 with the colour of the spectrum matching the colour of the contours. The profile for the $v1$ component (which is present in both the main galaxy and the satellite) is shown as a solid orange line for the main galaxy and a dotted brown line for the satellite. The complex kinematics for this source, coupled with the presence of a neighbour at a similar redshift indicates that there is a disturbance of the gas but further observations would be necessary to be certain which of these features are real and related to an interaction.

We perform the analysis on gas mass in Section 4 using two versions of the [C_I] fluxes: conservatively using just the $v2$ component, because this has the least offset from the systemic optical velocity, and secondly using all three components which would be a maximum. There is no significant CO emission detectable at any of these velocities, nor at the systemic velocity. The ratio of line luminosity $L'_{\text{CI}} / L'_{\text{CO}} (= R_{\text{CI}})$ in this galaxy is thus higher than we see in other sources, ranging from $0.54 < R_{\text{CI}} < 0.94$, using the measured CO flux which is only 2σ significance. Using the 3σ upper limit on the CO flux gives a lower limit for this source of $R_{\text{CI}} > 0.35$. The average value in Milky Way clouds is $R_{\text{CI}} \sim 0.15$ (Frerking et al. 1989), while the average value seen in QSO is $R_{\text{CI}} \sim 0.29$ (Walter et al. 2011).

SDP.6451

This galaxy has $M_* = 5.6 \times 10^{10} M_\odot$ and $f_g = 0.17$. The GAMA spectrum (Fig. C6) has strong O[II] and H β in emission indicating ongoing star formation. There is only weak O[III] indicating that this is not an AGN (Lamareille 2010). Both dust and [C_I] line emission are strongly detected, while CO is much weaker. Figure 15 (top right) shows the CO contours on tapered [C_I] showing a roughly 2σ detection of flux at the same location and same velocity range as [C_I]. There is a wide blue wing in the [C_I] line profile which is extended to the east of the galaxy. At full resolution this appears to have structure, possibly spiral arms or tidal material. The tapered map suggests that this may be another source where the dust and [C_I] may be partially resolved out. The flux presented in Table 4 for [C_I] is integrated over the full extent of the emission from $-350 \rightarrow +150 \text{ km s}^{-1}$. The CO flux estimate is measured in an aperture over a similar velocity range. The dust emission appears to be morphologically different to the [C_I], there are two distinct clumps either side of the optical nucleus and no extension to the east as is apparent in [C_I] (Fig. 15). The $R_{\text{CI}} = 0.69^{+0.51}_{-0.27}$ for this source is also very high.

APPENDIX B: FLUX BOOSTING BY SMG

Flux boosting by the high redshift dusty galaxies in these fields affects all the *Herschel* SPIRE fluxes of our target $z = 0.35$ sources, but more so in the 350 and 500 μ m bands for two reasons. Firstly, the *Herschel* beam is larger with increasing wavelength and so a contaminant at distance r will have a higher weighting in the beam profile. Secondly, the observed sub-mm colour of the high redshift dust source will be redder (relatively brighter at 500 μ m) compared to the target source, as the observed frame samples closer to the peak of the SED. The percentage contamination at 500 μ m from the high- z SMG is thus larger than that at 250 μ m. In order to produce reasonably accurate physical parameters from SED fitting, we wanted to estimate the

Table B1. Estimated boost to the $z = 0.35$ H-ATLAS photometry due to the high redshift dusty galaxies within the *Herschel* beam, from Dunne et al. *submitted*.

SMG	S_{250}^C (mJy)	S_{350}^C (mJy)	S_{500}^C (mJy)
1160	13.6	16.9	16.8
2173	9.2	6.7	3.3
3366	12.5	7.7	3.4
4104	12.7	11.1	6.2
5347	2.0	3.4	3.0
6418	1.2	3.5	4.7
6451	1.6	4.2	5.1

Estimated contamination to the H-ATLAS SPIRE fluxes in Table 5.

possible contamination from the high redshift galaxy and investigate its impact on the results of the SED fitting. More details are given in Dunne et al. (2020). Briefly, we took the ALMA S_{850} for each high redshift dusty galaxy and calculated the flux that it should have in each of the *Herschel* SPIRE bands, using plausible values of $T_d = 38$ K, $\beta = 1.8$ and $z = 1.5 - 5$ for SMG (Chapman et al. 2005; da Cunha et al. 2015; Stach et al. 2019). Any redshift where the predicted signal should be highly visible in the H-ATLAS maps at the position of the SMG was ruled out. From the remaining possible redshifts we calculate the contribution of the high redshift dusty galaxy to the *Herschel* fluxes of the $z = 0.35$ galaxy by weighting its predicted flux at each band by the beam attenuation at the location of the $z = 0.35$ galaxy relative to the position of the SMG. We then correct the H-ATLAS DR-1 photometry in Table 5 for the possible contamination and fit the SEDs again with MAGPHYS. We choose the redshift at which the correction produces the lowest overall χ^2 for the SED fit and the best estimates of the contamination in the *Herschel* bands are listed in Table B1.¹⁷

APPENDIX C: MAGPHYS SED FITS AND OPTICAL SPECTRA FOR THE SAMPLE.

¹⁷ The redshift and T_d are roughly degenerate in this process but we are not attempting to constrain either; merely we wish to retrieve FIR colours which are most compatible with the PACS and ALMA $850\mu\text{m}$ photometry, which we know to be uncontaminated

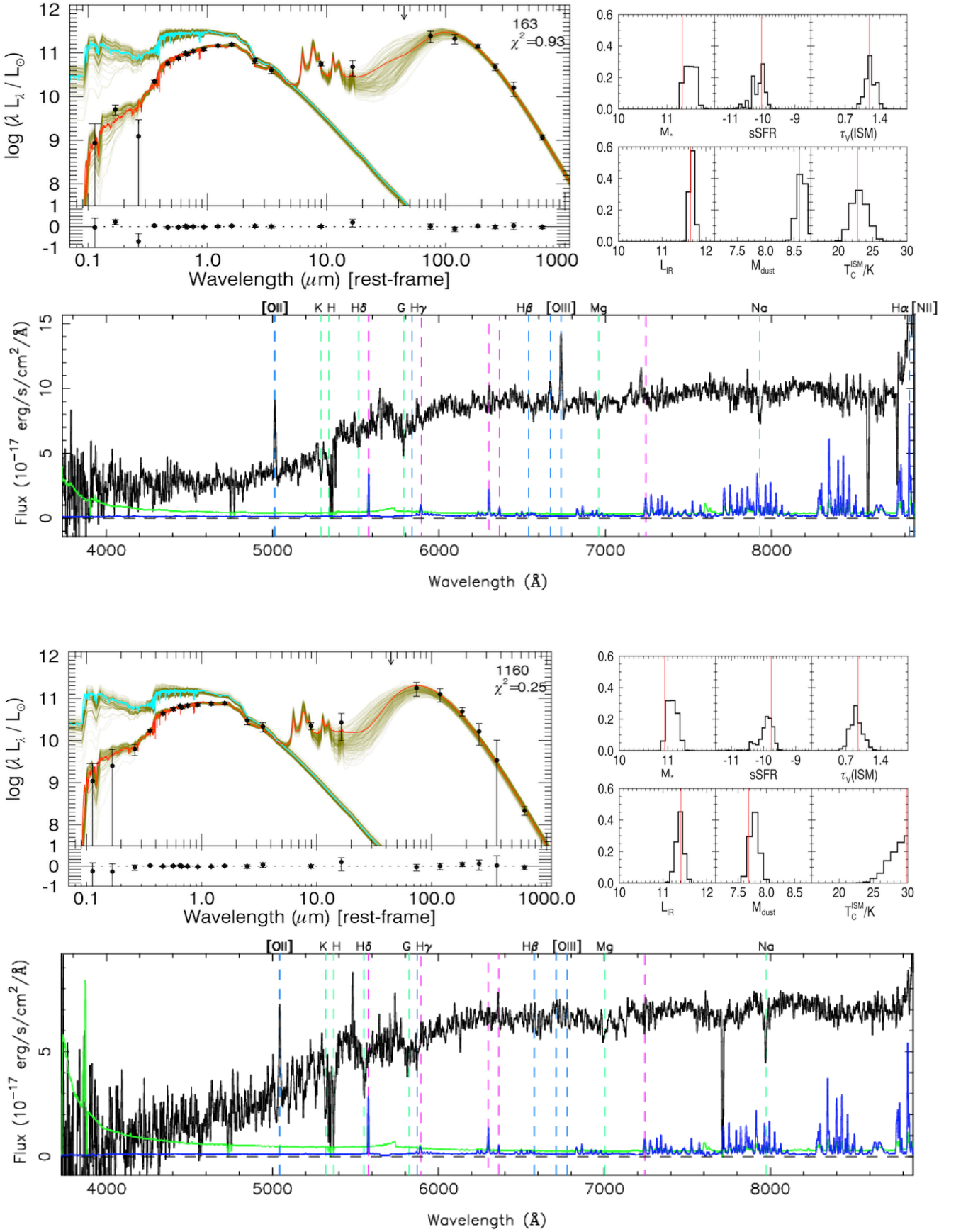


Figure C1. MAGPHYS best fit SED in red with 200 of the next best fits in olive. *top:* Optical spectrum for SDP.163 showing broad O[III] and O[II] in emission on a reddened continuum. *bottom:* Optical spectrum for SDP.1160 showing O[II] in emission on a reddened continuum.

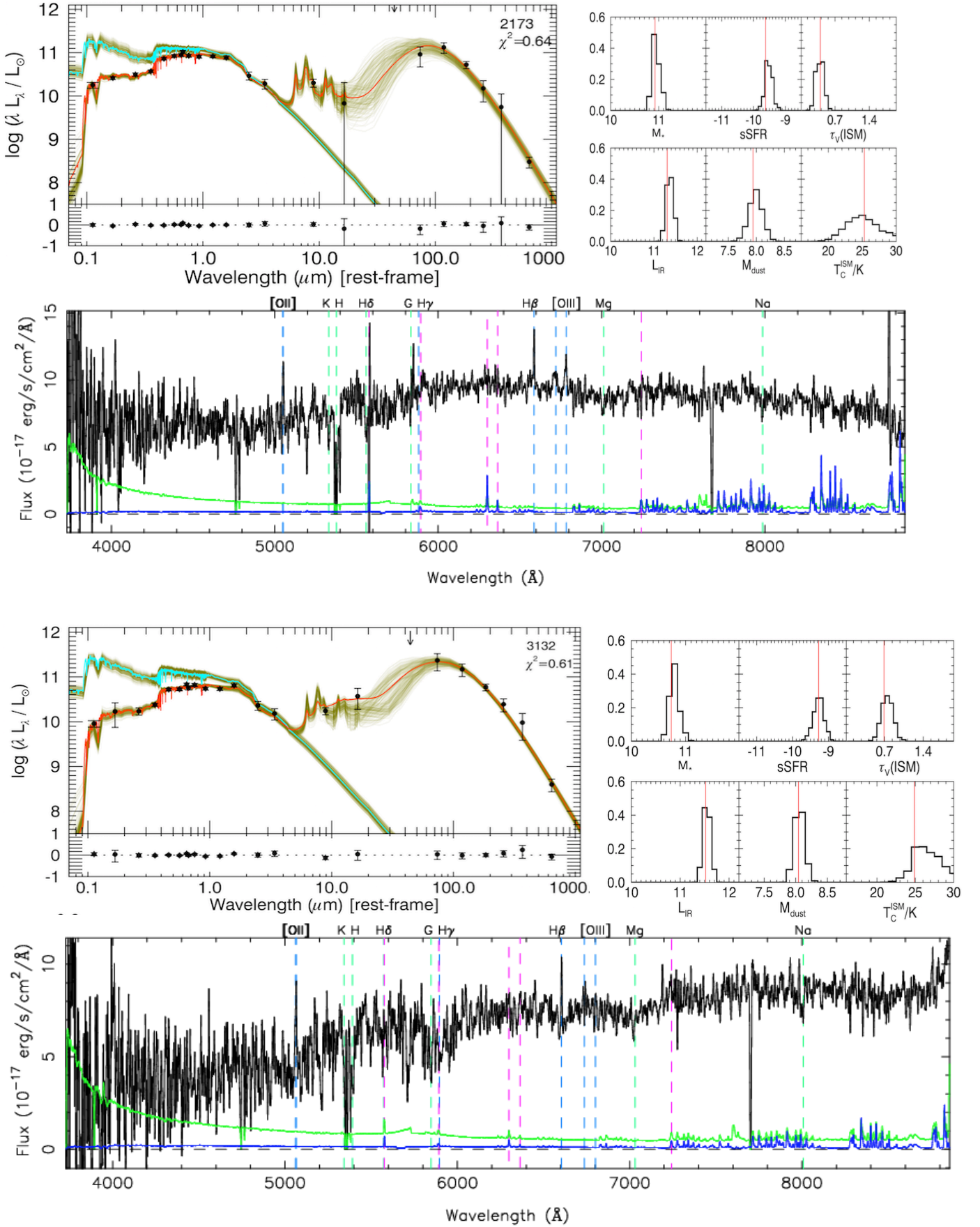


Figure C2. MAGPHYS best fit SED in red with 200 of the next best fits in olive. SDP.2173 optical spectrum showing weak O[II], H β and broad O[III] in emission. The attenuation for this source is relatively low as it is a face on spiral. SDP.3132 optical spectrum showing O[II] and H β in emission, O[III] is very weak.

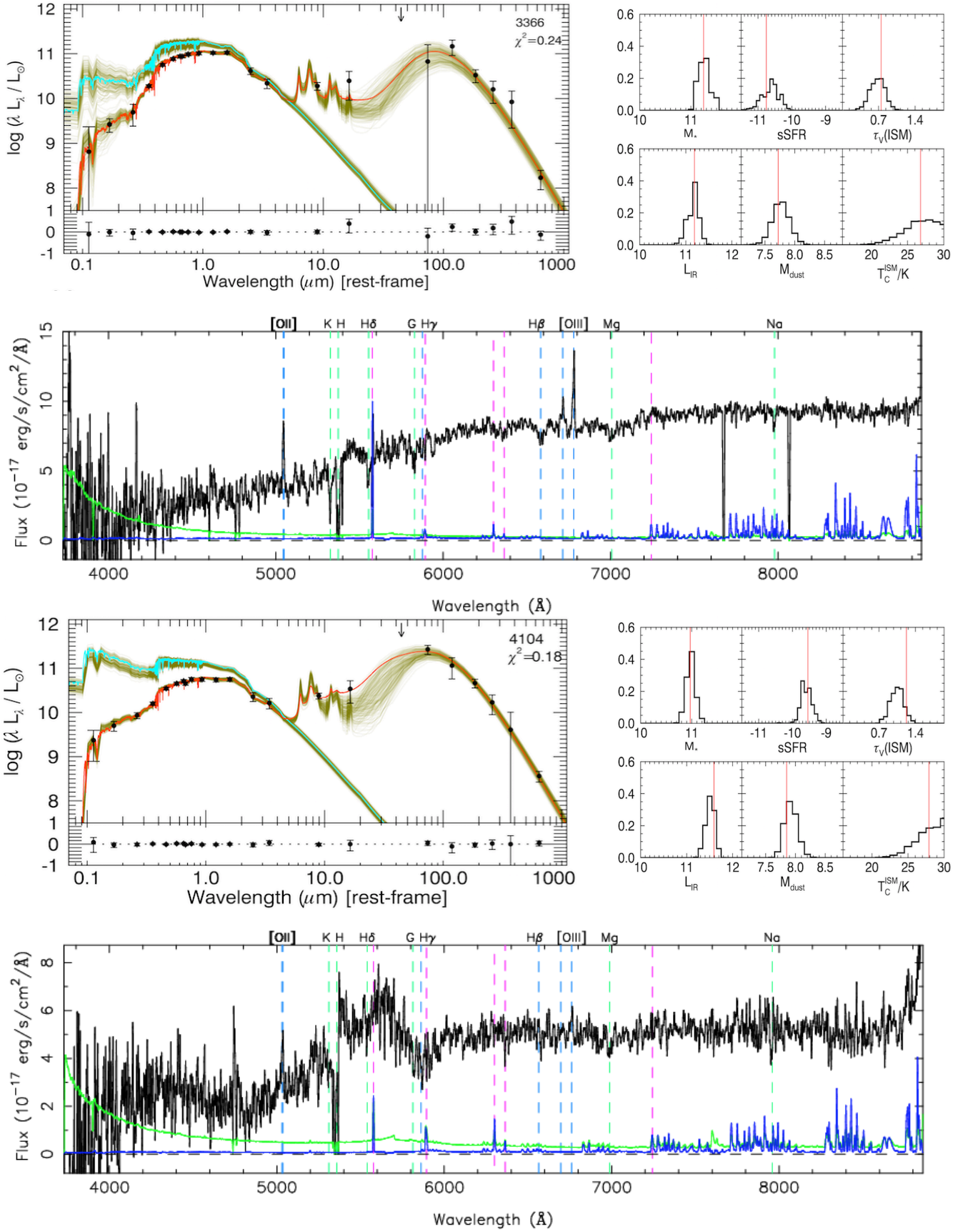


Figure C3. MAGPHYS best fit SED in red with 200 of the next best fits in olive. SDP.3366 optical spectrum showing strong Balmer absorption with broad O[III] and O[II]. SDP.4140 optical spectrum which is noisy with weak O[II] and O[III] emission and a large 4000Å break.

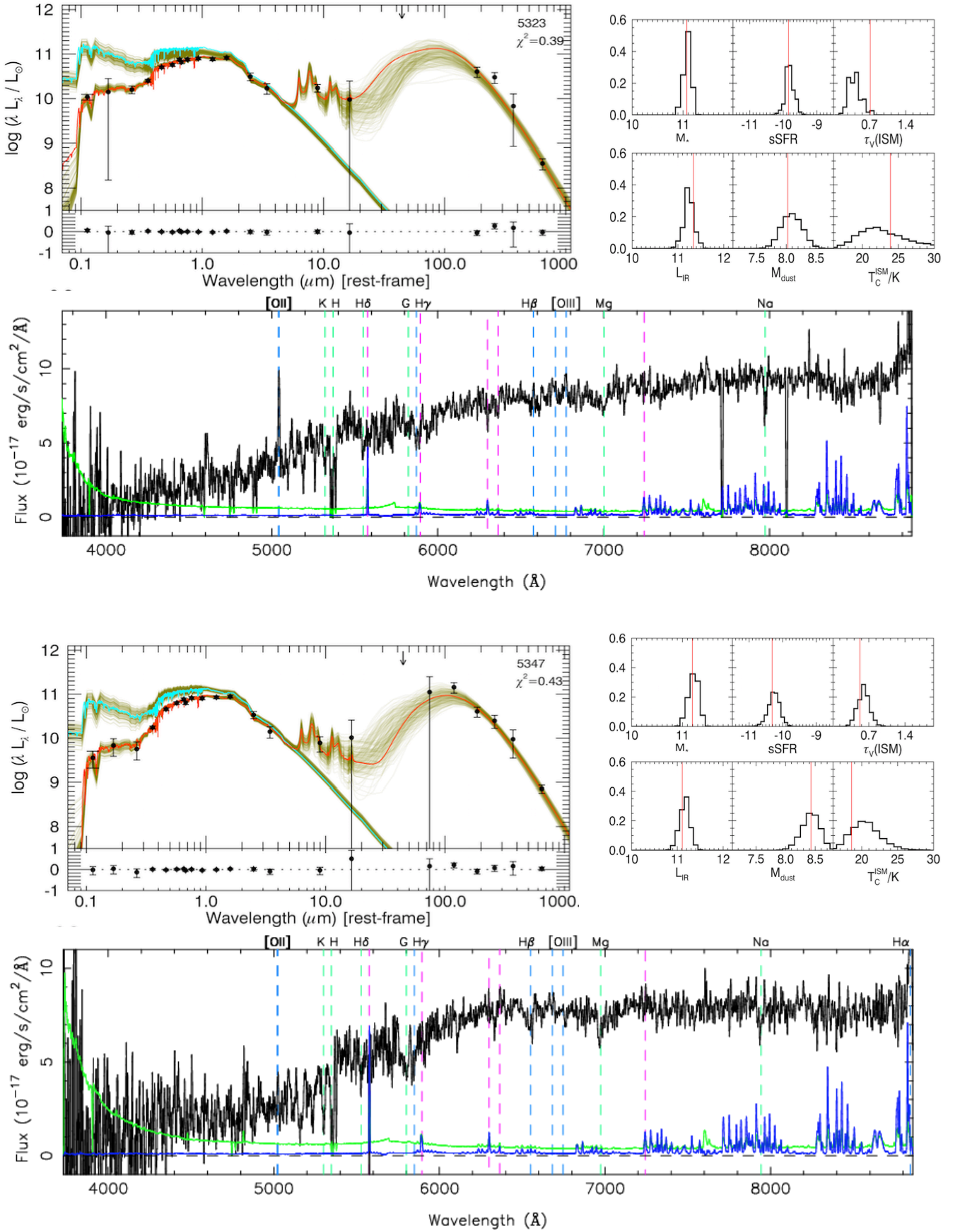


Figure C4. MAGPHYS best fit SED in red with 200 of the next best fits in olive. SDP.5323 optical spectrum with O[II] and weak but broad O[III] emission. SDP.5347 optical spectrum which has no emission lines, a large 4000 \AA break and strong Balmer absorption features.

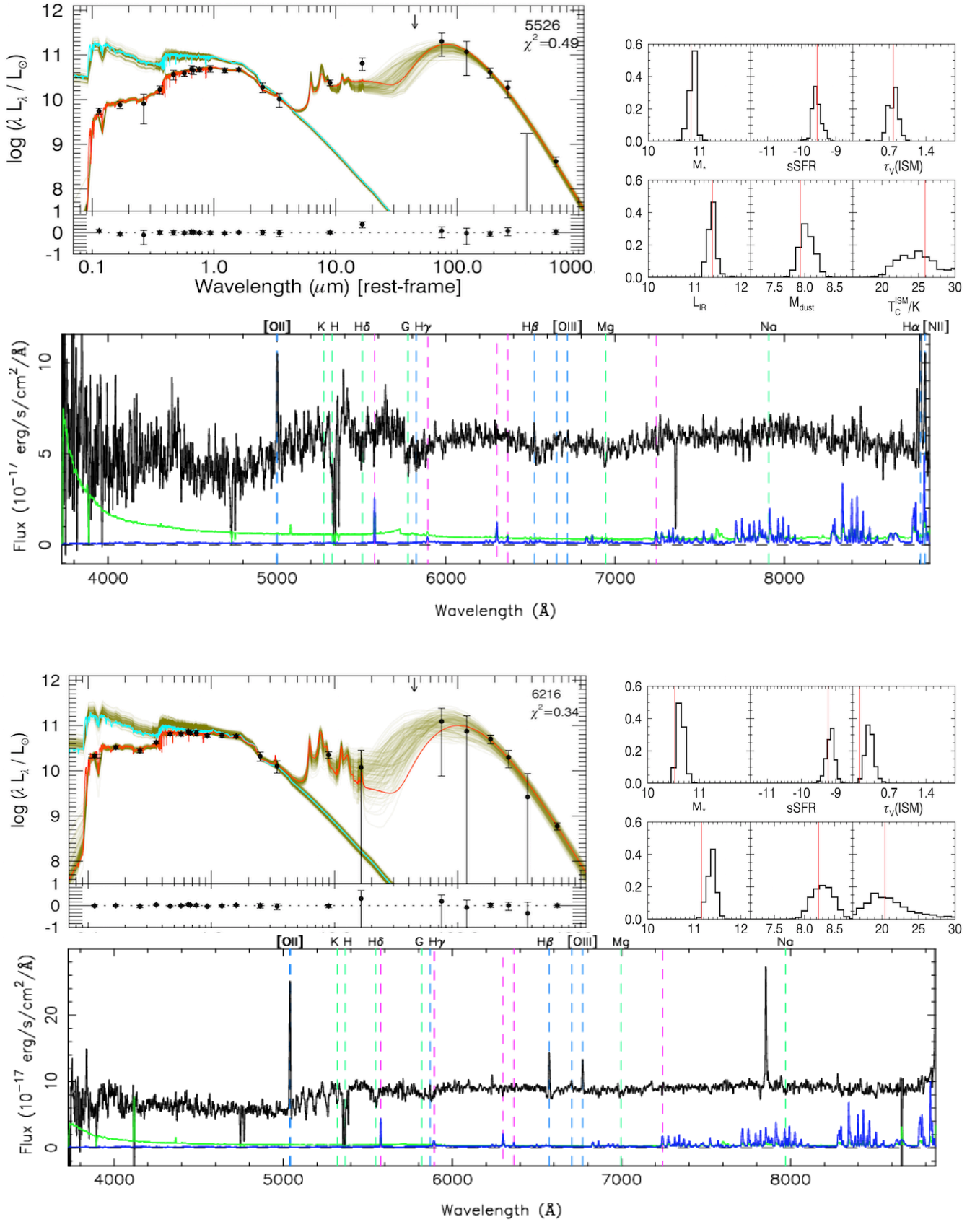


Figure C5. MAGPHYS best fit SED in red with 200 of the next best fits in olive. SDP.5526 optical spectrum shows O[II], weak H β and strong H α at the red edge of the band. SDP.6216 optical spectrum showing strong emission in O[II] and H β on a blue continuum with strong Balmer absorption features.

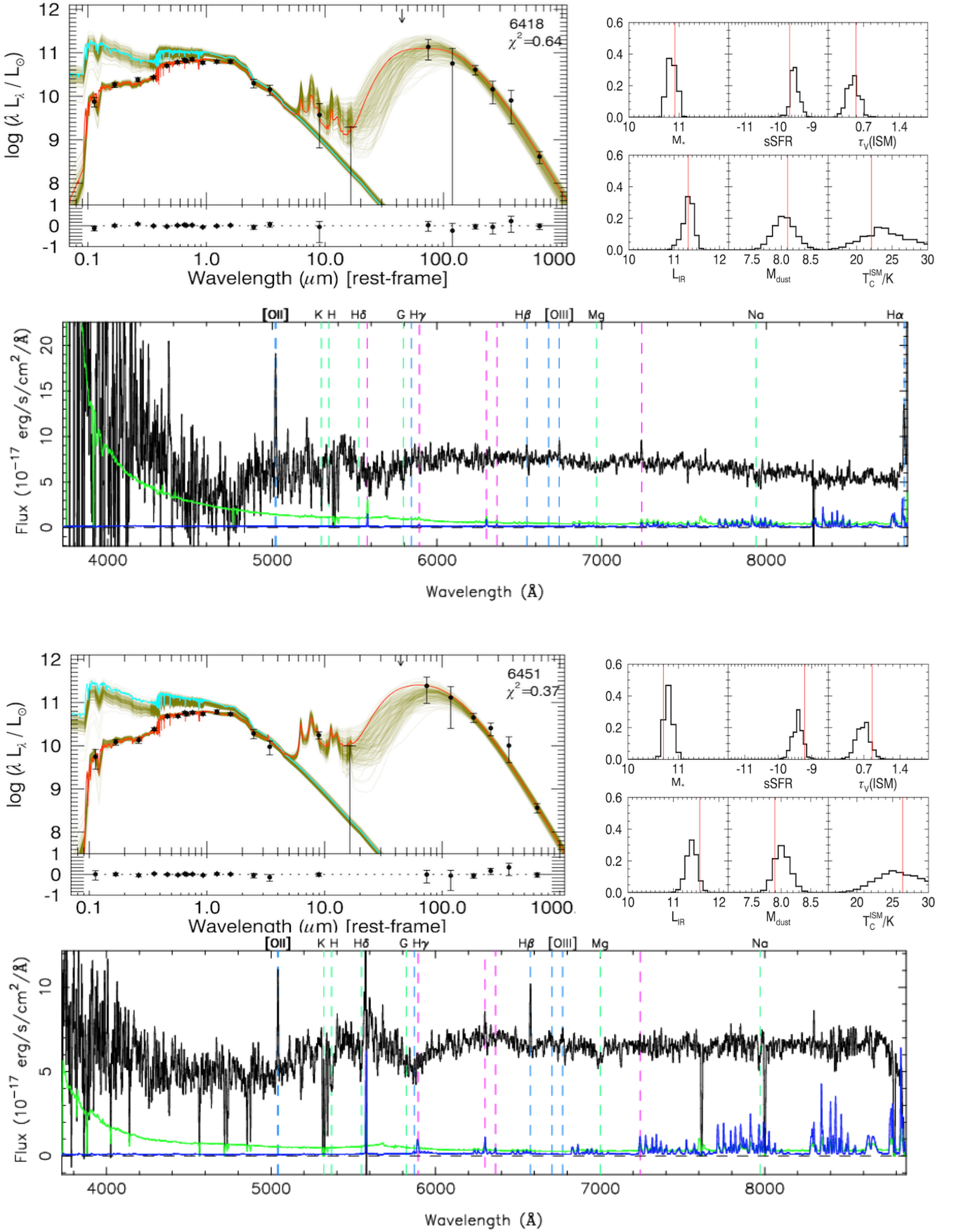


Figure C6. MAGPHYS best fit SED in red with 200 of the next best fits in olive. SDP.6418 optical spectrum shows a blue continuum with strong OII, weak H β and OIII and strong H α at the red edge of the spectrum. SDP.6451 optical spectrum shows strong O[II] and H β in emission indicating high current levels of SFR. There is only weak O[III] indicating that this is not an AGN.